Abstract

MCMULLAN, RICHARD JEFFREY. Numerical Boundary Conditions Simulating the Interaction Between Upstream Disturbances and an Axial Compressor. (Under the direction of Dr. D. Scott McRae.)

New small disturbance and area reduction compressor face boundary conditions that model the unsteady interactions of acoustic disturbances with an axial compressor are presented. The new small disturbance boundary condition is formulated to correct the deficiencies associated with the Paynter small disturbance model. The area reduction boundary condition provides a simple approach for the inlet outflow boundary. Both of these boundary conditions are implemented in one-dimensional and axisymmetric turbulent flow models of the inlet/compressor experiment at the University of Cincinnati. Acoustic reflections from the compressor face boundary conditions are compared against the measured experimental reflection characteristics of the axial compressor. The performance of the boundary conditions is also compared against existing boundary conditions such as the Paynter small disturbance boundary condition. These comparisons show that the new small disturbance boundary condition provides the best accuracy in terms of the prediction of the reflected disturbance from the interaction of an acoustic disturbance with a compressor. The results also show that the area reduction boundary condition produces acoustic reflections that agree well with the experimental data.

Numerical Boundary Conditions Simulating the Interaction Between Upstream Disturbances and an Axial Compressor

by

Richard Jeffrey McMullan

A dissertation submitted to the Graduate Faculty of
North Carolina State University
in partial fulfillment of the
requirements for the Degree of
Doctorate of Philosophy

Department of Mechanical and Aerospace Engineering

Raleigh, North Carolina

August 6, 2002

Approved By:

Dr. J. R. Edwards	Dr. N. D. Chokani
Dr. C. T. Kelley	Dr. D. S. McRae, Chair

Biography

Richard Jeffrey McMullan was born in Athens, Georgia on November 13, 1968 to Richard and Susan McMullan. Raised in Cornelia, Georgia, he became a Christian in 1980 and graduated from Habersham Central High School in 1987. He attended Clemson University on an Air Force ROTC scholarship and earned his Bachelor of Science degree in Mechanical Engineering in 1991. Upon his graduation, Richard was commissioned as a Second Lieutenant in the United States Air Force. His first assignment was at the High Explosive Research and Development Center at Eglin Air Force Base, Florida where he was Deputy Chief of the Explosive Processing Laboratory. In May 1995, 1st Lt McMullan was given the opportunity to further his education at the Air Force Institute of Technology, Wright-Patterson Air Force Base, Ohio. He earned his Masters of Science degree in Aeronautical Engineering in December 1996. He then was assigned to the National Air Intelligence Center at Wright-Patterson Air Force Base where he served as program manager for the technical assessment on foreign ballistic missiles. Richard has received many awards and medals for his outstanding service to his country. In August 1999, Captain McMullan was sent to North Carolina State University on an Air Force Institute of Technology Faculty Preparation Scholarship to pursue a Doctorate of Philosophy in Aerospace Engineering. Upon completion of his degree, Richard will return to the Air Force Institute of Technology to serve on the faculty in the Department of Aeronautical and Astronautical Engineering. On September 1, 2001, Richard married Rebekah Jean Billington. Rebekah is a registered nurse and currently working at the University of North Carolina hospital in Chapel Hill. Richard and Rebekah currently reside in Durham, North Carolina.

Acknowledgments

First, I praise my Savior Jesus Christ for the strength, support, and knowledge with which He has blessed me. I would like to thank my loving wife Rebekah for all her support, encouragement, and love. I would also like to thank my parents and Rebekah's parents for their encouragement and prayers. I thank my advisor, Dr. D. Scott McRae, for his support and guidance over the last three years. I would also like to thank Dr. Edwards for all of his advice and help over the years and especially with the axisymmetric code. Thank you to Dr. Kelley and Dr. Chokani for being on my committee and providing me with help on several occasions. I would like to acknowledge the support and data I received from Dr. Sajben and Dr. Freund at the University of Cincinnati. Their help was very crucial. In addition, I would also like to recognize Dr. Slater at NASA Glenn for his numerical data and models on the bump collapse mechanism. A special thank you to the Air Force Institute of Technology for the opportunity to pursue this Doctorate of Philosophy degree. I would also like to acknowledge the North Carolina Supercomputing Center for a grant of their computer resources. Finally, I would like to thank Ryan Bond for his friendship and support over the last three years.

Contents

List of Tables

List of Figures

List of Symbols

Roman symbols:

A	Jacobian matrix of Euler equations $\frac{\partial \mathbf{F}}{\partial \mathbf{U}}$
AR	relative area reduction
a	sound speed
c	blade chord
c_p	constant pressure specific heat
d	distance from closest wall
E, e	energy
$\mathbf{F}$	inviscid flux vector in axial direction
$\mathbf{F_v}$	viscous flux vector in axial direction
$\mathbf{G}$	inviscid flux vector in radial direction
$\mathbf{G_v}$	viscous flux vector in radial direction
g	grid speed
H	total enthalpy
h	enthalpy or bump height
i	axial direction
$\frac{1}{J}$	cell volume
j	radial direction
k	index for either ξ or η
L	length of domain
M	Mach number
N	number of cells or blade rotational speed
n_1	open frontal area
n_2	closed frontal area
Pr	Prandtl number
p	pressure
q	characteristic variable, heat flux, or dynamic pressure
R	universal gas constant or Roe averaged variable
$\mathbf{R}$	residual vector
r	characteristic variable or eigenvector
s	characteristic variable
S	cross-sectional area
s	blade spacing
T	bump collapse duration time or temperature
t	time
U	blade speed
$\mathbf{U}$	vector of conservative variables
$\mathcal{U}$	contravariant velocity in ξ direction
u	axial velocity
V	velocity

$\mathbf{V}$	vector of primitive variables
$\mathcal{V}$	contravariant velocity in η direction
v	radial velocity
$\mathbf{W}$	source vector
w	circumferential velocity
x	axial coordinate
y	radial coordinate

Greek symbols:

α	blade angle or Roe vector quantities
β	reflection response coefficient or blade angle
Γ	blade stagger angle
γ	ratio of specific heats
Δ	difference operator
δ	differential operator
δ^*	displacement thickness
ϵ	user defined quantity
η	generalized coordinate
κ	MUSCL quantity
λ	eigenvalue
μ	viscosity
ν	kinematic viscosity
ξ	generalized coordinate
ρ	density
τ	stress tensor or generalized time
ϕ_{cr}	rotor loss coefficient
Ω	rotation tensor
ω	minmod relaxation factor
∂	partial differential operator
∂w	wave amplitudes
∇	gradient operator

Subscripts:

0	flow region or initial
$1, 2, 3, 4, 5, 6, 7, 8, 9$	flow regions or Roe vector indices
a	absolute condition
amb	ambient
$bump$	flexible bump
CF	compressor face
cor	corrected
i, j, k	index notation

$inlet$	inlet condition
L	left cell interface
m	iteration level
mod	modulus
R	right cell interface
r	relative condition
ref	reference
$rotor$	first stage rotor
T	turbulent quantity
t	total condition or differentiation with respect to time
$VIGV$	variable inlet guide vane
x	axial component or differentiation with respect to x
y	radial component or differentiation with respect to y
η	differentiation with respect to η
θ	circumferential component
ξ	differentiation with respect to ξ
τ	differentiation with respect to τ

Superscripts:

$0, 1, 2, 3$	Runge-Kutta levels
I	inviscid
j	index notation
m	iteration level
n	time level
TL	thin layer
V	viscous
$+$	forward or turbulent scale
$-$	bckward
$'$	perturbation from reference state or Reynolds averaged fluctuating part
$''$	Favre averaged fluctuating part
$\rightarrow$	vector quantity
$\bar{}$	Reynolds averaged mean quantity
$\tilde{}$	Favre averaged mean quantity
$\hat{}$	vectors in generalized coordinates, normal quantity, or unit vectors
$\bar{\bar{}}$	Roe averaged values
$\hat{\bar{}}$	Roe averaged values

Acronyms:

BC	boundary condition
CFD	Computational Fluid Dynamics
CFL	Courant-Friedrichs-Lewy
HSCT	High Speed Civil Transport
IEP	incident expansion pulse
RCP	reflected compression pulse
REP	reflected expansion pulse
RPM	revolutions per minute
VIGV	variable inlet guide vane

1 Introduction

The success of commercial supersonic transport programs such as the NASA High Speed Civil Transport (HSCT) program is dependent on the development of a high-performance propulsion system. For flight Mach numbers above 2.0, a mixed-compression inlet is needed to provide high total pressure recovery and low flow distortion for the propulsion system. A mixed-compression inlet uses a system of oblique shocks upstream of the throat and a normal shock just aft the throat to decrease the inlet flow Mach number from supersonic at the freestream to subsonic at the face of the axial compressor. Supersonic mixed-compression inlets are susceptible to disturbances generated in the atmosphere (such as pressure and temperature changes). These disturbances can reduce the throat and normal shock Mach numbers and cause the shock system to be expelled from the inlet if the throat Mach number falls below 1.0 or the normal shock Mach number is less than the throat Mach number. This undesirable process is known as inlet unstart. The penalties of inlet unstart are significant reduction in total pressure recovery, dramatic increase in drag, and potential loss of aircraft control.[1]

In the past, almost all of the performance data needed to design the inlet was gathered from wind-tunnel testing. However, increased costs of wind-tunnel testing have led to the use of computational fluid dynamic (CFD) techniques for the design of inlets. In order to properly predict inlet unstart, unsteady CFD codes that correctly model the propagation of disturbances through the inlet are needed.

Several researchers have numerically modeled the mixed-compression inlet and compressor together as a system to investigate the unsteady flow field in the inlet. In most of these studies, the compressor was modeled in a simple one-dimensional sense.[2, 3, 4] Suresh, et. al. coupled three-dimensional inlet and turbomachinery CFD codes together to model the inlet/compressor combination.[5] However, they concluded that significant computer speed up would be required to make the coupling of inlet and compressor together a viable numerical design and analysis tool. Therefore, supersonic mixed-compression inlet flows are investigated separately from the compressor with the compressor dynamics represented by an outflow boundary condition.

Atmospheric disturbances can be decomposed into acoustic and convective disturbances to the inlet flow.[6] Acoustic disturbances are pressure disturbances that propagate downstream through the inlet at the flow speed plus the speed of sound. Convective disturbances are thermodynamic changes that propagate downstream through the inlet at the flow speed. Both types of disturbances eventually interact with the axial compressor and reflect back upstream as acoustic disturbances. Therefore, a viable outflow boundary condition for an unsteady inlet CFD code must properly model the wave reflection from the compressor.

Since the supersonic flow in the inlet is decelerated to subsonic flow at the compressor, the outlet boundary condition at the compressor face, for the inlet considered alone, is for subsonic outflow. In that case, one physical condition must be specified at the boundary and the remaining conditions are calculated using the information from the interior of the inlet. Traditionally, subsonic outflow boundary conditions have been evaluated by setting a selected variable to be constant on the boundary and solving the positive eigenvalue compatibility equations at the boundary. This technique is mathematically well posed but does not model the presence of the compressor.

A number of boundary conditions that simulate the presence of the compressor have been formulated by holding a variable constant at the boundary. The most commonly selected variables have been constant static pressure[4, 7], constant axial velocity[4], constant axial Mach number[1, 8], constant volumetric flow rate[7], and constant corrected mass flow rate[1, 7]. All of these boundary conditions are easy to implement and work well for steady inlet flows.

The experimental work by Freund and Sajben was conducted in a facility that mated a constant area annular duct with a multi-stage axial compressor from a General Electric helicopter engine.[9, 10, 11, 12, 16, 17] A downstream travelling expansion pulse was created from the collapse of a flexible bump. The reflection from the axial compressor was an expansion pulse travelling upstream. Four pressure transducers were used to record the passage of the incident wave from the bump collapse and the reflected wave from the compressor. The experiment provides comparative data for testing numerical compressor face boundary conditions. In Section 2, a detailed description of the experiment and the results observed will be presented.

When compared with the experimental data collected by Freund and Sajben, a constant static pressure boundary condition was shown to reflect the expansion wave travelling through the inlet with the wrong sign.[9, 10, 11, 12] Although constant axial velocity, constant axial Mach number, constant volumetric flow rate, and constant corrected mass flow rate all provide the proper sign of the reflection wave, the computational results showed that these boundary conditions overpredict the magnitude of the acoustic reflection when compared with the experimental data. Therefore, these simple boundary conditions do not accurately model the unsteady behavior at the compressor.

Mayer and Paynter developed a boundary condition model that specified compressor face corrected mass flow rate as a linear function of the stagnation conditions.[13] This boundary condition was found to provide better inlet unstart predictions than setting the corrected mass flow rate as a constant. In addition, Chung and Cole formulated a new boundary condition that specified a uniform Mach number at the compressor face and allowed the static pressure to vary along the face.[14] Numerical calculations performed by Slater and Paynter showed that both of these boundary conditions grossly overpredict the magnitude of the reflected acoustic wave when compared to University of Cincinnati experiment.[15] Therefore, these boundary conditions do not properly model the unsteady flow reflection at the compressor.

Paynter, et. al. have developed a small disturbance model for the interaction of freestream disturbances with an axial compressor.[18, 19, 20] This model provides the best agreement so far with the University of Cincinnati experimental data.[15, 20] However, this model does not take into account the turning of the flow by a compressor's inlet guide vanes. In addition, this small disturbance boundary condition assumes that no work is being done by the compressor at steady flow conditions. The Paynter model formulation and problems will also be presented in Section 2.

The current work uses the small disturbance ideas of Paynter, et. al. to develop a new small disturbance boundary condition that accounts for the presence of inlet guide vanes and models more closely the compressor dynamics. Section 3 presents the development of this new compressor face boundary condition. In addition, a simple area reduction boundary condition was developed for the compressor face outflow boundary. The area reduction condition compares the open frontal area a wave sees as it enters the blade passage to the physical cross-sectional area of the blade passage. The development of this boundary condition is also presented in Section 3.

Section 4 presents the governing equations for both the one-dimensional and axisymmetric two-dimensional models used to simulate numerically the experimental work performed at the University of Cincinnati. In Section 5, the numerical algorithms used to solve the two models are described in detail. Section 6 compares the performance of the new small disturbance boundary condition and area reduction boundary condition to the experimental data from the University of Cincinnati and the Paynter small disturbance model for both the one-dimensional and axisymmetric two-dimensional models of the experiment. Sections 7 presents the conclusions made about the use of these new boundary conditions in unsteady inlet analysis.

2 Prior Research

2.1 Compressor Face Boundary Condition Experiment

Freund and Sajben at the University of Cincinnati developed an experiment to study rapid flow transients in a constant area annular duct mated with an operating axial compressor.[9, 10, 11, 12, 16, 17] The experiment used a collapsing bump to create one millisecond duration acoustic expansion pulses travelling both upstream and downstream through the annular duct. The amplitude of the expansion pulse travelling downstream toward the compressor was approximately 4% of the mean static pressure. The incident and reflected expansion pulses were tracked using fast-response pressure transducers. From the pressure transducer data, the amplitude and duration of the reflected pulse were determined. This experimental research provides the CFD community with a database to validate new compressor face boundary condition formulations. However, since none of the currently available inlet outflow boundary conditions predict correctly the data collected in their research, Freund and Sajben concluded that new outflow boundary conditions are needed.[11, 12]

2.1.1 Experimental Apparatus and Test Procedure

The experiment at the University of Cincinnati mated a constant area annular duct to an axial compressor. Figure 1 shows the schematic of the experiment used by Freund and Sajben to investigate the reflection characteristics of the axial compressor to a downstream travelling acoustic pulse.

A General Electric T58-3 helicopter engine with the power turbine removed was used for this experiment. The engine was modified for cold operation by removing the combustor and fuel injection systems and replacing them with an external high pressure air supply for the turbine. The maximum attainable speed for the compressor in cold operation was approximately 20,000 RPM, which corresponds to an axial

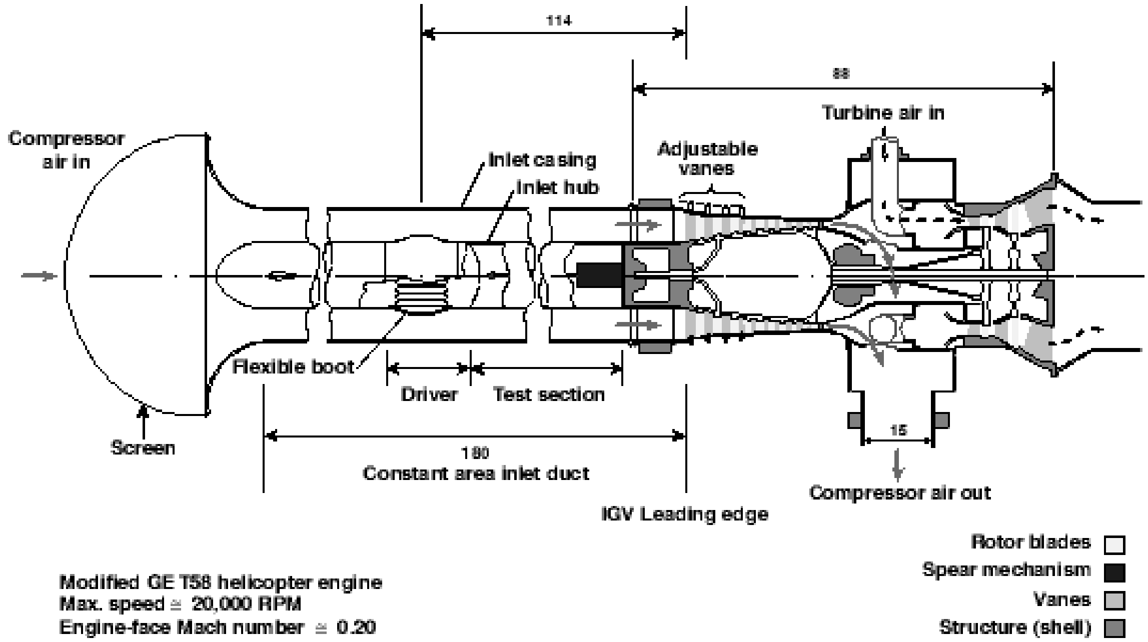

Figure 1: Inlet Duct and Compressor Rig Schematic (Dimensions in cm) [11]

compressor face Mach number of approximately 0.2. The compressor had ten stages and a pressure ratio up to 2.7 for the laboratory configuration.

The blade configuration data for the compressor is considered proprietary information by the General Electric Company. The Department of Mechanical and Aerospace Engineering at North Carolina State University was not able to get release of this information. However, the following descriptions of the compressor configuration have already been published.[11, 12, 15]

The compressor had ten stages and a variable inlet guide vane (VIGV) row powered by a linear actuator. The VIGV row contained 38 uncambered blades whose stagger angle varied from 31.7° to $-5.3°$. The first stage rotor contained 30 blades with a solidity and stagger angle at the mean radius of 1.16 and 52°, respectively. In addition, the cross-sectional area was reduced across the VIGVs by 87%.

Figure 1 shows the 1.80 m long constant area annular duct mated with the axial compressor. The duct's hub and case diameters were 0.137 m and 0.258 m, respectively. This corresponded to an annular height of 0.0605 m. The annular duct had a flexible collapsing bump whose center was located 1.14 m from the leading edge of the VIGVs. Figures 2 and 3 show the flexible bump deflated and inflated, respectively. These figures also show that the transition from the hub to the bump for both cases was continuous. The bump was inflated to a height of 0.0111 m at its center and completely deflated in 0.0008 seconds by rupturing a diaphragm.

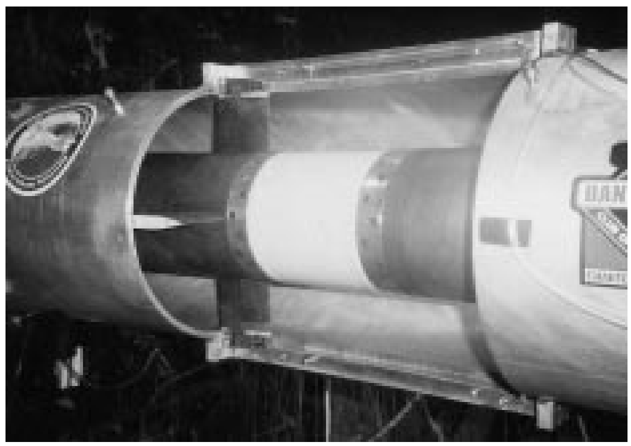

Figure 2: Deflated Flexible Bump in the Constant Area Annular Duct [11]

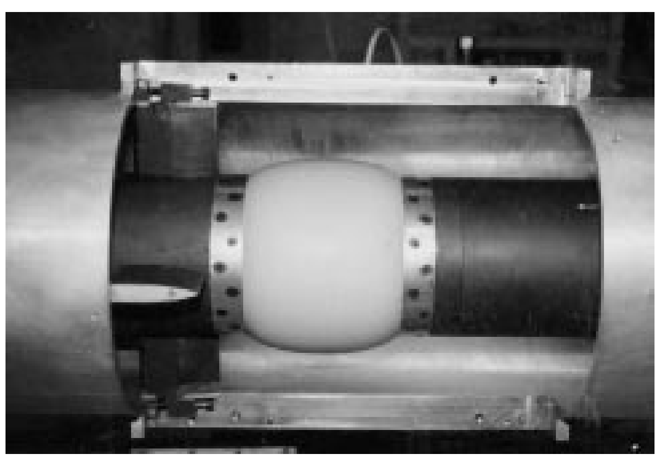

Figure 3: Inflated Flexible Bump in the Constant Area Annular Duct [11]

Six fast response pressure transducers were used to monitor the travel of the downstream moving incident expansion pulse and its reflected upstream moving expansion pulse. Four transducers were mounted on the case and two on the hub. Figure 4 shows the four axial locations of the transducers.

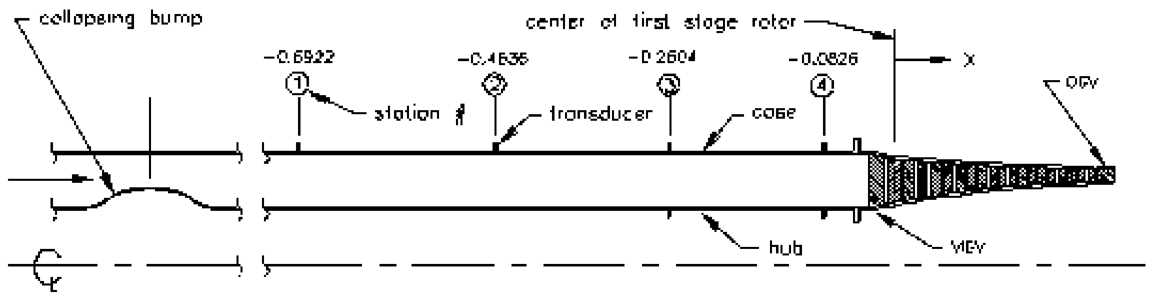

Figure 4: Location of the Pressure Transducers (Dimensions in m) [11]

The following test procedure was employed by Freund and Sajben for the experiments. First, the flexible bump was inflated to the proper height using helium gas. Once steady state conditions were achieved in the inlet, the steady state flow parameters of ambient pressure and temperature, corrected mass flow rate, and corrected compressor speed were recorded. Then, the diaphragm was burst which simultaneously caused the bump to deflate and the pressure transducers to acquire data. Finally, the data from the pressure transducers was reduced to show the travel of the acoustic waves in the inlet.

2.1.2 Experimental Results

Freund and Sajben performed many experimental tests using the inlet and axial compressor set-up at low speed inlet Mach numbers of 0.10 to 0.18. The data collected from these runs are available at the University of Cincinnati Aerospace Engineering anonymous ftp server (ftp.ase.uc.edu).[11] The reduced data files provided the pressure perturbation histories of all six pressure transducers for each experimental test.

Figure 5 shows the plots of differential pressures at each of the four transducer locations on the annular case versus time for an inlet Mach number M_{inlet} of 0.17. The differential pressures δp were the differences in pressure from the steady state pressure recorded at each transducer. The downstream travelling incident expansion pulse created by the deflated bump is labelled IEP. The reflection of this incident pulse is an upstream travelling expansion pulse labelled REP. In addition, the deflated bump creates an upstream travelling expansion pulse which is reflected off the bellmouth entrance as a compression pulse labelled RCP. At pressure transducer 4, the incident and reflected expansion pulses overlap. In order to investigate the shape and amplitude of the reflected expansion pulse, the incident pulse measured at transducer 1 was shifted in time and subtracted from the pressure data collected at transducer 4.

Figure 6 shows an expanded view of the reflected expansion pulse in Figure 5 at transducer 4. The maximum amplitude of the reflected pulse from the compressor is approximately 36% of the incident pulse amplitude. From plots similar to this figure, Freund and Sajben determined that the first and largest negative peak in the pulse's pressure plot represents the reflection of the incident pulse from the first stage rotor.[11] They also deduced that the other negative peaks were reflections from the next few stages in the compressor. In addition, numerical work performed by Slater, Freund, and Sajben showed that the traditional subsonic outflow boundary conditions provided reflection pulses that differed sharply from those observed from experimental data, for example the reflected pulse given in Figure 6.[11, 17] This result emphasizes the need for the development of new compressor face boundary conditions that agree more closely with the experimental data.

After investigating the experimental data, Freund and Sajben also concluded that the axial Mach number at the compressor face and the stagger angle of the VIGVs

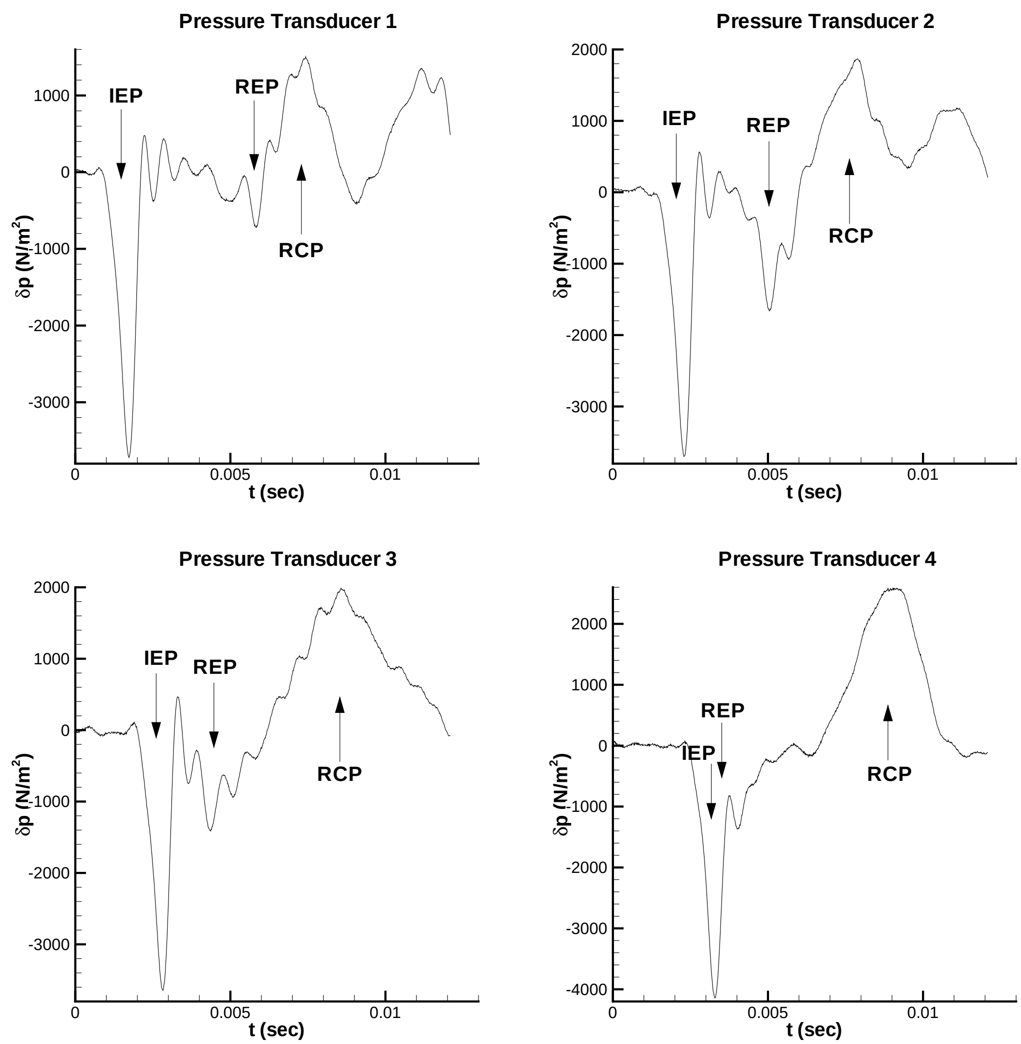

Figure 5: Temporal Evolution of Acoustic Pulses for $M_{inlet} = 0.17$

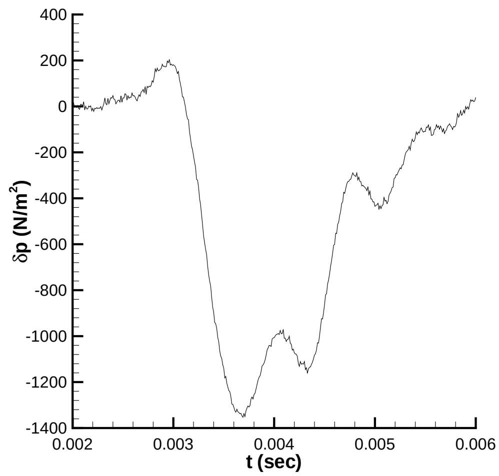

Figure 6: Expanded View of Reflection Pulse at Trnasducer 4 for $M_{inlet} = 0.17$

had a significant effect on the reflection process of the incident expansion pulse.[11] The amplitude of the reflected wave increased for both increases in the Mach number and the stagger angle.

2.2 Paynter Small Disturbance Compressor Face Boundary Condition

Paynter et. al. have developed a new compressor face boundary condition based on a small disturbance model of the unsteady flow around a compressor's first stage.[15, 19, 20] The results of this small disturbance boundary condition were compared to the experimental data collected at the University of Cincinnati. Figure 7 shows that this compressor face boundary condition provides significant improvement over the existing boundary conditions of constant pressure, velocity, and Mach number.

2.2.1 Paynter Small Disturbance Formulation

Paynter conducted a parametric numerical study on a two-dimensional cascade to determine the amplitude of the reflected disturbance as a function of the blade cam-

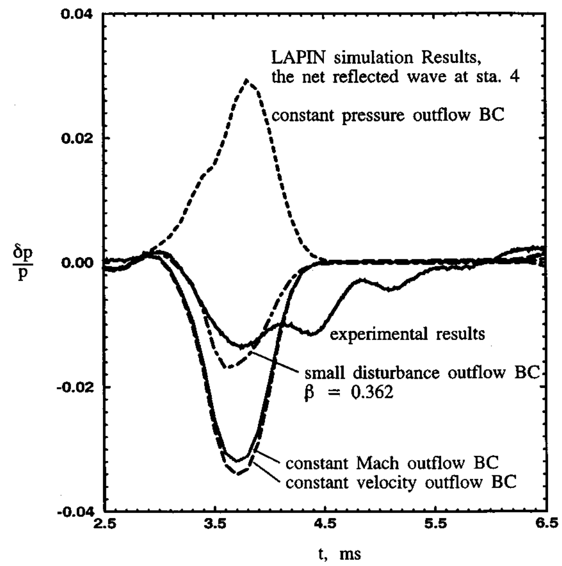

Figure 7: Comparison of Numerical and Experimental Results[20]

ber, blade loading, blade solidity, blade stagger angle, incident acoustic disturbance strength, and upstream axial Mach number.[18] His results showed that only the blade stagger angle and the upstream axial Mach number had a strong effect on the reflected wave.

Using the results from the parametric cascade study, Paynter et. al. developed a small disturbance boundary condition based on the following assumptions.[20]

1. Blade geometry was modeled as a flat plate with zero thickness and a solidity greater than 1.0.

2. Flow properties prior to the incident acoustic disturbance were known.

3. Prior to the acoustic disturbance, the flow was aligned with the first stage rotor such that the flow properties upstream and downstream of the blade passage were the same. Figure 8 shows a schematic of the flow field prior to the interaction of the disturbance with the rotor.

4. Incident acoustic disturbance was a step change in static pressure and travelled downstream towards the blade passage.

5. The response of the blade passage to the interaction with the incident acoustic disturbance was a reflected acoustic disturbance travelling upstream and a transmitted acoustic disturbance travelling downstream. Figure 9 shows a schematic of the flow field around the first stage rotor after its interaction with the incident disturbance.

6. Flow at the exit of the blade passage was aligned both before and after the transmitted acoustic disturbance.

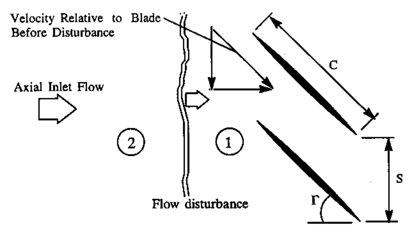

Figure 8: Flow Schematic Prior to Acoustic Disturbance[20]

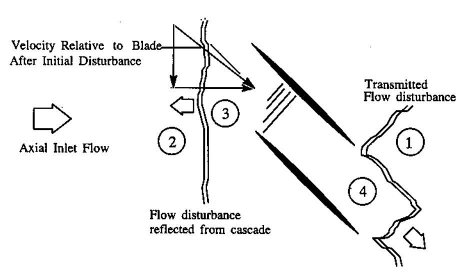

Figure 9: Flow Schematic After Interaction of Disturbance with Rotor[20]

The formulation of the Paynter small disturbance boundary condition used the following small perturbation relationships derived by Shapiro.[21] For right-running (downstream travelling) acoustic waves,

$$\frac{\delta p}{p} = \gamma \frac{\delta u}{a} = \gamma M \frac{\delta u}{u} \tag{1}$$

For left-running (upstream travelling) acoustic waves,

$$\frac{\delta p}{p} = -\gamma \frac{\delta u}{a} = -\gamma M \frac{\delta u}{u} \tag{2}$$

In addition, Paynter et. al. used the following notation system for relating the flow properties in regions $1-4$ of Figures 8 and 9.

$$\begin{aligned} p_2 &= p_1 + p_2' \qquad & u_2 &= u_1 + u_2' \\ p_3 &= p_1 + p_3' \qquad & u_3 &= u_1 + u_3' \\ p_4 &= p_1 + p_4' \qquad & u_4 &= u_1 + u_4' \end{aligned} \tag{3}$$

Region 1 was designated as the reference state, and the prime quantities represented small perturbations from the reference state.

Using Equations (2) and (3), the flow properties across the reflected acoustic disturbance were given by

$$\frac{p_3'}{p_1} + \gamma M_{x1} \frac{u_3'}{u_1} = 2\frac{p_2'}{p_1} \tag{4}$$

Assuming no time rate of change of mass in a control volume fixed to the blade passage given in Figure 9, the continuity equation for the control volume was given by

$$\frac{p_3'}{p_1} + \gamma \frac{u_3'}{u_1} - \frac{p_4'}{p_1} - \gamma \frac{u_4'}{u_1} = 0 \tag{5}$$

Using this control volume and assuming no time rate of change of energy within the control volume, the energy equation was given by

$$\frac{p_3'}{p_1} + \gamma M_{x1}^2 \frac{u_3'}{u_1} - \frac{p_4'}{p_1} - \gamma \frac{M_{x1}^2}{\cos^2 \Gamma} \frac{u_4'}{u_1} = 0 \tag{6}$$

Finally, the flow properties across the transmitted acoustic disturbance were given by

$$\frac{p_4'}{p_1} - \gamma \frac{M_{x1}}{\cos\Gamma} \frac{u_4'}{u_1} = 0 \tag{7}$$

Equations (4) through (7) formed a system of linear equations which were solved to determine a formulation for the reflection response coefficient. This response coefficient β was defined to be the ratio of reflected acoustic disturbance strength to incident acoustic disturbance strength.

$$\beta = \frac{p_3 - p_2}{p_2 - p_1} = \tan^2\left(\frac{\Gamma}{2}\right)\left[\frac{1 + M_{x1}}{1 - M_{x1}}\right] \tag{8}$$

Paynter et. al. used the linearized Euler equations in characteristic form to apply the small disturbance boundary condition into a CFD code.[20] Using region 1 in Figures 8 and 9 as the reference state, the linearized Euler equations in characteristic form were given by

$$\begin{aligned} \frac{\partial q}{\partial t} &+ [u_1 + a_1]\frac{\partial q}{\partial x} = 0 \\ \frac{\partial r}{\partial t} &+ [u_1 - a_1]\frac{\partial r}{\partial x} = 0 \\ \frac{\partial s}{\partial t} &+ [u_1]\frac{\partial s}{\partial x} = 0 \end{aligned} \tag{9}$$

where $q = u + \dfrac{a_1}{\gamma}\ln p$, $r = u - \dfrac{a_1}{\gamma}\ln p$, and $s = \dfrac{1}{\gamma}\ln p - \ln\rho$.

After investigating the characteristic behavior of the boundary where the incident acoustic disturbance interacts with the compressor, Paynter et. al. concluded that $r + \beta q$ was a Reimann invariant on the boundary.[20] Then, the small disturbance compressor face boundary equation for pressure was given by

$$\frac{\partial p}{\partial t} = -\left(u_1 + a_1\right)\left(1 + \beta\right)\frac{\partial p}{\partial x} \tag{10}$$

where β was calculated using Equation (8). In addition, the density and velocity at the boundary were calculated using the positive eigenvalue characteristic equations in Equation (9) and the new pressure calculated from Equation (10).

2.2.2 Problems with Paynter Small Disturbance Formulation

Paynter et. al. applied their small disturbance boundary condition across the blade passage of a compressor's first stage rotor. The only two parameters that affected their reflection response coefficient were the axial Mach number before the incident disturbance and the stagger angle of the rotor blades. They assume that the flow entering the rotor was purely axial. This assumption neglected the flow turning provided by inlet guide vanes.

In the Paynter model, the rotor blades were modeled as flat plates so that the initial steady conditions on both sides of the blade passage were equal. This model of the rotor did zero work on the fluid at steady state. In comparison, rotor blades in a real compressor have camber, and the first stage rotor does work on the fluid. In addition, the flat plate model did negative work on the fluid (i.e. acted as a turbine) when the incident acoustic disturbance was a compression wave. Therefore, the flat blades inaccurately model actual rotor blades. This small disturbance model needs to be corrected to consider inlet guide vanes and real blade shapes.

2.2.3 Modification to Paynter Small Disturbance Formulation

Sajben developed a small disturbance compressor face boundary condition that was very similar to the Paynter model.[22] The only exception was that Sajben assumed the transmitted disturbance did not travel along the direction of the blade passage. In his model, the transmitted wave propagated along the axial direction, and an additional vorticity wave was created off the trailing edge of the blades to align the flow behind the transmitted disturbance with the blade passage. According to Sajben, the change in flow angle into the blade passage created lift on the blades which produced a starting vortex from each blade. Using this new assumption, Sajben's formulation for the reflection response coefficient was given by

$$\beta = \frac{M_{x1} \tan^2 \Gamma}{2\left(1 + M_{x1}\right) + M_{x1} \tan^2 \Gamma} \tag{11}$$

Numerical calculations performed by Slater and Paynter showed that the Paynter small disturbance boundary condition predicted more closely the magnitude of the reflected acoustic disturbance than the Sajben model when compared to University of Cincinnati experimental data.[15] The results in Section 6 will also show that the Paynter model performs better than the Sajben model. In addition, the Sajben small disturbance boundary condition modification did not improve on any of the problems that occurred with the Paynter model.

3 New Compressor Face Boundary Conditions

Two new compressor face boundary conditions were developed to model the axial compressor reflection process. These boundary conditions must accurately calculate the amplitude of the reflected disturbance and be simple enough to implement into existing CFD codes. In this section, both the new small disturbance and area reduction boundary conditions will be presented.

3.1 New Small Disturbance Boundary Condition

A new small disturbance compressor face boundary condition that models the interaction of an acoustic disturbance and an axial compressor was developed to correct the problems in the Paynter small disturbance formulation. This model accounts for the turning of the flow through the inlet guide vanes. In addition, the model uses cambered blade geometry and the velocity of the compressor blades in the calculation of the reflection response coefficient β from an axial compressor. Therefore, this formulation includes more of an axial compressor's flow dynamics.

3.1.1 Small Disturbance Formulation

Most of the same assumptions employed by Paynter et. al. were also used in this new boundary condition development. However, changes were made to model the effects of the inlet guide vanes and the cambered blade designs. This small disturbance boundary condition is formulated based on the following assumptions:

1. The flow properties prior to the incident acoustic disturbance interacting with the axial compressor are known.

2. Prior to the acoustic disturbance, the flow is aligned with the blade passages of both the inlet guide vanes and the first stage rotor.

3. The flow is isentropic through the inlet guide vanes.

4. The incident acoustic disturbance is a step change in static pressure and travelled downstream towards the compressor.

5. The response of each blade passage to the interaction with an acoustic disturbance is a reflected acoustic disturbance travelling upstream and a transmitted acoustic disturbance travelling downstream.

6. The flow at the exit of each blade passage is aligned with the blade angle both before and after its interaction with the acoustic disturbance.

This boundary condition models an acoustic disturbance's travel through the inlet guide vanes and first stage rotor of an axial compressor. First, the acoustic disturbance propagates downstream through the inlet at the flow speed plus the speed of sound and interacts with the inlet guide vanes of the axial compressor. Figure 10 shows schematically the flow field around the inlet guide vanes prior to the arrival of the incident acoustic disturbance. The flow Mach number M_1 behind the inlet guide vanes is calculated from the following equation for constant mass flow rate using a Newton iteration.

$$\frac{S_1 M_1 \cos\alpha_1}{\left[1+\frac{\gamma-1}{2}M_1^2\right]^{\frac{\gamma+1}{2(\gamma-1)}}} = \frac{S_0 M_0}{\left[1+\frac{\gamma-1}{2}M_0^2\right]^{\frac{\gamma+1}{2(\gamma-1)}}} \tag{12}$$

where S is the cross-sectional area and α_1 is the blade passage exit angle. Using the assumption of isentropic flow across the inlet guide vanes, the thermodynamic variables at the exit of the guide vanes are computed. In addition, the axial Mach number M_{x1}, axial velocity u_1, and circumferential velocity w_1 are calculated at the exit.

The result of the interaction of the acoustic disturbance with the inlet guide vanes is a reflected wave travelling upstream and a transmitted wave travelling downstream

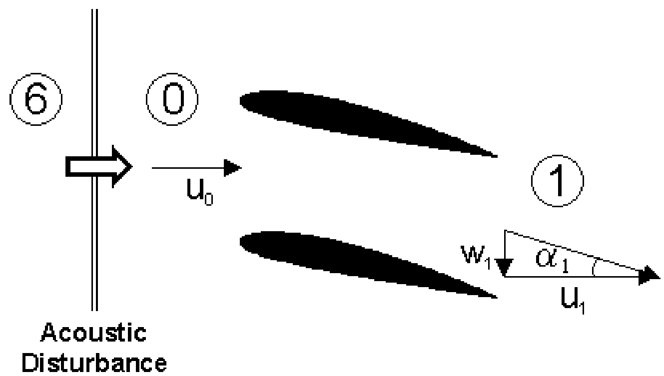

Figure 10: Flow Schematic of Inlet Guide Vanes Prior to Incident Acoustic Disturbance

aligned with the exit angle of the blade passage. Figure 11 depicts the flow around the inlet guide vanes after its interaction with the incident acoustic wave.

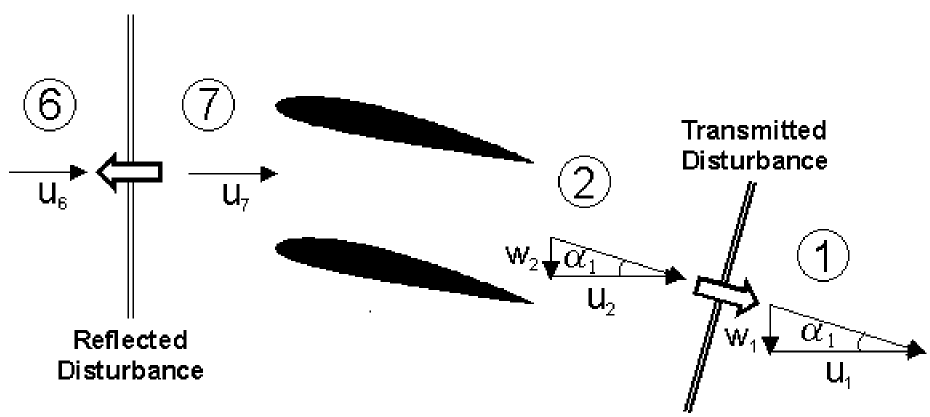

Figure 11: Flow Schematic of Inlet Guide Vanes After Interaction With Incident Acoustic Disturbance

The following small disturbance notation system is used to relate the flow properties in regions 0, 1, 2, 6, and 7 of Figures 10 and 11.

$$\begin{array}{lll} p_6 = p_0 + p'_6 & u_6 = u_0 + u'_6 & \rho_6 = \rho_0 + \rho'_6 \\ p_7 = p_0 + p'_7 & u_7 = u_0 + u'_7 & \rho_7 = \rho_0 + \rho'_7 \\ p_2 = p_1 + p'_2 & u_2 = u_1 + u'_2 & \rho_2 = \rho_1 + \rho'_2 \end{array} \tag{13}$$

Regions 0 and 1 are designated as the reference states in front of and behind the inlet guide vanes, respectively.

Using Equations (1) and (13), the flow properties across the incident acoustic disturbance are given by

$$\frac{p'_6}{p_0} = \gamma M_{x0} \frac{u'_6}{u_0} \tag{14}$$

Using Equations (2) and (13), the flow properties across the reflected acoustic disturbance are given by

$$\frac{p'_7}{p_0} - \frac{p'_6}{p_0} = -\gamma M_{x0} \left(\frac{u'_7}{u_0} - \frac{u'_6}{u_0} \right) \tag{15}$$

This equation is simplified into the following form by substituting Equation (14) into it and rearranging.

$$\frac{p'_7}{p_0} + \gamma M_{x0} \frac{u'_7}{u_0} = 2 \frac{p'_6}{p_0} \tag{16}$$

Assuming no time rate of change of mass in a control volume attached to the inlet guide vanes, the continuity equation has the following forms.

$$\begin{aligned} \rho_7 u_7 S_0 &= \rho_2 u_2 S_1 \\ \rho'_7 u_0 S_0 + \rho_0 u'_7 S_0 &= \rho'_2 u_1 S_1 + \rho_1 u'_2 S_1 \end{aligned} \tag{17}$$

Using the isentropic relation

$$\frac{\delta \rho}{\rho} = \frac{1}{\gamma} \frac{\delta p}{p} \tag{18}$$

Equation (17) is reduced to the following form.

$$\frac{p_7'}{p_0} + \gamma\frac{u_7'}{u_0} = \frac{p_2'}{p_1} + \gamma\frac{u_2'}{u_1} \tag{19}$$

Assuming no time rate of change of energy for this control volume, the conservation of energy equation is given by

$$\begin{aligned} h_{t7} &= h_{t2} \\ \frac{\gamma}{\gamma-1}\frac{p_7}{\rho_7} + \frac{1}{2}u_7^2 &= \frac{\gamma}{\gamma-1}\frac{p_2}{\rho_2} + \frac{1}{2}\left(u_2^2 + w_2^2\right) \end{aligned} \tag{20}$$

where h_t is the total enthalpy. Using Equation (18) and the velocity component relation $w_2 = u_2 \tan\alpha_1$, Equation (20) is reduced to the following form.

$$\frac{p_7'}{\rho_0} + u_7' u_0 = \frac{p_2'}{\rho_1} + \frac{u_2' u_1}{\cos^2\alpha_1} \tag{21}$$

Using Equations (1) and (13), the flow properties across the transmitted acoustic disturbance are given by

$$\frac{p_2'}{p_1} = \frac{\gamma M_{x1}}{\cos\alpha_1}\frac{u_2'}{u_1} \tag{22}$$

Equations (16), (19), (21), and (22) form a system of linear equations for four unknowns p_7', p_2', u_7', and u_2'. This linear system is solved to determine ratio of the transmitted acoustic disturbance strength to the known incident acoustic disturbance strength.

$$\frac{\dfrac{p_2'}{p_1}}{\dfrac{p_6'}{p_0}} = \frac{2a_0\cos\alpha_1(u_0 + a_0)}{(u_1 + a_1\cos\alpha_1)\left(a_1 + a_0\left(\dfrac{u_0}{u_1}\right)\cos\alpha_1\right)} \tag{23}$$

In addition, the ratio of reflected acoustic disturbance strength to the known incident disturbance strength is given by

$$\frac{\dfrac{p_7'}{p_0} - \dfrac{p_6'}{p_0}}{\dfrac{p_6'}{p_0}} = \frac{(1 + M_{x0})(u_1 a_1 - u_0 a_0\cos\alpha_1)}{(1 - M_{x0})(u_1 a_1 + u_0 a_0\cos\alpha_1)} \tag{24}$$

Comparing with the data from the University of Cincinnati Mach 0.17 run presented in Figure 5, the reflected disturbance from the interaction of the incident disturbance with the inlet guide vanes was found to be very weak. The ratio given in Equation (24) was calculated to be approximately 0.02. This negligible amount of reflection off the inlet guide vanes agrees with the University of Cincinnati conclusion that the main reflection occurs at the first stage rotor.

After transmission through the inlet guide vanes, the acoustic disturbance travels downstream towards the first stage rotor. Figure 12 depicts the flow around the first stage rotor prior to the arrival of the inlet guide vanes' transmitted acoustic disturbance. The relative velocity vector measured with respect to the moving rotor $\overrightarrow{V_r}$ is given by

$$\overrightarrow{V_r} = \overrightarrow{V_a} - \overrightarrow{U} \tag{25}$$

where $\overrightarrow{V_a}$ is the absolute velocity measured with respect to the fixed reference frame of the compressor rig and $\overrightarrow{U}$ is rotor's blade velocity. The axial component of the velocity remains the same in both reference frames. The relative flow properties upstream of the rotor in region 1 are calculated using the known rotor blade speed U and the previously computed absolute flow conditions.

The relative Mach number M_{4r} downstream of the first stage rotor is calculated using the constant mass flow rate equation for the rotor blade passage.

$$\frac{S_1 p_{t1r} M_{1r} \cos\beta_1}{\left[1 + \frac{\gamma-1}{2} M_{1r}^2\right]^{\frac{\gamma+1}{2(\gamma-1)}}} = \frac{S_4 p_{t4r} M_{4r} \cos\beta_4}{\left[1 + \frac{\gamma-1}{2} M_{4r}^2\right]^{\frac{\gamma+1}{2(\gamma-1)}}} \tag{26}$$

where p_{tr} is the relative total pressure, β_1 is blade inlet angle, and β_4 is the blade exit angle. The relative total pressure ratio across the rotor passage is given by

$$\frac{p_{t4r}}{p_{t1r}} = 1 - \phi_{cr} \frac{\frac{\gamma}{2} M_{1r}^2}{\left[1 + \frac{\gamma-1}{2} M_{1r}^2\right]^{\frac{\gamma}{\gamma-1}}} \tag{27}$$

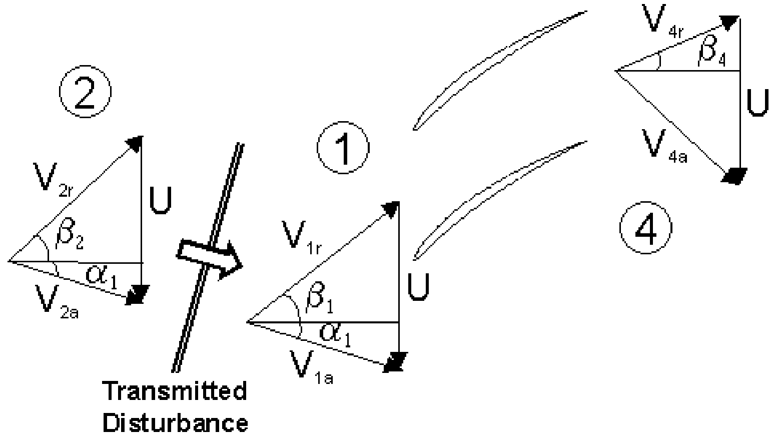

Figure 12: Flow Schematic of First Stage Rotor Prior to Arrival of Inlet Guide Vanes' Transmitted Acoustic Disturbance

where ϕ_{cr} is the rotor loss coefficient with a typical range in value from 0.05 to 0.12. This loss coefficient accounts for the non-isentropic flow through the rotor passage. Using the relative total pressure, relative Mach number, rotor blade speed, and exit blade angle, all of the remaining flow variables in region 4 are computed.

The result of the interaction of the transmitted acoustic disturbance with the first stage rotor is a reflected wave travelling upstream aligned with the exit angle of the inlet guide vanes and a transmitted wave travelling downstream aligned with the exit angle of the rotor. Figure 13 depicts the flow around the first stage rotor after its interaction with the transmitted acoustic wave.

The following small disturbance notation system is used to relate the flow properties in regions 1, 2, 3, 4, and 5 of Figures 12 and 13.

$$\begin{aligned}
p_2 &= p_1 + p_2' \qquad & u_2 &= u_1 + u_2' \qquad & \rho_2 &= \rho_1 + \rho_2' \\
p_3 &= p_1 + p_3' \qquad & u_3 &= u_1 + u_3' \qquad & \rho_3 &= \rho_1 + \rho_3' \\
p_5 &= p_4 + p_5' \qquad & u_5 &= u_4 + u_5' \qquad & \rho_5 &= \rho_4 + \rho_5'
\end{aligned} \tag{28}$$

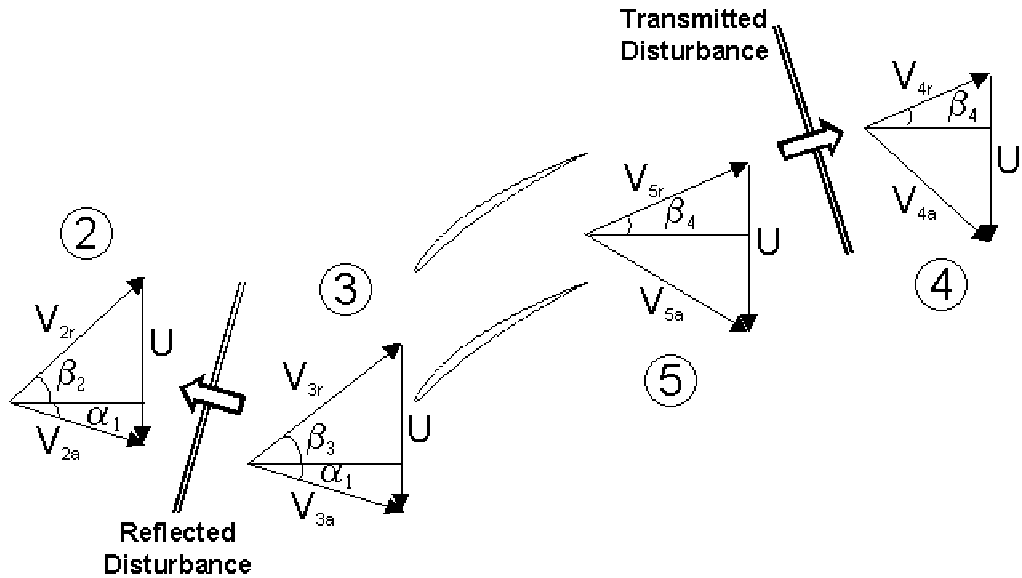

Figure 13: Flow Schematic of First Stage Rotor After Interaction With Inlet Guide Vanes' Transmitted Acoustic Disturbance

Regions 1 and 4 are designated as the reference states in front of and behind the first stage rotor, respectively.

Using Equations (2) and (28), the flow properties across the reflected acoustic disturbance from the rotor are given by

$$\frac{p_3'}{p_1} - \frac{p_2'}{p_1} = -\frac{\gamma M_{x1}}{\cos\alpha_1}\left(\frac{u_3'}{u_1} - \frac{u_2'}{u_1}\right) \tag{29}$$

This equation is simplified into the following form by substituting Equation (22) into it and rearranging.

$$\frac{p_3'}{p_1} + \frac{\gamma M_{x1}}{\cos\alpha_1}\frac{u_3'}{u_1} = 2\frac{p_2'}{p_1} \tag{30}$$

Assuming no time rate of change of mass, the continuity equation for a control volume fixed to the moving first stage rotor has the following form.

$$\rho_3' u_1 S_1 + \rho_1 u_3' S_1 \quad = \quad \rho_5' u_4 S_4 + \rho_4 u_5' S_4 \tag{31}$$

Using Equation (18) on either side of the rotor passage, Equation (31) is reduced to the following form.

$$\frac{p'_5}{p_4} + \gamma\frac{u'_5}{u_4} = \frac{p'_3}{p_1} + \gamma\frac{u'_3}{u_1} \tag{32}$$

Assuming no time rate of change of energy, the conservation of energy equation for this control volume fixed to the moving rotor is given by

$$\begin{aligned} h_{t5r} &= h_{t3r} \\ \frac{\gamma}{\gamma-1}\frac{p_5}{\rho_5} + \frac{1}{2}\left(u_5^2 + w_{5r}^2\right) &= \frac{\gamma}{\gamma-1}\frac{p_3}{\rho_3} + \frac{1}{2}\left(u_3^2 + w_{3r}^2\right) \end{aligned} \tag{33}$$

where $w_{5r} = u_5 \tan\beta_4$ and $w_{3r} = U - u_3 \tan\alpha_1$. Using Equation (18) on both sides of the rotor, Equation (33) is reduced to the following form.

$$\frac{p'_5}{\rho_4} + \frac{u'_5 u_4}{\cos^2\beta_4} = \frac{p'_3}{\rho_1} + \frac{u'_3 u_1}{\cos^2\alpha_1} - U u'_3 \tan\alpha_1 \tag{34}$$

Using Equations (1) and (28), the flow properties across the transmitted acoustic disturbance from the rotor are given by

$$\frac{p'_5}{p_4} = \frac{\gamma M_{x4}}{\cos\beta_4}\frac{u'_5}{u_4} \tag{35}$$

Equations (30), (32), (34), and (35) form a system of linear equations for four new unknowns p'_5, p'_3, u'_5, and u'_3. This linear system is solved to determine the ratio of the rotor's reflected acoustic disturbance strength to the inlet guide vanes' transmitted acoustic disturbance strength.

$$\frac{\dfrac{p'_3}{p_1} - \dfrac{p'_2}{p_1}}{\dfrac{p'_2}{p_1}} = \frac{(\cos\alpha_1 + M_{x1})(u_4 a_4 \cos\alpha_1 - u_1 a_1 \cos\beta_4) + U u_1 \sin\alpha_1 \cos\alpha_1 \cos\beta_4}{(\cos\alpha_1 - M_{x1})(u_4 a_4 \cos\alpha_1 + u_1 a_1 \cos\beta_4) + U u_1 \sin\alpha_1 \cos\alpha_1 \cos\beta_4} \tag{36}$$

Equation (36) can be reduced to Equation (8) for Paynter's reflection response coefficient if the turning of the flow by the inlet guide vanes is neglected ($\alpha_1 = 0$) and the blades are assumed to be flat plates ($u_1 a_1 = u_4 a_4$).

After the reflection from the first stage rotor, this reflected acoustic disturbance travels back upstream towards the inlet guide vanes. Figure 14 shows schematically the flow field around the inlet guide vanes prior to the arrival of the rotor's reflected acoustic disturbance. The result of the interaction of the acoustic disturbance with the inlet guide vanes is a transmitted wave travelling upstream through the inlet and a reflected wave travelling downstream aligned with the exit angle of the blade passage. Figure 15 depicts the flow around the inlet guide vanes after its interaction with the rotor's reflected acoustic wave.

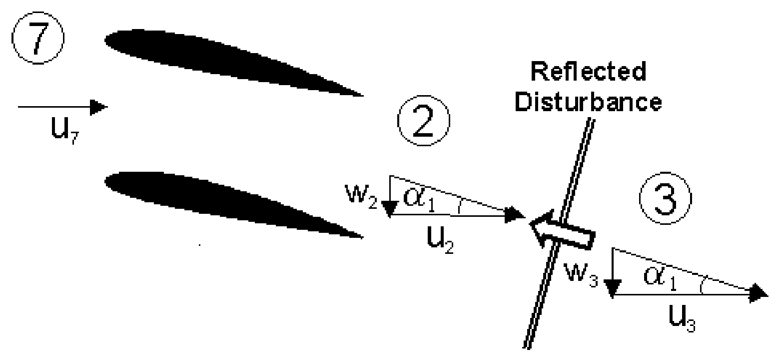

Figure 14: Flow Schematic of Inlet Guide Vanes Prior to Arrival of Rotor's Reflected Acoustic Disturbance

The following small disturbance notation system is used to relate the flow properties in regions 2, 3, 7, 8, and 9 of Figures 14 and 15.

$$\begin{array}{lll} p_2 = p_1 + p_2' & u_2 = u_1 + u_2' & \rho_2 = \rho_1 + \rho_2' \\ p_3 = p_1 + p_3' & u_3 = u_1 + u_3' & \rho_3 = \rho_1 + \rho_3' \\ p_9 = p_1 + p_9' & u_9 = u_1 + u_9' & \rho_9 = \rho_1 + \rho_9' \\ p_7 = p_0 + p_7' & u_7 = u_0 + u_7' & \rho_7 = \rho_0 + \rho_7' \\ p_8 = p_0 + p_8' & u_8 = u_0 + u_8' & \rho_8 = \rho_0 + \rho_8' \end{array} \tag{37}$$

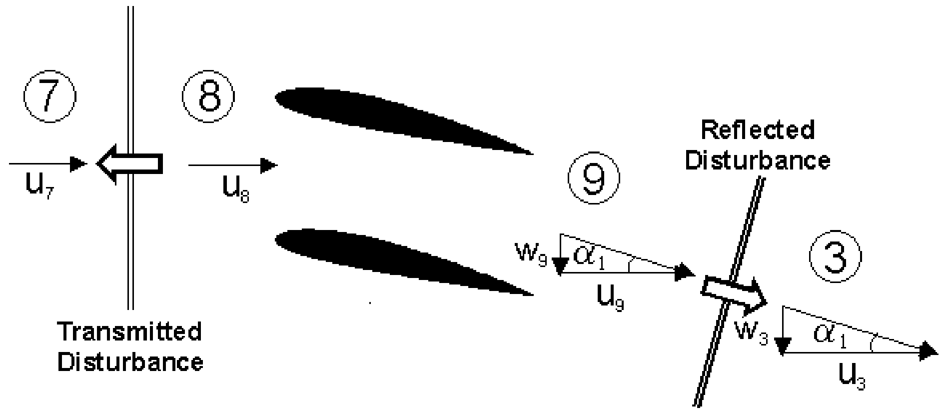

Figure 15: Flow Schematic of Inlet Guide Vanes After Interaction With Rotor's Reflected Acoustic Disturbance

Regions 0 and 1 are still designated as the reference states in front of and behind the inlet guide vanes, respectively.

Using Equations (1) and (37), the flow properties across the reflected acoustic disturbance are given by

$$\frac{p_9'}{p_1} - \frac{p_3'}{p_1} = \frac{\gamma M_{x1}}{\cos\alpha_1}\left(\frac{u_9'}{u_1} - \frac{u_3'}{u_1}\right) \tag{38}$$

This equation is simplified into the following form by substituting Equation (30) into it and rearranging.

$$\frac{p_9'}{p_1} + \frac{\gamma M_{x1}}{\cos\alpha_1}\frac{u_9'}{u_1} = 2\left(\frac{p_3'}{p_1} - \frac{p_2'}{p_1}\right) \tag{39}$$

Using the assumption of no time rate of change of mass, the continuity equation for a control volume fixed to the inlet guide vanes has the following form.

$$\rho_8' u_0 S_0 + \rho_0 u_8' S_0 \quad = \quad \rho_9' u_1 S_1 + \rho_1 u_9' S_1 \tag{40}$$

Using Equation (18) across the inlet guide vanes, Equation (40) is reduced to the following form.

$$\frac{p_8'}{p_0} + \gamma\frac{u_8'}{u_0} = \frac{p_9'}{p_1} + \gamma\frac{u_9'}{u_1} \tag{41}$$

Using the assumption of no time rate of change of energy, the conservation of energy equation for this control volume fixed to the blade passage is given by

$$\begin{aligned} h_{t8} &= h_{t9} \\ \frac{\gamma}{\gamma-1}\frac{p_8}{\rho_8} + \frac{1}{2}u_8^2 &= \frac{\gamma}{\gamma-1}\frac{p_9}{\rho_9} + \frac{1}{2}\left(u_9^2 + w_9^2\right) \end{aligned} \tag{42}$$

Using Equation (18) and the velocity component relation $w_9 = u_9 \tan\alpha_1$, Equation (42) is reduced to the following form.

$$\frac{p_8'}{\rho_0} + u_8' u_0 = \frac{p_9'}{\rho_1} + \frac{u_9' u_1}{\cos^2\alpha_1} \tag{43}$$

Using Equations (2) and (37), the flow properties across the transmitted acoustic disturbance are given by

$$\frac{p_8'}{p_0} - \frac{p_7'}{p_0} = -\gamma M_{x0}\left(\frac{u_8'}{u_0} - \frac{u_7'}{u_0}\right) \tag{44}$$

This equation is simplified into the following form by substituting Equation (16) into it and rearranging.

$$\frac{p_8'}{p_0} = -\gamma M_{x0}\frac{u_8'}{u_0} + 2\frac{p_6'}{p_0} \tag{45}$$

Equations (39), (41), (43), and (44) form a system of linear equations for four new unknowns p_8', p_9', u_8', and u_9'. This linear system is solved to determine an equation for the strength of the transmitted acoustic disturbance travelling upstream through the inlet.

$$\begin{aligned} \frac{p_8'}{p_0} = &\frac{[2(\cos\alpha_1 + M_{x1})(u_1 a_1 - u_0^2\cos\alpha_1)]}{[(1-M_{x0})(\cos\alpha_1 + M_{x1})(u_0 a_0\cos\alpha_1 + u_1 a_1)]}\frac{p_6'}{p_0} \\ &+ \frac{[2a_1^2 M_{x0}\cos\alpha_1(\cos\alpha_1 - M_{x1}^2)]}{[(1-M_{x0})(\cos\alpha_1 + M_{x1})(u_0 a_0\cos\alpha_1 + u_1 a_1)]}\left(\frac{p_3'}{p_1} - \frac{p_2'}{p_1}\right) \end{aligned} \tag{46}$$

Equations (23) and (36) are used to simplify the previous equation into an equation for the compressor response coefficient β. The response coefficient for this new small disturbance boundary condition is given by

$$\begin{aligned}\beta &= \frac{p_8 - p_6}{p_6 - p_0} \\ &= \left(\frac{1 + M_{x0}}{1 - M_{x0}}\right)\left(\frac{u_1 a_1 - u_0 a_0 \cos\alpha_1}{u_1 a_1 + u_0 a_0 \cos\alpha_1}\right) \\ &\quad + \left(\frac{1 + M_{x0}}{1 - M_{x0}}\right)\left(\frac{(\cos\alpha_1 - M_{x1}^2)}{(\cos\alpha_1 + M_{x1})^2}\frac{(4u_1 u_0 a_0 a_1 \cos^2\alpha_1)}{(u_1 a_1 + u_0 a_0 \cos\alpha_1)^2}\right) \\ &\quad * \left(\frac{(\cos\alpha_1 + M_{x1})(u_4 a_4 \cos\alpha_1 - u_1 a_1 \cos\beta_4) + U u_1 \sin\alpha_1 \cos\alpha_1 \cos\beta_4}{(\cos\alpha_1 - M_{x1})(u_4 a_4 \cos\alpha_1 + u_1 a_1 \cos\beta_4) + U u_1 \sin\alpha_1 \cos\alpha_1 \cos\beta_4}\right)\end{aligned} \tag{47}$$

This new formulation for the reflection response coefficient takes in account the turning of the flow through the inlet guide vanes and the camber and speed of the blades.

3.1.2 Model Implementation

The new small disturbance compressor face boundary condition was implemented into a CFD code similar to the process described by Paynter et. al.[20] First, the new reflection response coefficient β is calculated using Equation (47). This new response coefficient only depends on the flow conditions and geometry of the compressor prior to the arrival of the incident acoustic disturbance. The previous time level conditions at the compressor face boundary (region 0) and the geometry for the inlet guide vanes and first stage rotor varies in the radial direction. Therefore, the needed reference conditions in regions 1 and 4 of Figures 10 and 12 and β are calculated at each computational cell along the outflow boundary. For a one-dimensional model of the inlet, mean values of the compressor's geometry are used to calculate the response coefficient.

After calculating the new reflection response coefficient, the updated pressure at the boundary is calculated from Equation (10). Then, the remaining flow variables at the compressor face boundary are updated using the one dimensional positive eigenvalue compatibility equations given by

$$\frac{\partial \rho}{\partial t} - \frac{1}{a^2}\frac{\partial p}{\partial t} + u\left(\frac{\partial \rho}{\partial x} - \frac{1}{a^2}\frac{\partial p}{\partial x}\right) = 0$$
$$\frac{\partial u}{\partial t} + \frac{1}{\rho a}\frac{\partial p}{\partial t} + (u+a)\left(\frac{\partial u}{\partial x} + \frac{1}{\rho a}\frac{\partial p}{\partial x}\right) = 0 \tag{48}$$

and the equation for the advection of the radial velocity v given by

$$\frac{\partial v}{\partial t} + u\frac{\partial v}{\partial x} = 0 \tag{49}$$

3.2 Area Reduction Boundary Condition

For this simple compressor face boundary condition, the first stage rotor blades are modeled as flat plates. The flow in front of the downstream travelling acoustic disturbance is assumed to be aligned with the rotor blade passage. Figure 16 shows the frontal area open to the flow if the flow is aligned with the stagger angle Γ of the rotor blades. The frontal area the aligned flow saw as it entered the blade passage is given by

$$n_1 = s\cos\Gamma \tag{50}$$

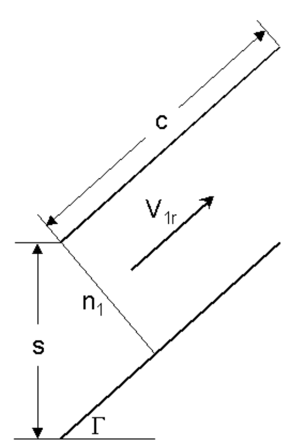

Figure 16: Frontal Area Open to Flow Aligned With Blade Passage

Behind the acoustic disturbance, the flow entering the blade passage is not aligned with the rotor blades. Therefore, the open frontal area seen by the flow is reduced. Figure 17 shows the reduced open frontal area for a flow that is not aligned with the blade passage. The shaded area represents the frontal area that the entering flow sees as closed. The frontal area that is closed to the non-aligned flow is given by

$$n_2 = c \tan|\beta_2 - \Gamma| \tag{51}$$

where β_2 is inlet flow angle.

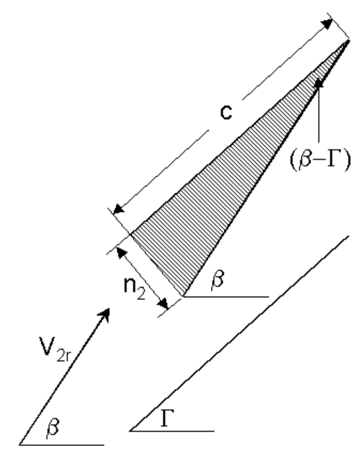

Figure 17: Frontal Area Open to Flow Not Aligned With Blade Passage

The area reduction boundary condition compares the open frontal area the flow after the disturbance sees to that seen by the flow in front of the acoustic disturbance. Using Equations (50) and (51), the relative amount of area reduction AR is given by

$$\begin{aligned} AR &= \frac{n_1 - n_2}{n_1} \\ &= 1 - \frac{c}{s}\frac{\tan|\beta_2 - \Gamma|}{\cos\Gamma} \end{aligned} \tag{52}$$

In order to implement this area reduction boundary condtion into a CFD code, the inlet domain is extended axially past the third stage rotor. In the axial direction, the cross-sectional area across the first stage rotor is reduced linearly by relative amount of area reduction calculated using Equation (52). The acoustic disturbance is reflected off this reduced cross-sectional area of the domain. In addition, a constant pressure boundary condition is applied at the exit of the domain. However, the reflection off this constant pressure boundary was far enough downstream that it did not interfere with the reflected disturbance from the area reduction section of the domain.

4 Governing Equations

Both one-dimensional and axisymmetric two-dimensional models were used to numerically simulate the compressor face boundary condition experiment at the University of Cincinnati. The one-dimensional model used the Euler equations in quasi one-dimensional form to calculate the unsteady flow in the inlet. The axisymmetric model employed the compressible Favre averaged Navier-Stokes equations to investigate the two-dimensional acoustic reflection of the axial compressor.

4.1 One-Dimensional Model Equations

4.1.1 Euler Equations

The Euler equations were derived from the universal laws of Conservation of Mass, Conservation of Momentum, and Conservation of Energy and governed the motion of an inviscid fluid. The quasi one-dimensional Euler equations, written in conservative form, with no body forces or external heat addition were as follows.

$$\frac{\partial (\mathbf{U}S)}{\partial t} + \frac{\partial (\mathbf{F}S)}{\partial x} = \mathbf{W} \tag{53}$$

where $\mathbf{U}$ was the vector of conservative variables

$$\mathbf{U} = \begin{bmatrix} \rho \\ \rho u \\ E_t \end{bmatrix} \tag{54}$$

$\mathbf{F}$ was the inviscid flux in the axial direction

$$\mathbf{F} = \begin{bmatrix} \rho u \\ \rho u^2 + p \\ (E_t + p)u \end{bmatrix} \tag{55}$$

$\mathbf{W}$ represented the source terms for the equations

$$\mathbf{W} = \begin{bmatrix} 0 \\ p\frac{\partial S}{\partial x} \\ -p\frac{\partial S}{\partial t} \end{bmatrix} \tag{56}$$

where $S(x,t)$ was the inlet cross-sectional area. The source term for the energy equation, $-p\frac{\partial S}{\partial t}$, accounted for the work done by the fluid on the bump as the bump deflated.

4.1.2 Ideal Gas Law

The three Euler equations contain three thermodynamic variables ρ, p, E_t as well as the axial velocity component u. Therefore, another equation was needed to close the system. Air was assumed to be a calorically perfect ideal gas for this work. Its thermodynamic variables were related by the following equation of state.

$$p = (\gamma - 1)(E_t - \frac{1}{2}\rho u^2) \tag{57}$$

where E_t was the total energy.

4.1.3 Geometry Equations

For the one-dimensional case, the geometry of the experimental set-up was modeled in Equation (53) by the axial coordinate x and the cross-sectional area S. The constant area annular duct containing the flexible bump was modeled using the duct and bump dimensions published by the University of Cincinnati.[9, 10, 11, 12, 16, 17] In addition, the constant area section of the duct was extended upstream 0.2266 m to account for the bellmouth entrance and 0.0319 m downstream to the mid-plan of the first stage rotor since Freund and Sajben had determined that the acoustic reflection in the experiments originated at this point.[11]

In order to account approximately for the pressure drop along the duct caused by turbulent boundary layer on both the hub and case, Schlichting's flat plate turbulent boundary layer displacement thickness model was employed.[23] The formula for the displacement thickness model was

$$\delta^* = \frac{0.37x}{8}\left(\frac{\rho u x}{\mu}\right)^{-0.20} \tag{58}$$

For the calculation of the cross-sectional area at each axial location, the displacement thickness was subtracted from the radius of the case and added to the radius of the hub or bump. Figure 18 shows the cross-sectional area of the numerical domain prior to the deflation of the flexible bump. The center of the flexible bump was located at 0.8918 m.

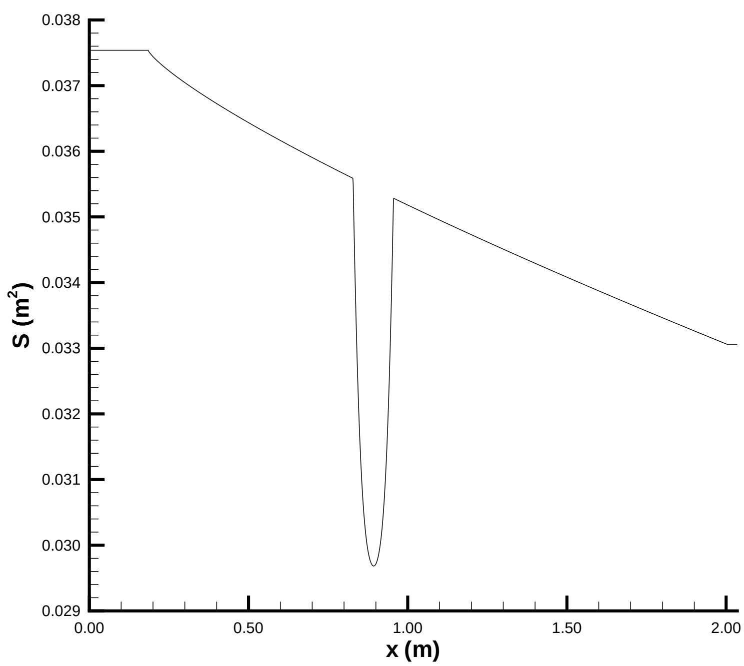

Figure 18: One-Dimensional Model Cross-Sectional Area

After investigating the experimental data from the collapse of the bump, Slater et. al. produced the following relation for the height of the center of the collapsing bump.[24]

$$h(t) = h_0 \left[\cos\left(\frac{\pi t}{2T} \right) \right]^{0.8} \tag{59}$$

where h_0 was the initial height before deflation and T was the duration time required for completely deflating the bump. Slater also stated that the bump collapsed with a uniform displacement at each axial location. This meant that the ends of the bump reached the hub first.

4.2 Axisymmetric Model Equations

4.2.1 Reynolds and Favre Averaging

In order to account for the effects of turbulence on the mean flow properties, the Navier-Stokes equations were modified by using Reynolds and Favre averaging.

For Reynolds averaging, the variables can be decomposed into mean and fluctuating components.[25] The following is an example of Reynolds averaging of the density.

$$\rho(x_i, t) = \overline{\rho}(x_i) + \rho'(x_i, t) \tag{60}$$

where the mean quantity $\overline{\rho}$ is defined as

$$\overline{\rho}(x_i) = \lim_{\Delta t \to \infty} \frac{1}{\Delta t} \int_t^{t+\Delta t} \rho(x_i, t) dt \tag{61}$$

To account for the the density variations in compressible flows, Favre averaging was used to simplify the averaging of the Navier-Stokes equations. For Favre averaging, a flow variable such as the axial flow velocity was decomposed into the sum of mean and fluctuating parts as follows.[25]

$$u(x_i, t) = \tilde{u}(x_i) + u''(x_i, t) \tag{62}$$

where the Favre averaged quantity $\tilde{u}(x_i)$ was defined as

$$\tilde{u}(x_i) = \frac{1}{\overline{\rho}} \lim_{\Delta t \to \infty} \frac{1}{\Delta t} \int_t^{t+\Delta t} \rho u(x_i, t) dt = \frac{\overline{\rho u}}{\overline{\rho}} \tag{63}$$

The following combination of Reynolds and Favre averaged quantities were used in the Favre averaged Navier-Stokes equations.

$$\begin{array}{ccc} \rho = \overline{\rho} + \rho' & p = \overline{p} + p' & q_i = \overline{q}_i + q_i' \\ u = \tilde{u} + u'' & v = \tilde{v} + v'' & \tau_{ij} = \overline{\tau}_{ij} + \tau_{ij}' \\ h_t = \tilde{h}_t + h_t'' & e_t = \tilde{e}_t + e_t'' & T = \tilde{T} + T'' \end{array} \tag{64}$$

4.2.2 Navier-Stokes Equations

The Favre averaged Navier-Stokes equations were derived from the universal laws of Conservation of Mass, Conservation af Momentum, and Conservation of Energy and governed the motion of a viscous turbulent flow. The axisymmetric Favre averaged Navier-Stokes equations, written in conservative form, with no body forces or external heat addition were as follows.

$$\frac{\partial\left(y\mathbf{U}\right)}{\partial t}+\frac{\partial\left[y\left(\mathbf{F}-\mathbf{F_v}\right)\right]}{\partial x}+\frac{\partial\left[y\left(\mathbf{G}-\mathbf{G_v}\right)\right]}{\partial y}=\mathbf{W} \tag{65}$$

where $\mathbf{U}$ was the vector of conservative variables

$$\mathbf{U}=\begin{bmatrix}\overline{\rho}\\ \overline{\rho}\tilde{u}\\ \overline{\rho}\tilde{v}\\ \overline{\rho}\tilde{e}_t\end{bmatrix} \tag{66}$$

$\mathbf{F}$ and $\mathbf{G}$ were the inviscid fluxes in the axial and radial directions, respectively

$$\mathbf{F}=\begin{bmatrix}\overline{\rho}\tilde{u}\\ \overline{\rho}\tilde{u}^2+\overline{p}\\ \overline{\rho}\tilde{u}\tilde{v}\\ \overline{\rho}\tilde{h}_t\tilde{u}\end{bmatrix}\quad \mathbf{G}=\begin{bmatrix}\overline{\rho}\tilde{v}\\ \overline{\rho}\tilde{u}\tilde{v}\\ \overline{\rho}\tilde{v}^2+\overline{p}\\ \overline{\rho}\tilde{h}_t\tilde{v}\end{bmatrix} \tag{67}$$

$\mathbf{F_v}$ and $\mathbf{G_v}$ were the viscous fluxes in the axial and radial directions, respectively

$$\mathbf{F_v}=\begin{bmatrix}0\\ \overline{\tau}_{xx}\\ \overline{\tau}_{xy}\\ \tilde{u}\overline{\tau}_{xx}+\tilde{v}\overline{\tau}_{xy}-\overline{q}_x\end{bmatrix}\quad \mathbf{G_v}=\begin{bmatrix}0\\ \overline{\tau}_{xy}\\ \overline{\tau}_{yy}\\ \tilde{u}\overline{\tau}_{xy}+\tilde{v}\overline{\tau}_{yy}-\overline{q}_y\end{bmatrix} \tag{68}$$

$\mathbf{W}$ represented the source terms for the axisymmetric equations

$$\mathbf{W}=\begin{bmatrix}0\\ 0\\ \overline{p}-\overline{\tau}_{\theta\theta}\\ 0\end{bmatrix} \tag{69}$$

and y was the radial distance from the centerline. The stress and heat flux terms in the above equations were given by

$$
\begin{aligned}
\overline{\tau}_{xx} &= \frac{2}{3}(\mu+\mu_T)\left(2\frac{\partial\tilde{u}}{\partial x}-\frac{\partial\tilde{v}}{\partial y}-\frac{\tilde{v}}{y}\right)\\
\overline{\tau}_{xy} &= (\mu+\mu_T)\left(\frac{\partial\tilde{u}}{\partial y}+\frac{\partial\tilde{v}}{\partial x}\right)\\
\overline{\tau}_{yy} &= \frac{2}{3}(\mu+\mu_T)\left(2\frac{\partial\tilde{v}}{\partial y}-\frac{\partial\tilde{u}}{\partial x}-\frac{\tilde{v}}{y}\right)\\
\overline{\tau}_{\theta\theta} &= \frac{2}{3}(\mu+\mu_T)\left(-\frac{\partial\tilde{u}}{\partial x}-\frac{\partial\tilde{v}}{\partial y}+2\frac{\tilde{v}}{y}\right)\\
\overline{q}_x &= -c_p\left(\frac{\mu}{Pr}+\frac{\mu_T}{Pr_T}\right)\frac{\partial\tilde{T}}{\partial x}\\
\overline{q}_y &= -c_p\left(\frac{\mu}{Pr}+\frac{\mu_T}{Pr_T}\right)\frac{\partial\tilde{T}}{\partial y}
\end{aligned}
\tag{70}
$$

where μ was the laminar viscosity, μ_T was the eddy viscosity, Pr was the laminar Prandtl number, Pr_T was the turbulent Prandtl number, and c_p was the constant pressure specific heat.

Physical domain grids usually have nonuniform grid spacing in one or more directions. Therefore, it was useful to transform the nonuniform physical grid to a uniformly distributed computational grid. This transform allowed the use of body-fitted coordinates which may not be orthogonal. The Navier-Stokes equations can be written for a generalized coordinate system (ξ,η) using the transformation of the form

$$
\begin{aligned}
\xi &= \xi(x,y,t)\\
\eta &= \eta(x,y,t)\\
\tau &= t
\end{aligned}
\tag{71}
$$

The differential expressions for this transformation to generalized coordinates were given by

$$\begin{aligned} d\xi &= \xi_x dx + \xi_y dy + \xi_t dt \\ d\eta &= \eta_x dx + \eta_y dy + \eta_t dt \\ d\tau &= dt \end{aligned} \tag{72}$$

Similarly, the differential expressions for the inverse transformation had the form

$$\begin{aligned} dx &= x_\xi d\xi + x_\eta d\eta + x_\tau d\tau \\ dy &= y_x i d\xi + y_\eta d\eta + y_\tau d\tau \\ dt &= d\tau \end{aligned} \tag{73}$$

Using Equations (72) and (73), the transformation metrics were defined as

$$\begin{aligned} \xi_x &= y_\eta J \\ \xi_y &= -x_\eta J \\ \eta_x &= -y_\xi J \\ \eta_y &= x_\xi J \end{aligned} \tag{74}$$

where the cell volume $\frac{1}{J}$ was defined as

$$\frac{1}{J} = x_\xi y_\eta - x_\eta y_\xi \tag{75}$$

Applying the chain rule of differentiation to Equation (65) and using the transformation metrics, the following axisymmetric Favre averaged Navier-Stokes equations written in strong conservation law form for the generalized coordinate system were derived.

$$\frac{\partial\left(y\hat{\mathbf{U}}\right)}{\partial\tau} + \frac{\partial\left(y\hat{\mathbf{F}}\right)}{\partial\xi} + \frac{\partial\left(y\hat{\mathbf{G}}\right)}{\partial\eta} = \hat{\mathbf{W}} \tag{76}$$

where

$$\begin{aligned}
\hat{\mathbf{U}} &= \frac{\mathbf{U}}{J} \\
\hat{\mathbf{F}} &= \frac{\mathbf{U}\xi_t + (\mathbf{F}-\mathbf{F_v})\,\xi_x + (\mathbf{G}-\mathbf{G_v})\,\xi_y}{J} \\
\hat{\mathbf{G}} &= \frac{\mathbf{U}\eta_t + (\mathbf{F}-\mathbf{F_v})\,\eta_x + (\mathbf{G}-\mathbf{G_v})\,\eta_y}{J} \\
\hat{\mathbf{W}} &= \frac{\mathbf{W}}{J}
\end{aligned} \tag{77}$$

4.2.3 Turbulence Modeling

The Spalart-Allmaras one-equation turbulence model was used to determine eddy viscosity.[26] The model included eight closure coefficients and three closure functions. The eddy viscosity was defined as

$$\mu_T = \overline{\rho}\tilde{\nu} f_{v1} \tag{78}$$

The equation for kinematic eddy viscosity was written as

$$\frac{\partial\tilde{\nu}}{\partial t} + \tilde{u}_j\frac{\partial\tilde{\nu}}{\partial x_j} = c_{b1}\tilde{S}\tilde{\nu} - c_{w1}f_w\left(\frac{\tilde{\nu}}{d}\right)^2 + \frac{1}{\sigma}\frac{\partial}{\partial x_k}\left[(\nu+\tilde{\nu})\frac{\partial\tilde{\nu}}{\partial x_k}\right] + \frac{c_{b2}}{\sigma}\frac{\partial\tilde{\nu}}{\partial x_k}\frac{\partial\tilde{\nu}}{\partial x_k} \tag{79}$$

with the following closure coefficients and functions

$$c_{b1} = 0.1355, \qquad c_{b2} = 0.622, \qquad c_{v1} = 7.1, \qquad \sigma = 2/3 \tag{80}$$

$$c_{w1} = \frac{c_{b1}}{\kappa^2} + \frac{1+c_{b2}}{\sigma}, \qquad c_{w2} = 0.3, \qquad c_{w3} = 2, \qquad \kappa = 0.41 \tag{81}$$

$$f_{v1} = \frac{\chi^3}{\chi^3 + c_{v1}^3}, \qquad f_{v2} = 1 - \frac{\chi}{1+\chi f_{v1}}, \qquad f_w = g\left[\frac{1+c_{w3}^6}{g^6+c_{w3}^6}\right]^{1/6} \tag{82}$$

$$\chi = \frac{\tilde{\nu}}{\nu}, \qquad g = r + c_{w2}(r^6 - r), \qquad r = \frac{\tilde{\nu}}{\tilde{S}\kappa^2 d^2} \tag{83}$$

$$\tilde{S} = \sqrt{2\Omega_{ij}\Omega_{ij}} + \frac{\tilde{\nu}}{\kappa^2 d^2} f_{v2} \tag{84}$$

The tensor $\Omega_{ij} = \frac{1}{2}(\partial\tilde{u}_i/\partial x_j - \partial\tilde{u}_j/\partial x_i)$ was the rotation tensor and d was distance from the closest wall. This equation was also transformed to generalized coordinates and solved in conjunction with the axisymmetric Favre averaged Navier-Stokes equations.

4.2.4 Ideal Gas Law and Sutherland Law

The four axisymmetric Navier-Stokes equations and the Spalart-Allmaras equation contained seven thermodynamic variables $\overline{\rho}, \overline{p}, \tilde{e}_t, \tilde{h}_t, \tilde{T}, \mu, \mu_T$ as well as the velocity components $\tilde{u}, \tilde{v}$. Therefore, four more equation were needed to close the system. Air was assumed to be a calorically perfect ideal gas for this work. Its thermodynamic variables were related by the following equations.

$$\begin{aligned} \overline{p} &= \overline{\rho} R \tilde{T} \\ \overline{\rho}\tilde{e}_t &= \frac{\overline{p}}{(\gamma - 1)} + \frac{1}{2}\overline{\rho}\left(\tilde{u}^2 + \tilde{v}^2\right) \\ \overline{\rho}\tilde{h}_t &= \overline{\rho}\tilde{e}_t + \overline{p} \end{aligned} \tag{85}$$

where $\tilde{e}_t$ was the total energy and $\tilde{h}_t$ was the total enthalpy.

In addition, Sutherland Law was used to determine the laminar viscosity as follows.[27]

$$\mu = 1.716 \times 10^{-5} \left(\frac{\tilde{T}}{273}\right)^{3/2} \frac{384}{\tilde{T} + 111} \tag{86}$$

4.2.5 Geometry Description

For the axisymmetric two-dimensional case, the geometry of the experimental set-up was modeled in Equation (65) by the axial coordinate x and the radial coordinate y. Again, the constant annular duct containing the flexible bump was modeled using the dimensions provided by the University of Cincinnati. In addition, the constant area section of the duct was extended upstream 0.05 m to account for the development of the turbulent boundary on the bellmouth entrance and 0.0319 m downstream to the mid-plan of the first stage rotor. Equation (59) was again used to model the deflating bump from the University of Cincinnati experiment. The bump collapsed with a uniform displacement at each axial location such that the ends of the bump reached the hub first.

5 Numerical Implementation

In the following sections, the numerical algorithms employed for the solutions of the quasi one-dimensional Euler equations and the axisymmetric Navier-Stokes equations are presented. These include the flux differencing schemes, time integration schemes, and boundary conditions implementations.

5.1 One-Dimensional Numerical Algorithms

A cell-centered finite-volume approach was used to solve the one-dimensional model. The domain interval $[0, L]$ was divided into N cells of length Δx, with cell centers x_i and cell faces $x_{i\pm1/2}$. The finite-volume discretization of Equation (53) had the form

$$\begin{aligned}
\frac{(S\mathbf{U})_i^{n+1} - (S\mathbf{U})_i^n}{\Delta t} &= -\mathbf{R}(\mathbf{U})_i^n \qquad (87)\\
\mathbf{R}(\mathbf{U})_i^n &= \frac{S_{i+1/2}^n \mathbf{F}_{i+1/2}^n - S_{i-1/2}^n \mathbf{F}_{i-1/2}^n}{\Delta x} - \begin{bmatrix} 0 \\ p_i \dfrac{S_{i+1/2}^n - S_{i-1/2}^n}{\Delta x} \\ -p_i \dfrac{S_i^{n+1} - S_i^n}{\Delta t} \end{bmatrix}
\end{aligned}$$

where $\mathbf{R}(\mathbf{U})$ was the residual vector and n represented the time level.

5.1.1 Roe's Flux Differencing Scheme

The flux vector $\mathbf{F}$ in the residual vector of Equation (87) was discretized using Roe's upwind method with minmod limited MUSCL variable extrapolation.[28, 29] The cell interface flux for Roe's method was given by

$$\mathbf{F}_{i+1/2} = \frac{1}{2}\left[\mathbf{F}(\mathbf{U}_L) + \mathbf{F}(\mathbf{U}_R) - |\bar{\bar{\mathbf{A}}}|(\mathbf{U}_R - \mathbf{U}_L)\right]_{i+1/2} \qquad (88)$$

where $\mathbf{A} = \frac{\partial \mathbf{F}}{\partial \mathbf{U}}$ was the Jacobian matrix of the Euler flux and the subscripts L and R were used to designate the left and right cell interface states, respectively. The Roe matrix $\bar{\bar{\mathbf{A}}}$ was evaluated using the Roe averaged variables given by

$$\begin{aligned}
R_{i+1/2} &= \sqrt{\frac{\rho_R}{\rho_L}} \\
\bar{\bar{\rho}}_{i+1/2} &= \rho_L R_{i+1/2} \\
\bar{\bar{u}}_{i+1/2} &= \frac{R_{i+1/2} u_R + u_L}{R_{i+1/2} + 1} \\
\bar{\bar{H}}_{i+1/2} &= \frac{R_{i+1/2} H_R + H_L}{R_{i+1/2} + 1} \\
\bar{\bar{a}}^2_{i+1/2} &= (\gamma - 1)(\bar{\bar{H}}_{i+1/2} - \frac{1}{2}\bar{\bar{u}}^2_{i+1/2})
\end{aligned} \tag{89}$$

where H was the total enthalpy defined by

$$H = \frac{\gamma}{\gamma - 1}\frac{p}{\rho} + \frac{1}{2}u^2 \tag{90}$$

The Roe vector in Equation (88) was evaluated as follows.

$$|\bar{\bar{\mathbf{A}}}|(\mathbf{U}_R - \mathbf{U}_L) = \sum_{j=1}^{3}\left(|\bar{\bar{\lambda}}_j| \cdot \partial w_j \cdot \bar{\bar{r}}^{(j)}\right) \tag{91}$$

where $\bar{\bar{\lambda}}_j$ were the eigenvalues of the Roe matrix

$$\bar{\bar{\lambda}}_1 = \bar{\bar{u}}, \quad \bar{\bar{\lambda}}_2 = \bar{\bar{u}} + \bar{\bar{a}}, \quad \bar{\bar{\lambda}}_3 = \bar{\bar{u}} - \bar{\bar{a}} \tag{92}$$

$\bar{\bar{r}}^{(j)}$ were the corresponding eigenvectors

$$\bar{\bar{r}}^{(1)} = \begin{bmatrix} 1 \\ \bar{\bar{u}} \\ \frac{\bar{\bar{u}}^2}{2} \end{bmatrix}, \quad \bar{\bar{r}}^{(2)} = \begin{bmatrix} 1 \\ \bar{\bar{u}} + \bar{\bar{a}} \\ \bar{\bar{H}} + \bar{\bar{u}}\bar{\bar{a}} \end{bmatrix} \frac{\bar{\bar{\rho}}}{2\bar{\bar{a}}}, \quad \bar{\bar{r}}^{(3)} = -\begin{bmatrix} 1 \\ \bar{\bar{u}} - \bar{\bar{a}} \\ \bar{\bar{H}} - \bar{\bar{u}}\bar{\bar{a}} \end{bmatrix} \frac{\bar{\bar{\rho}}}{2\bar{\bar{a}}} \tag{93}$$

and ∂w_j were the wave amplitudes

$$\partial w_1 = \delta\rho - \frac{\delta p}{\bar{\bar{a}}^2}, \quad \partial w_2 = \delta u + \frac{\delta p}{\bar{\bar{\rho}}\bar{\bar{a}}}, \quad \partial w_3 = \delta u - \frac{\delta p}{\bar{\bar{\rho}}\bar{\bar{a}}} \tag{94}$$

A problem with Roe's method is that it can admit an expansion shock as a solution to the Euler equations. The easiest way to handle this problem is to add some numerical dissipation in the calculation of the eigenvalues. Harten and Hyman[30] proposed to replace the absolute value of the each eigenvalue in Equation (91) with

$$|\bar{\bar{\lambda}}|_{mod} = \begin{cases} |\bar{\bar{\lambda}}|_{i+1/2} & \text{if } |\bar{\bar{\lambda}}|_{i+1/2} \geq \epsilon \\ \dfrac{1}{2}\left(\dfrac{\bar{\bar{\lambda}}^2_{i+1/2}}{\epsilon} + \epsilon\right) & \text{if } |\bar{\bar{\lambda}}|_{i+1/2} < \epsilon \end{cases} \tag{95}$$

where ϵ was defined as follows.

$$\epsilon = \max\left[0, (\bar{\bar{\lambda}}_{i+1/2} - \lambda_i), (\lambda_{i+1} - \bar{\bar{\lambda}}_{i+1/2})\right] \tag{96}$$

In order to achieve a higher order of accuracy, variable extrapolation of the primitive variable values to the left and right cell interface states was needed. The primitive variable vector was given by

$$\mathbf{V} = \begin{bmatrix} \rho \\ u \\ p \end{bmatrix} \tag{97}$$

The higher order left and right cell interface values of the primitive variables were calculated using a relaxed minmod limited MUSCL variable extrapolation.[31]

$$\begin{aligned}
(\mathbf{V}_L)_{i+1/2} &= \mathbf{V}_i + \frac{1}{4}[(1-\kappa)\overline{\delta^-}\mathbf{V}_i + (1+\kappa)\overline{\delta^+}\mathbf{V}_i] \\
(\mathbf{V}_R)_{i+1/2} &= \mathbf{V}_{i+1} - \frac{1}{4}[(1+\kappa)\overline{\delta^-}\mathbf{V}_{i+1} + (1-\kappa)\overline{\delta^+}\mathbf{V}_{i+1}] \\
\delta^-\mathbf{V}_i &= \mathbf{V}_i - \mathbf{V}_{i-1} \\
\delta^+\mathbf{V}_i &= \mathbf{V}_{i+1} - \mathbf{V}_i \\
\overline{\delta^-}\mathbf{V} &= \text{minmod}\left(\delta^-\mathbf{V}, \delta^+\mathbf{V}, \omega\right) \\
\overline{\delta^+}\mathbf{V} &= \text{minmod}\left(\delta^+\mathbf{V}, \delta^-\mathbf{V}, \omega\right) \\
\text{minmod}(b, c, \omega) &= \frac{1}{2}\left(\text{sign}(b) + \text{sign}(c)\right)\min(|b|, |\omega c|) \\
\kappa &= \frac{1}{3} \\
\omega &= 1.7
\end{aligned} \tag{98}$$

The operators δ^+ and δ^- were the forward difference and backward difference operators, respectively. The constant ω was a relaxation factor to reduce the diffusive nature of the minmod limiter. For the first order calculations, the left and right cell interface values were set equal to the i and $i+1$ cell centered values, respectively.

5.1.2 Steady State Implicit Integration Scheme

For the steady state time integration of Equation (87), the cross-sectional area S of the annular duct varied only with respect to the axial location x. Therefore, the source term in the energy equation was zero. In order to reduce the time required to reach steady state convergence, a pseudo-transient continuation method was used for the implicit time integration of the one-dimensional model.[32, 33, 34] The pseudo-transient algorithm had the form

$$\left(\frac{\partial \mathbf{R}^m}{\partial \mathbf{U}} + \frac{S}{\Delta_m t}\mathbf{I}\right)\Delta^m \mathbf{U} = -\mathbf{R}(\mathbf{U})^m \tag{99}$$

where $\Delta^m \mathbf{U}$ was the conservative variable vector step size given by

$$\Delta^m \mathbf{U} = \mathbf{U}^{m+1} - \mathbf{U}^m \tag{100}$$

and m represented the implicit iteration level. This time marching method sacrifices temporal accuracy for rapid convergence to steady state by varying the size of the time step $\Delta_m t$. Kelley's implementation of the GMRES algorithm was used to calculate the conservative variable vector step size for each iteration.[35, 36]

The residual vector on the right hand side of Equation (99) was discretized using Roe's flux difference scheme. The minmod slope limiter in the MUSCL variable extrapolation is a source of nonsmoothness for this flux discretization. Therefore, a smooth first order Lax-Freidrichs discretization of fluxes was used to construct an approximate Jacobian $\frac{\partial \mathbf{R}^m}{\partial \mathbf{U}}$ on the left side of the equation. Lax-Freidrichs flux discretization had the form

$$\mathbf{F}_{i+1/2} = \frac{1}{2}\left[\mathbf{F}_{i+1} + \mathbf{F}_i - |\lambda|_{i+1/2}(\mathbf{U}_{i+1} - \mathbf{U}_i)\right] \tag{101}$$

where $|\lambda| = |u| + a$.

5.1.3 Time Accurate Runge-Kutta Integration Scheme

For the unsteady time integration of Equation (87), the new cross-sectional area S^{n+1} over the collapsing bump was calculated using the new bump height given by Equation (59). In order to insure the time accuracy of the unsteady inlet flow simulation, an explicit, multi-stage Runge-Kutta integration algorithm was chosen.[37] This scheme provided higher order time accuracy by calculating the residual vector $\mathbf{R}$ in Equation (87) at several different values of $\mathbf{U}$ in the time interval Δt and combining these calculations to get $\mathbf{U}^{n+1}$. The four-stage Runge-Kutta scheme employed for the higher order calculations had the following form.

$$\begin{aligned}
\mathbf{U}_i^{(0)} &= \mathbf{U}_i^n \\
\mathbf{U}_i^{(1)} &= \frac{(S\mathbf{U})_i^n}{S_i^{(1)}} - \frac{\Delta t}{4}\frac{\mathbf{R}(\mathbf{U})_i^{(0)}}{S_i^{(1)}} \\
\mathbf{U}_i^{(2)} &= \frac{(S\mathbf{U})_i^n}{S_i^{(2)}} - \frac{\Delta t}{3}\frac{\mathbf{R}(\mathbf{U})_i^{(1)}}{S_i^{(2)}} \\
\mathbf{U}_i^{(3)} &= \frac{(S\mathbf{U})_i^n}{S_i^{(3)}} - \frac{\Delta t}{2}\frac{\mathbf{R}(\mathbf{U})_i^{(2)}}{S_i^{(3)}} \\
\mathbf{U}_i^{n+1} &= \frac{(S\mathbf{U})_i^n}{S_i^{n+1}} - \Delta t\frac{\mathbf{R}(\mathbf{U})_i^{(3)}}{S_i^{n+1}}
\end{aligned} \tag{102}$$

For the first order time accurate calculations, an Euler explicit time integration scheme was employed.

5.1.4 Boundary Conditions

For subsonic inflow, two physical conditions and one numerical condition must be specified at the boundary to the domain. For each experimental run at the University of Cincinnati, total pressure and total temperature were recorded.[11] Therefore, a constant total pressure and temperature were enforced physically at the inflow boundary. The axial velocity was linearly extrapolated from the domain at each time step. From these conditions, the density and pressure at the inflow boundary were calculated.

For a subsonic outflow boundary, one physical condition and two numerical conditions must be specified. For steady state time integration, a constant Mach number boundary condition was enforced. For the unsteady time integration, common subsonic outflow boundary conditions of constant Mach number, constant pressure, and constant axial velocity were employed. In addition, the Paynter small disturbance, Sajben small disturbance, and new small disturbance boundary conditions were applied using Equations (10) and (48). The reflection of the incident acoustic disturbance created by each of these outflow boundary conditions was compared with the experimental data from the University of Cincinnati to determine which one best modeled the reflection characteristics of an axial compressor.

5.2 Axisymmetric Numerical Algorithms

A cell-centered finite-volume approach was also used to solve the axisymmetric model. A physical grid was developed for the annular inlet using equal spacing of mesh points along the axial direction and clustering of points near the hub and case for turbulent flow. This physical grid had 378×81 mesh points. Figure 19 shows the clustering of the grid lines over the bump. Equation (74) was used to transform the unevenly spaced physical grid into an evenly spaced body-fitted computational mesh. The body surfaces of the hub and case were η = constant surfaces. The finite-volume

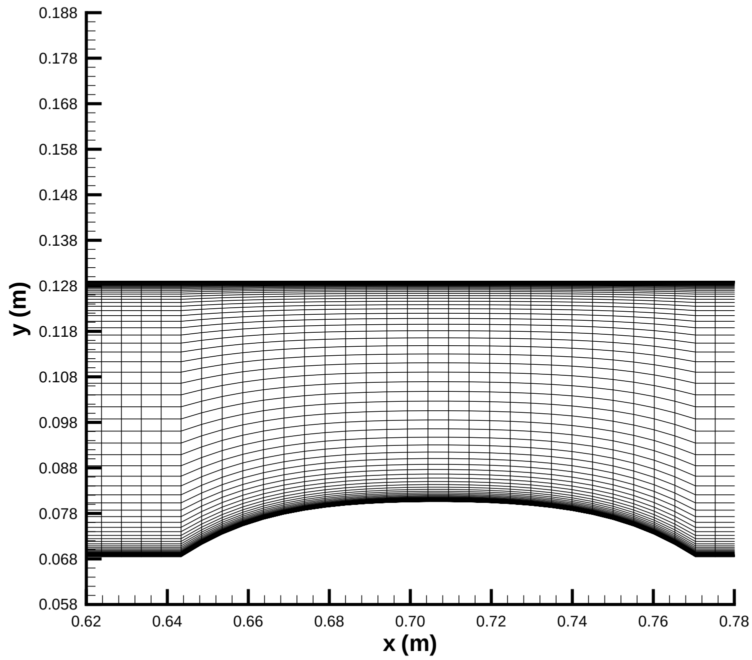

Figure 19: Axisymmetric Physical Grid Over the Bump

discretization of Equation (76) had the form

$$\begin{aligned}\frac{\left(\dfrac{y\mathbf{U}}{J}\right)^{n+1}_{i,j}-\left(\dfrac{y\mathbf{U}}{J}\right)^{n}_{i,j}}{\Delta t}&=-\mathbf{R}(\mathbf{U})^n_{i,j}\\ \mathbf{R}(\mathbf{U})^n_{i,j}&=(y\hat{\mathbf{F}})^n_{i+1/2,j}-(y\hat{\mathbf{F}})^n_{i-1/2,j}+(y\hat{\mathbf{G}})^n_{i,j+1/2}\\ &\quad-(y\hat{\mathbf{G}})^n_{i,j-1/2}-\hat{\mathbf{W}}^n_{i,j}\end{aligned} \tag{103}$$

The indices (i,j) represented the cell center values, and the indices $(i \pm 1/2, j)$ and $(i, j \pm 1/2)$ represented the right/left and top/bottom cell interfaces, respectively.

5.2.1 Flux Representation

The flux definitions for $\hat{\mathbf{F}}$ and $\hat{\mathbf{G}}$ given in Equation (77) contained inviscid, viscous, and grid movement components in the ξ and η directions, respectively.

The inviscid portion of the flux vectors $\hat{\mathbf{F}}$ and $\hat{\mathbf{G}}$ had the following forms. For clarity, the superscripts denoting the Favre- and Reynolds-averaged quantities will be omitted for the remainder of this dissertation.

$$\hat{\mathbf{F}}^I = \frac{1}{J}\begin{bmatrix} \rho\mathcal{U} \\ \rho\mathcal{U}u + \xi_x p \\ \rho\mathcal{U}v + \xi_y p \\ \rho\mathcal{U}h_t \end{bmatrix} \tag{104}$$
$$\hat{\mathbf{G}}^I = \frac{1}{J}\begin{bmatrix} \rho\mathcal{V} \\ \rho\mathcal{V}u + \eta_x p \\ \rho\mathcal{V}v + \eta_y p \\ \rho\mathcal{V}h_t \end{bmatrix}$$

$\mathcal{U}$ and $\mathcal{V}$ were contravariant velocity components in the ξ and η directions,respectively. These contravariant velocity components were defined as

$$\begin{aligned} \mathcal{U} &= \xi_x u + \xi_y v \\ \mathcal{V} &= \eta_x u + \eta_y v \end{aligned} \tag{105}$$

The inviscid portions of residual flux vectors in Equation (103) were discretized using Roe's upwind method with minmod limited MUSCL variable extrapolation.[28, 29] Roe's algorithm is an upwinding scheme in one dimension which is applied to both generalized coordinate directions independently. In this section, Roe's scheme is applied to the inviscid flux in ξ direction. The cell interface flux for Roe's method was given by

$$\hat{\mathbf{F}}^I_{i+1/2,j} = \frac{1}{2}\left[\mathbf{F}^I(\mathbf{U}_L) + \mathbf{F}^I(\mathbf{U}_R) - |\bar{\bar{\mathbf{A}}}|(\mathbf{U}_R - \mathbf{U}_L)\right]_{i+1/2,j} \tag{106}$$

In order to achieve a higher order of spatial accuracy, variable extrapolation of the primitive variable vector to the left and right cell interface states was needed. The primitive variable vector was given by

$$\mathbf{V} = \begin{bmatrix} \rho \\ u \\ v \\ p \end{bmatrix} \tag{107}$$

The higher order left and right cell interface values of the primitive variables were calculated using Equation (98) with $\omega = 1.0$.

The Roe vector in Equation (106) was given by

$$|\bar{\bar{\mathbf{A}}}|(\mathbf{U}_R - \mathbf{U}_L) = \begin{bmatrix} \alpha_4 \\ \bar{\bar{u}}\alpha_4 + k_x\alpha_5 + \alpha_6 \\ \bar{\bar{v}}\alpha_4 + k_y\alpha_5 + \alpha_7 \\ \bar{\bar{H}}\alpha_4 + \hat{\bar{u}}\alpha_5 + \bar{\bar{u}}\alpha_6 + \bar{\bar{v}}\alpha_7 - \dfrac{\bar{\bar{a}}^2}{\gamma - 1}\alpha_1 \end{bmatrix} \tag{108}$$

where

$$\begin{aligned}
\alpha_1 &= \frac{|\nabla\xi|}{J}|\hat{\bar{u}}|\left(\Delta\rho - \frac{\Delta p}{\bar{\bar{a}}^2}\right) \\
\alpha_2 &= \frac{1}{2\bar{\bar{a}}^2}\frac{|\nabla\xi|}{J}|\hat{\bar{u}} + \bar{\bar{a}}|(\Delta p + \bar{\bar{\rho}}\bar{\bar{a}}\Delta\hat{u}) \\
\alpha_3 &= \frac{1}{2\bar{\bar{a}}^2}\frac{|\nabla\xi|}{J}|\hat{\bar{u}} - \bar{\bar{a}}|(\Delta p - \bar{\bar{\rho}}\bar{\bar{a}}\Delta\hat{u}) \\
\alpha_4 &= \alpha_1 + \alpha_2 + \alpha_3 \\
\alpha_5 &= \bar{\bar{a}}(\alpha_2 - \alpha_3) \\
\alpha_6 &= \frac{|\nabla\xi|}{J}|\hat{\bar{u}}|(\bar{\bar{\rho}}\Delta u - k_x\bar{\bar{\rho}}\Delta\hat{u}) \\
\alpha_7 &= \frac{|\nabla\xi|}{J}|\hat{\bar{u}}|(\bar{\bar{\rho}}\Delta v - k_y\bar{\bar{\rho}}\Delta\hat{u})
\end{aligned} \tag{109}$$

The geometry and normal velocity terms in the previous equations were defined as

$$\begin{aligned}
k_x &= \frac{\xi_x}{|\nabla\xi|} \\
k_y &= \frac{\xi_y}{|\nabla\xi|} \\
\hat{u} &= k_x u + k_y v
\end{aligned} \tag{110}$$

The Roe averaged variables used in Equations (108) and (109) were defined as

$$
\begin{aligned}
R_{i+1/2} &= \sqrt{\frac{\rho_R}{\rho_L}} \\
\bar{\bar{\rho}}_{i+1/2} &= \rho_L R_{i+1/2} \\
\bar{\bar{u}}_{i+1/2} &= \frac{R_{i+1/2} u_R + u_L}{R_{i+1/2} + 1} \\
\hat{\bar{u}}_{i+1/2} &= \frac{R_{i+1/2} \hat{u}_R + \hat{u}_L}{R_{i+1/2} + 1} \\
\bar{\bar{v}}_{i+1/2} &= \frac{R_{i+1/2} v_R + v_L}{R_{i+1/2} + 1} \\
\bar{\bar{H}}_{i+1/2} &= \frac{R_{i+1/2} H_R + H_L}{R_{i+1/2} + 1} \\
\bar{\bar{a}}^2_{i+1/2} &= (\gamma - 1)[\bar{\bar{H}}_{i+1/2} - \frac{1}{2}(\bar{\bar{u}}^2_{i+1/2} + \bar{\bar{v}}^2_{i+1/2})]
\end{aligned}
\tag{111}
$$

Again, Equation (95) was used to handle this method's problem of creating non-physical expansion shocks.

For the axisymmetric grid, a thin-layer approximation was made to the viscous flux vectors defined in Equations (70) and (77) by neglecting the derivatives in the stress tensor corresponding to the ξ direction.[31] In addition, the viscous flux in the ξ direction was ignored. Therefore, the viscous portion of the flux vector $\hat{\mathbf{G}}$ in Equation (103) was reduced to the following form.

$$
\hat{\mathbf{G}}^V_{i,j+1/2} = J \begin{bmatrix} 0 \\ \frac{\eta_x}{J}\tau^{TL}_{xx} + \frac{\eta_y}{J}\tau^{TL}_{xy} \\ \frac{\eta_x}{J}\tau^{TL}_{xy} + \frac{\eta_y}{J}\tau^{TL}_{yy} \\ \frac{\eta_x}{J}(u\tau^{TL}_{xx} + v\tau^{TL}_{xy} - q^{TL}_x) + \frac{\eta_y}{J}(u\tau^{TL}_{xy} + v\tau^{TL}_{yy} - q^{TL}_y) \end{bmatrix}_{i,j+1/2}
\tag{112}
$$

where

$$
\begin{aligned}
\tau_{xx}^{TL} &= \frac{2}{3}(\mu+\mu_T)\left[2\frac{\eta_x}{J}\frac{\partial u}{\partial \eta} - \frac{\eta_y}{J}\frac{\partial v}{\partial \eta} - \frac{1}{J}\frac{v}{y}\right] \\
\tau_{xy}^{TL} &= (\mu+\mu_T)\left[\frac{\eta_y}{J}\frac{\partial u}{\partial \eta} + \frac{\eta_x}{J}\frac{\partial v}{\partial \eta}\right] \\
\tau_{yy}^{TL} &= \frac{2}{3}(\mu+\mu_T)\left[2\frac{\eta_y}{J}\frac{\partial v}{\partial \eta} - \frac{\eta_x}{J}\frac{\partial u}{\partial \eta} - \frac{1}{J}\frac{v}{y}\right] \\
q_x^{TL} &= -c_p\left(\frac{\mu}{Pr}+\frac{\mu_T}{Pr_T}\right)\frac{\eta_x}{J}\frac{\partial T}{\partial \eta} \\
q_y^{TL} &= -c_p\left(\frac{\mu}{Pr}+\frac{\mu_T}{Pr_T}\right)\frac{\eta_y}{J}\frac{\partial T}{\partial \eta}
\end{aligned}
\tag{113}
$$

Central differences about the cell interface were used for the partial differentials in Equation (113). In addition, the thin layer approximation was applied the stress tensor source term in Equations (70) and (77). The thin layer source stress term had the form

$$
\frac{1}{J}\tau_{\theta\theta}^{TL} = \frac{2}{3}(\mu+\mu_T)\left[-\frac{\eta_x}{J}\frac{\partial u}{\partial \eta} - \frac{\eta_y}{J}\frac{\partial v}{\partial \eta} + 2\frac{1}{J}\frac{v}{y}\right] \tag{114}
$$

The grid movement portion of the flux vectors $\hat{\mathbf{F}}$ and $\hat{\mathbf{G}}$ in Equation (77) contained the grid movement metrics $\frac{\xi_t}{J}$ and $\frac{\eta_t}{J}$, respectively. These metrics were defined as follows

$$
\begin{aligned}
\frac{\xi_t}{J} &= -\frac{\Delta x}{\Delta t}\frac{\xi_x}{J} - \frac{\Delta y}{\Delta t}\frac{\xi_y}{J} \\
\frac{\eta_t}{J} &= -\frac{\Delta x}{\Delta t}\frac{\eta_x}{J} - \frac{\Delta y}{\Delta t}\frac{\eta_y}{J}
\end{aligned}
\tag{115}
$$

5.2.2 Runge-Kutta Time Integration

The steady and unsteady time integration of Equation (103) used a two-stage Runge-Kutta scheme for the higher order calculations.[37] This time integration scheme had the following form.

$$
\begin{aligned}
\mathbf{U}_{i,j}^{(0)} &= \mathbf{U}_{i,j}^{n} \\
\mathbf{U}_{i,j}^{(1)} &= \frac{\left(\dfrac{y\mathbf{U}}{J}\right)_{i,j}^{n}}{\left(\dfrac{y}{J}\right)_{i,j}^{(1)}} - \frac{\Delta t}{2}\frac{\mathbf{R}(\mathbf{U})_{i,j}^{(0)}}{\left(\dfrac{y}{J}\right)_{i,j}^{(1)}} \\
\mathbf{U}_{i,j}^{n+1} &= \frac{\left(\dfrac{y\mathbf{U}}{J}\right)_{i,j}^{n}}{\left(\dfrac{y}{J}\right)_{i,j}^{n+1}} - \Delta t\frac{\mathbf{R}(\mathbf{U})_{i,j}^{(1)}}{\left(\dfrac{y}{J}\right)_{i,j}^{n+1}}
\end{aligned}
\tag{116}
$$

For the first order time accurate calculations, an Euler explicit time integration scheme was employed.

5.2.3 Boundary Conditions

For the axisymmetric model inflow, a constant total temperature and mass flow rate were enforced physically at the boundary. In addition, the radial velocity was set equal to zero along the boundary, and the pressure was linearly extrapolated from the interior of the inlet. From these conditions, the axial velocity and density at the inflow boundary were calculated.

For steady state time integration, a constant pressure boundary condition was enforced along the outflow boundary. For the unsteady time integration, the Paynter small disturbance and new small disturbance boundary conditions were applied at the outflow boundary using Equations (10), (48), and (49). Again, the reflection of the incident acoustic disturbance created by each of these outflow boundary conditions was compared with the experimental data from the University of Cincinnati to determine which one best modeled the reflection characteristics of an axial compressor.

A non-slip wall boundary condition was applied at the solid walls of the case and the hub. However, the normal non-slip wall boundary condition was modified for the flexible bump boundary to account for the bump movement. This modified non-slip boundary condition had the following form along the bump.

$$\vec{V} = \vec{g} \tag{117}$$

$\vec{V}$ was the flow velocity at the wall, and $\vec{g} = x_t\hat{i} + y_t\hat{j}$ was grid speed vector of the collapsing bump. This boundary condition provides the mechanism for the flow to sense the movement of the bump. In addition, the pressure and density were extrapolated from the interior domain to the ghost nodes along the solid wall boundaries using a zero-order extrapolation.

6 Results and Discussion

The following sections discuss the results from this current work. First, the discussion will focus on the compressor face boundary condition results for the one-dimensional model. These results will be compared to the experimental data from the University of Cincinnati. Then, the discussion will investigate the performance of the boundary conditions for the axisymmetric numerical model of the experimental setup.

6.1 One-Dimensional Model

6.1.1 Model Validation

Freund and Sajben at the University of Cincinnati gathered experimental data on the static pressure distribution across the annular duct for an inlet Mach number of 0.16.[11] Table 1 lists the flow and compressor conditions for this experimental run. The listed ambient pressure p_{amb} and temperature T_{amb} were used for the total pressure and temperature conditions, respectively, at the inflow boundary for the numerical one-dimensional model. The reference pressure p_{ref} was measured at an axial location approximately 1.53 meters in front of the mean plane of the first stage rotor. The reference dynamic pressure q_{ref} was defined to be the total pressure minus the reference pressure.

p_{amb} (kPa)	98.78
T_{amb} (K)	300.2
N_{cor} (RPM)	18452
p_{ref} (kPa)	96.92
q_{ref} (kPa)	1.86

Table 1: Flow and Compressor Conditions for $M_0 = 0.16$ Experimental Run

Figure 20 shows a comparison of the static pressure distribution calculated by the one-dimensional numerical model and the distribution measured at the University of Cincinnati for this Mach 0.16 experimental test. For this figure, $x = 0.0$ represents the mid-plane of the first stage rotor. The flat plate turbulent displacement thickness model given in Equation (58) was responsible reducing the cross-sectional area along the inlet. This reduction in area caused the pressure drop across the inlet. In Figure 20, the pressure distribution calculated by this model agrees well with the experimentally measured static pressure distribution except at the location of the struts in the inlet. Struts were located at approximately -0.15, -1.25, and -1.7 meters. These struts were not modeled in the numerical code. As the results in the next sections will show, the exclusion of the struts did not affect the ability of this model to replicate the incident and reflected disturbances travelling through the inlet. In addition, the flat plate displacement thickness model overpredicted the displacement thickness and subsequently the decrease in pressure over the flexible bump curvature as shown in the figure. To account for this overprediction of displacement thickness and pressure decrease, the height of the bump was increased approximately 10% to more closely match the amplitude of the experimental incident expansion wave created from the deflation of the bump. Some separation right behind the bump which was not simulated in the numerical model is shown in Figure 20. This one-dimensional representation of the experimental setup at the University of Cincinnati provided a good model to test the new compressor face boundary conditions against the data for four different experimental runs.

6.1.2 Experimental Test Run 14A

First, the numerical one-dimensional model was tested against the experimental data from the University of Cincinnati run 14A.[11] Table 2 lists the flow and compressor conditions for this experimental test. For this run, a Courant-Friedrichs-Lewy (CFL) condition number of 0.7 was employed. Unless otherwise indicated, all numerical results presented for this test case were calculated using the higher order spatial

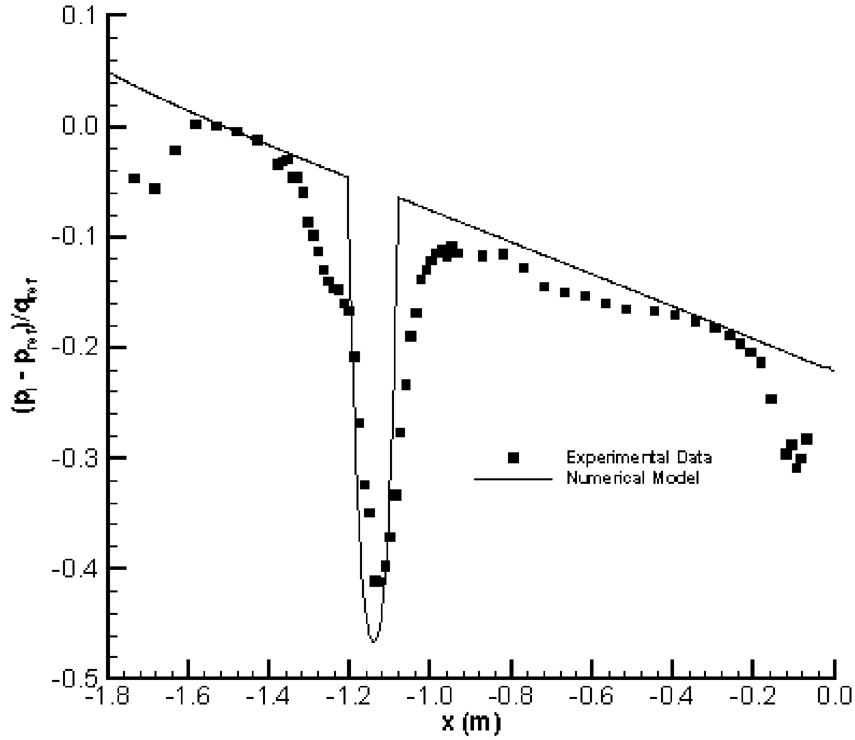

Figure 20: Axial Static Pressure Distribution in the Inlet for $M_0 = 0.16$

M_0	0.1637
M_{CF}	0.1867
p_{amb} (kPa)	98.74
T_{amb} (K)	295.7
$\dot{m}_{cor}$ (kg/m^3)	2.52
N_{cor} (RPM)	17912
Γ_{VIGV}	19.8°
Γ_{rotor}	52.0°
h_{bump} (m)	0.0121
T_{bump} (sec)	0.0008

Table 2: Flow and Compressor Conditions for Experimental Run 14A

discretiztion from limited MUSCL variable extrapolation and the four stage Runge-Kutta time integration scheme.

Figure 21 shows the steady state pressure and Mach number profiles for the inlet prior to the collapse of the bump. From a spectral analysis of their experimental data, Freund and Sajben concluded that the main reflection off the compressor occurred at the mid-plane of the first stage rotor.[11] Therefore, the domain extends to this location ($x = 2.0349$ m) for all steady state figures throughout the one-dimensional results section.

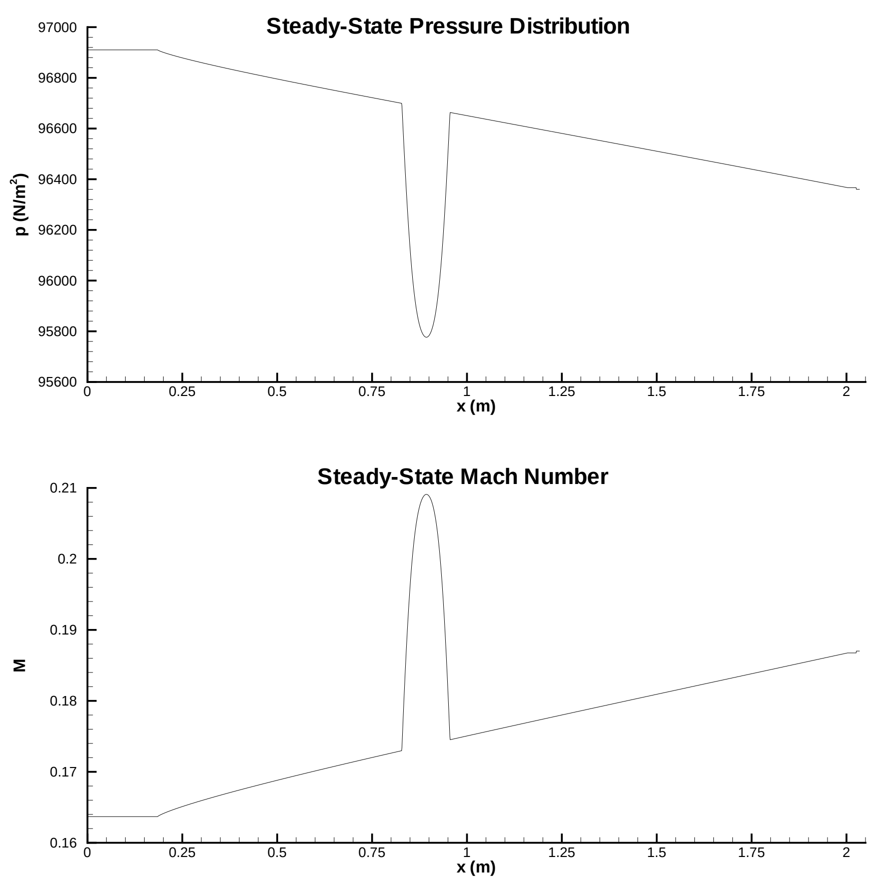

Figure 21: Steady State Pressure and Mach Number Distributions for Run 14A

Figure 22 shows the creation of the two expansion waves from the collapsing bump, the travel of the waves through the inlet, and the reflection of both waves off the inflow and outflow boundaries. The displacement of the flexible bump causes an extraction of energy from the flow and a creation of a local depression in pressure. After the bump completely collapses, this pressure depression splits into two acoustic expansion pulses which propagate in opposite directions through the inlet. After the downstream travelling disturbance interacts with the compressor, it is reflected back upstream as an expansion pulse with a smaller amplitude. For the numerical results of Figure 22, the new small disturbance compressor face boundary condition was employed. At the entrance to the inlet, the upstream acoustic wave is reflected as a compression wave since a constant total pressure condition was enforced at the inflow boundary.

The accuracy of the downstream travelling pulse in the numerical results is of primary importance to the study of compressor face boundary conditions. Figure 23 shows the time history of this incident expansion pulse as recorded by transducer station 1 ($x = 1.3427$ m). Both the first order spatial, Euler explicit method and higher order spatial, four stage Runge-Kutta method created incident pulses that agreed well with the experimental data for the incident wave at this station. Freund and Sajben stated that the observed oscillations behind the incident wave were due to rebounding of the flexible bump from the hub cage as it deflated.[11] They were unable to take any measurements of this effect. Therefore, the rebounding effect would be nearly impossible to numerically simulate and was neglected for this study. The amplitude of the experimental incident expansion pulse was -3576 Pa. The relative percent differences of the numerical amplitudes compared with the experimental amplitude were 2.29% and 1.35% for the first order and higher order numerical models, respectively.

The traditional outflow conditions of constant pressure, constant axial velocity,

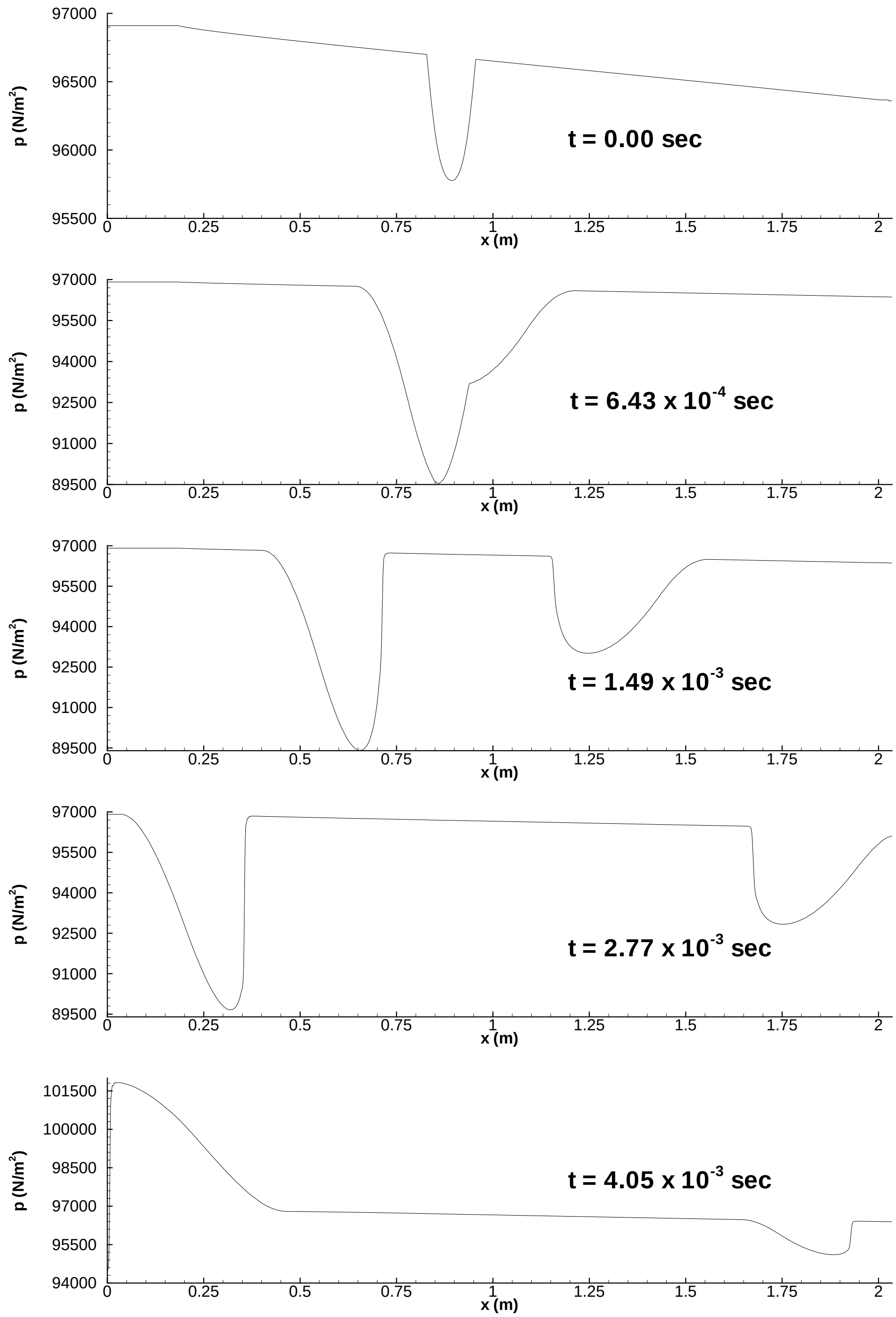

Figure 22: Expansion Wave Propagation Through the Inlet

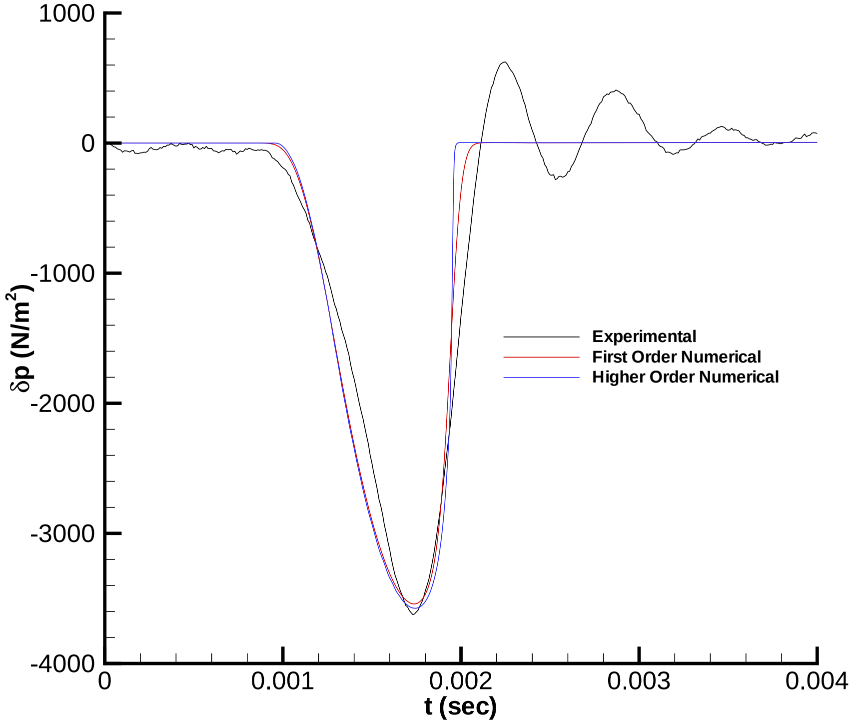

Figure 23: Incident Acoustic Expansion Pulse at Station 1 for Run 14A

and constant Mach number were applied at the compressor face boundary. The numerical reflection characteristics of these boundary conditions were compared with the experimental reflection results at transducer station 4 ($x = 1.9523$ m). Figure 24 shows differential pressure results at station 4 for the traditional boundary conditions and experiment for run 14A. At station 4, the incident and reflected waves overlap. In order to investigate the shape and amplitude of the reflected expansion pulse, the incident pulse measured at transducer 1 was shifted in time and subtracted from the pressure data collected at transducer 4. Figure 25 shows the reflected acoustic pulses produced by the traditional boundary conditions compared with the axial compressor data for this test case. The constant pressure boundary condition reflects a compression wave instead of an expansion wave. The constant axial velocity and constant

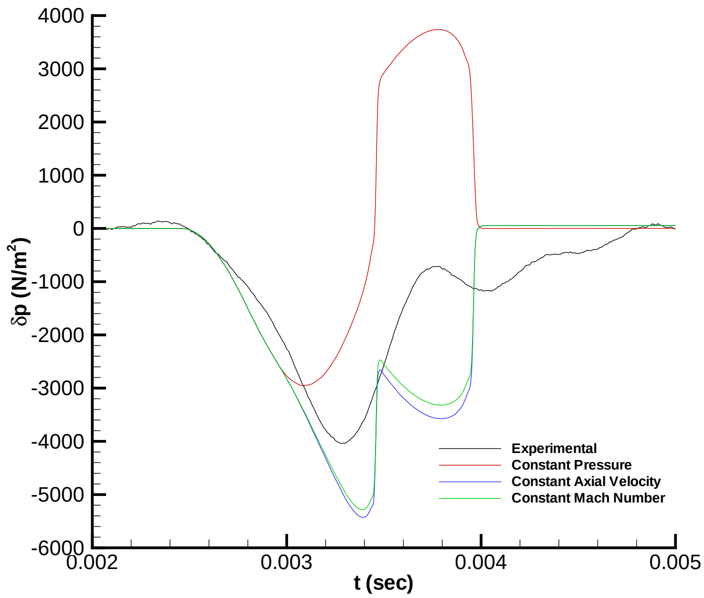

Figure 24: Comparison of Traditional Boundary Conditions vs. Experimental Data at Station 4 for Run 14A

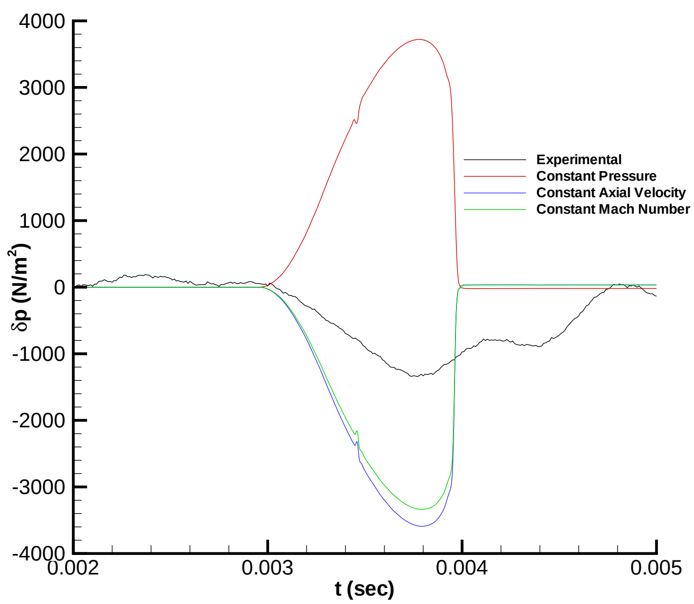

Figure 25: Traditional Boundary Conditions' Acoustic Wave Reflections for Run 14A

Mach number conditions predict an expansion reflection over twice the amplitude measured during the experiment. In agreement with previous work, this study also showed that traditional outflow boundary conditions do not properly represent an axial compressor's reflection characteristics.

Figures 26 and 27 show the reflection characteristics of the Paynter and Sajben small disturbance models at transducer station 4 for run 14A. The largest amplitude of the experimental reflection pulse was measured as -1335 Pa which corresponded to a 36.8% reflection of amplitude of the incident pulse off the axial compressor for this test run. The Sajben small disturbance model predicted a reflection disturbance that was less than half that measured by the University of Cincinnati. From Figure 27, the amplitude of the Paynter small disturbance reflection pulse is -1262 Pa which is a 5.47% relative difference from the experimental peak amplitude. In addition, the amplitude of this Paynter reflection was 35.3% of the numerical incident wave amplitude. Therefore, the Paynter small disturbance model provided better agreement with the initial and largest peak of the experimental reflection than the Sajben small disturbance model.

Due to the proprietary nature of the blade configuration for the axial compressor used at the University of Cincinnati, a few assumptions had to be made with regard to the input values required by the new small disturbance model. For Equation (26), the ratio of cross-sectional area in front of the rotor to the area behind was chosen to be 1.0 because a typical first stage rotor has little change in area across the blades. In addition, values for the inlet guide vanes and first stage rotor exit flow angles were needed. The known stagger angle for the variable inlet guide vanes was used for α_1 in Equation (47) since these vanes were uncambered blades. The known stagger angle for the first stage rotor blades was used for β_4 in Equation (47). The stagger angle for the rotor is larger than the exit blade angle. However, the exit angle of the flow

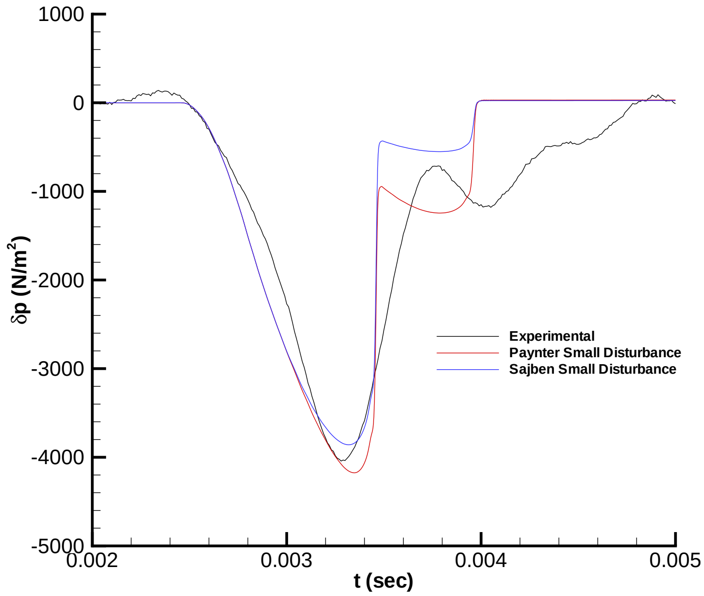

Figure 26: Comparison of Paynter and Sajben Small Disturbance Models vs. Experimental Data at Station 4 for Run 14A

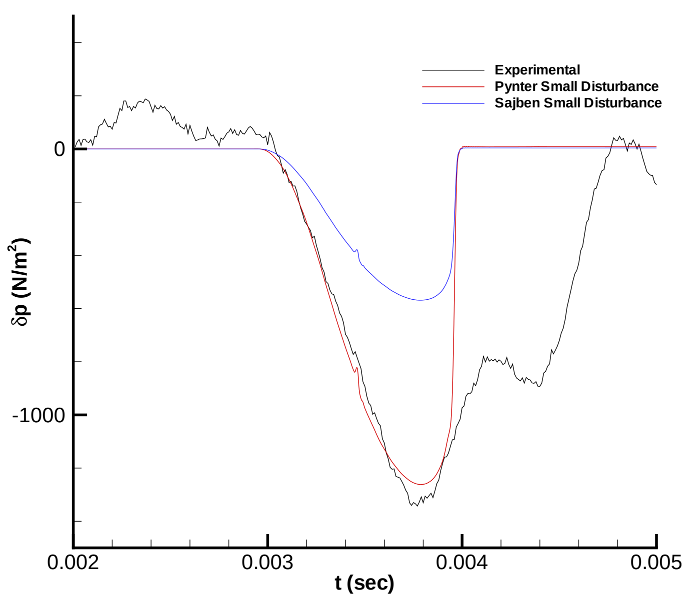

Figure 27: Paynter and Sajben Models' Acoustic Wave Reflections for Run 14A

is also larger than the exit blade angle. Therefore, this approximation of β_4 should be fairly accurate.

The numerical reflection results from the new small disturbance compressor face boundary condition model were compared with the experimental data from the University of Cincinnati run 14A and the numerical results from the Paynter small disturbance boundary condition. Figures 28 and 29 show these comparisons. In Figure 29, the amplitude of the reflected wave from the new small disturbance model shows excellent quantitative agreement with the amplitude of the largest peak in the experimental reflected wave. Although there are some differences in the waveform, the new small disturbance reflection also shows good qualitative agreement with the experimental reflection. Both the first and higher order model calculations of the reflected pulse from the new small disturbance compressor face boundary condition performed better than the Paynter small disturbance results when compared to the experimental data. The higher order model calculations produced a reflected wave of amplitude -1315 Pa which corresponded to a 1.50% relative difference from the experimental amplitude of -1335 Pa. The first order reflected wave had an amplitude of -1270 Pa. In addition, the amplitudes of the first and higher order reflections using the new small disturbance boundary condition were 35.9% and 36.8% of the numerical incident wave amplitudes, respectively. Therefore, the new small disturbance boundary condition models the reflection characteristics of the axial compressor more closely than Paynter's model for this experimental run.

The second reflection peak of the experimental wave in Figure 29 was concluded to be a reflection off the mid-plane of the second stage rotor by Freund and Sajben.[11] This second reflection plane was not modeled in the one-dimensional numerical code. However, a numerical run was conducted to test this conclusion. From analyzing published University of Cincinnati figures[11], the axial location of the mid-plane of

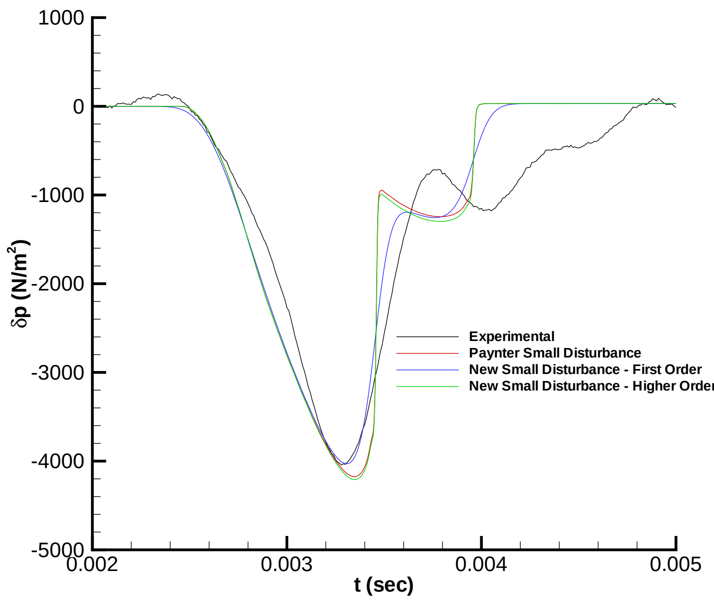

Figure 28: Comparison of New Small Disturbance Boundary Condition Model vs. Experimental Data at Station 4 for Run 14A

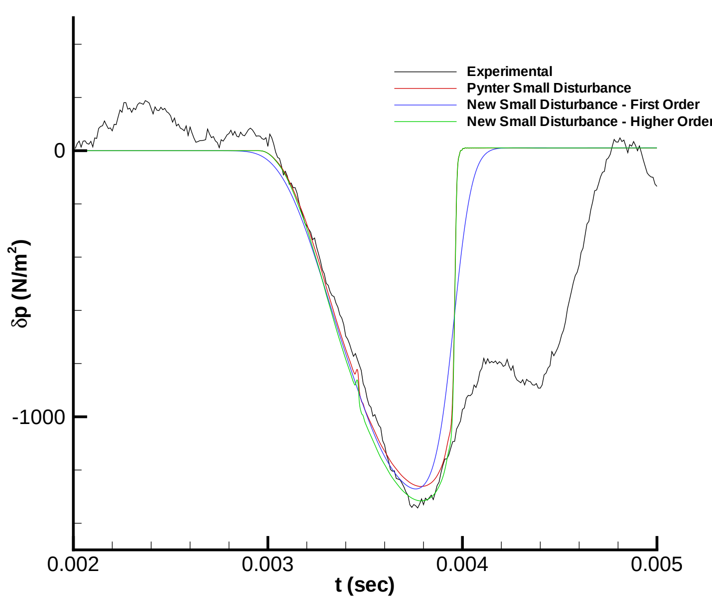

Figure 29: New Small Disturbance Model's Acoustic Wave Reflections for Run 14A

the second stage rotor was estimated to be $x = 2.072$ m. The numerical domain was extended to the second stage rotor, and a numerical run was conducted to investigate the reflection from this plane using the new small disturbance boundary condition. For this run, the same reflection response coefficient conditions used for the first stage rotor were employed for the second stage rotor since no data was available on the second stage. In addition, the presence of the first stage rotor was ignored so that the time history of the reflection from just the second stage rotor could be analyzed. Figure 30 shows the time history of the second stage reflection wave observed at transducer station 4. This figure also shows that the reflection from the second stage rotor mid-plane arrives at station 4 before the second peak in the experimental reflection. Therefore, this second peak in the experimental wave was reflected downstream of the second stage rotor. From the figure, this experimental reflection took place at approximately $x = 2.1314$ m. More information on the configuration of the axial compressor used in the experiment would be needed to better determine the location and cause of the second peak in the experimental reflected wave.

The effect of changing the new small disturbance boundary condition's area ratio across the rotor $\frac{S_1}{S_4}$ from 1.0 to 1.1 is shown in Figure 31. The fairly large 10% reduction in cross-sectional area produced a 19.3% increase in the amplitude of the reflection pulse. As stated previously, the cross-sectional area typically changes very little across the first stage rotor. Based on the limited information available, the assumption that the area remains constant across the rotor will be used for all remaining numerical runs.

The effect of changing the exit flow angle β_4 for the first stage rotor is shown in Figure 32. This 5° change in the flow angle produced an 18.1% decrease in the amplitude of the reflected pulse. However, the stagger angle of the rotor blades is a close approximation to the flow exit angle since both of these angles are greater than

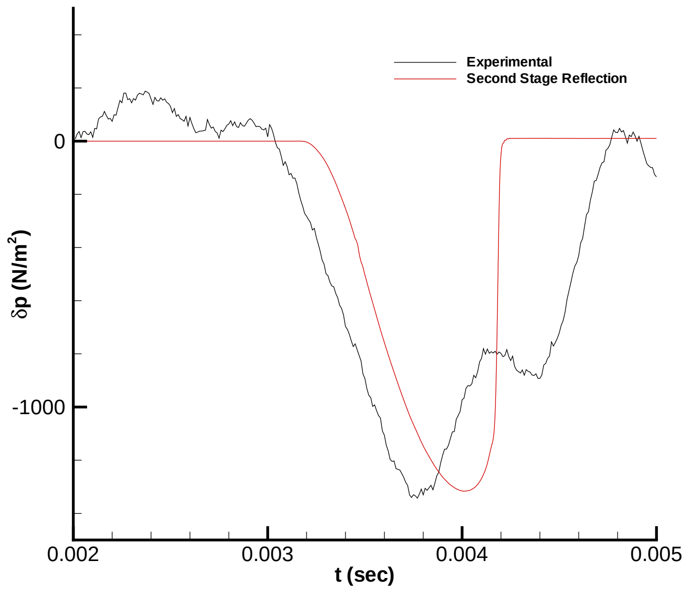

Figure 30: Acoustic Wave Reflection from Second Stage Rotor for Run 14A

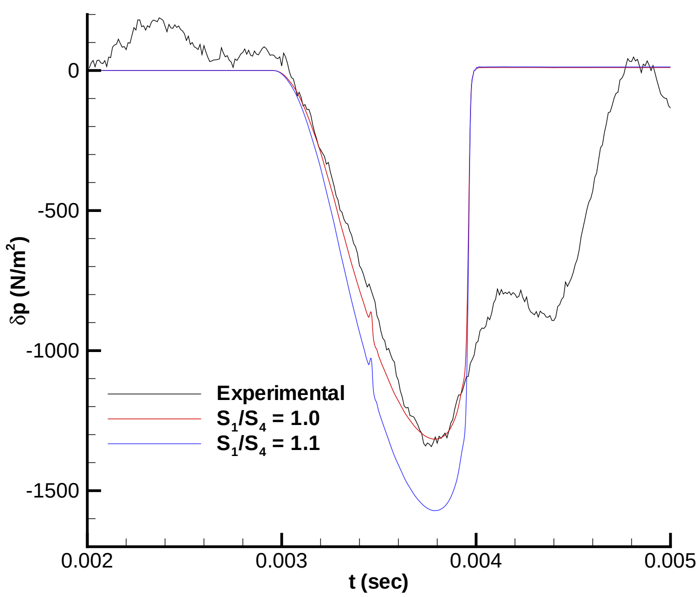

Figure 31: Acoustic Wave Reflections for Multiple Area Ratios

the blade exit angle. The assumption that the exit flow angle is approximately equal to the stagger angle will be used for all remaining numerical runs.

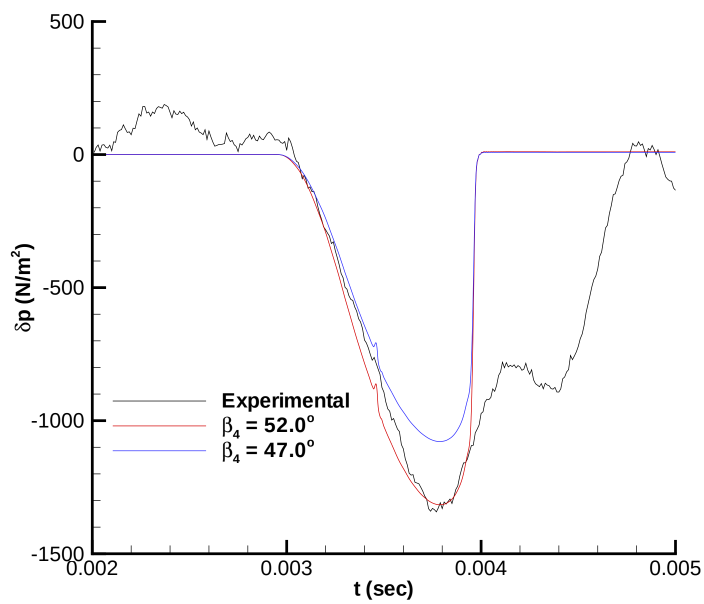

Figure 32: Acoustic Wave Reflections for Multiple Rotor Flow Angles

Figures 33 and 34 show the reflection characteristics of the simple area reduction boundary condition. The area reduction boundary condition for the higher order numerical model produced a reflected expansion wave with an amplitude of -1410 Pa. The first order reflection pulse had an amplitude of -1362 Pa. Although the area reduction model overestimated the reflection characteristics of the axial compressor for run 14A, this simple model still calculated the reflection amplitude within an accuracy of 5.5%. The numerical reflection results of run 14A showed that both the new small disturbance model and area reduction model compressor face boundary conditions provided improved wave amplitude accuracy over existing boundary conditions when compared with the experimental data.

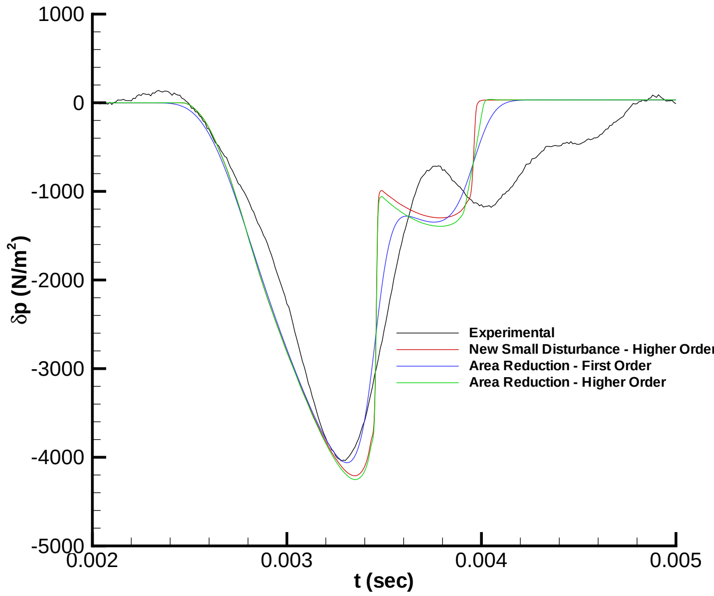

Figure 33: Comparison of Area Reduction Boundary Condition Model vs. Experimental Data at Station 4 for Run 14A

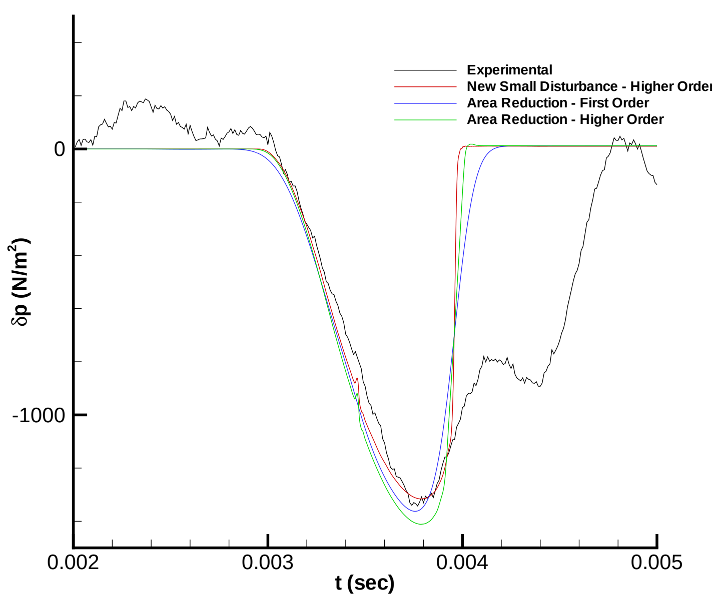

Figure 34: Area Reduction Model's Acoustic Wave Reflections for Run 14A

6.1.3 Experimental Test Run 010A

Second, the numerical one-dimensional model was tested against the experimental data from the University of Cincinnati run 010A.[11] Table 3 lists the flow and compressor conditions for this experimental test. A CFL of 0.7 was also used for these numerical runs. Again, all numerical results were higher order calculations unless otherwise stated. Figure 35 shows the inlet steady state pressure and Mach number profiles for run 010A.

M_0	0.1637
M_{CF}	0.1869
p_{amb} (kPa)	100.22
T_{amb} (K)	294.8
$\dot{m}_{cor}$ (kg/m^3)	2.52
N_{cor} (RPM)	18088
Γ_{VIGV}	24.8°
Γ_{rotor}	52.0°
h_{bump} (m)	0.0116
T_{bump} (sec)	0.0008

Table 3: Flow and Compressor Conditions for Experimental Run 010A

Figure 36 shows the time history of the incident expansion pulse as recorded by transducer station 1 for run 010A. The amplitude of the experimental expansion pulse was -3485 Pa. Solution of the limited minmod variable extrapolation Roe flux model with a four stage Runge-Kutta scheme provided an incident expansion wave which had an amplitude of -3484 Pa. Therefore, the higher order model almost matched the wave amplitude exactly. The differences in the wave shapes between experimental and numerical were due to the bump collapse mechanism model. The one-dimensional numerical model accurately predicted the acoustic expansion disturbance which travels downstream and interacts with the compressor face boundary condition.

Figure 37 shows the reflected acoustic pulses calculated by the Paynter and new

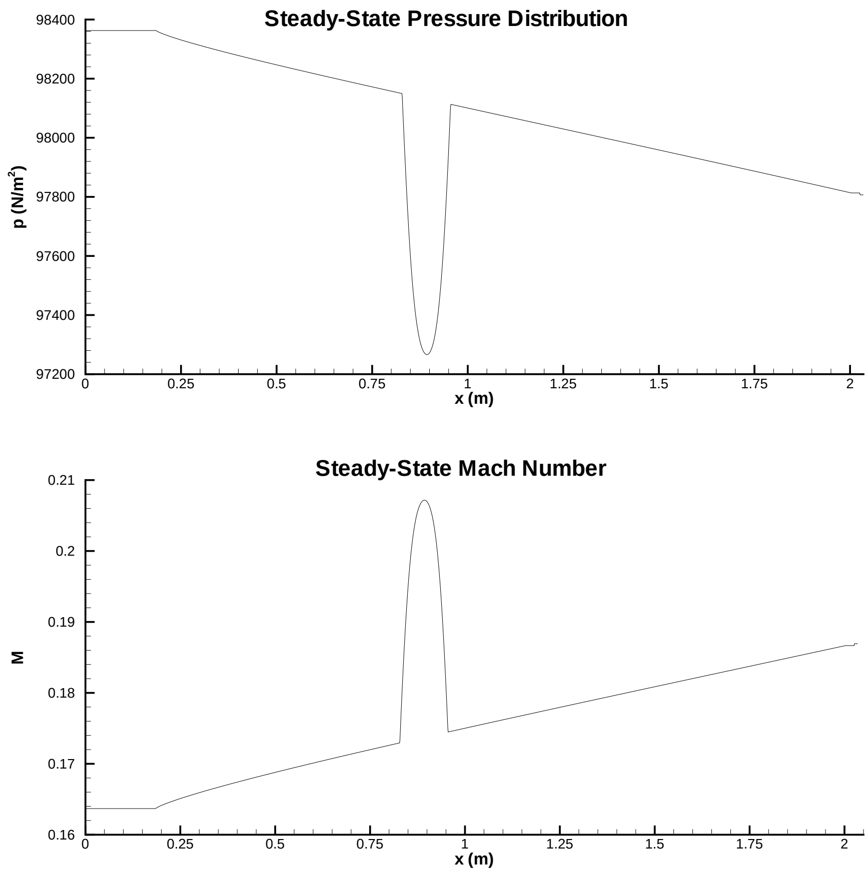

Figure 35: Steady State Pressure and Mach Number Distributions for Run 010A

small disturbance boundary conditions and measured by the pressure transducer at station 4 for run 010A. The largest amplitude of the experimental reflection pulse was measured as -1375 Pa which corresponded to a 39.5% reflection of the incident pulse amplitude by the axial compressor. The amplitude of the Paynter model reflection pulse was -1229 Pa which was a 10.6% relative difference from the experimental amplitude. In addition, the Paynter small disturbance model reflected only 35.3% of the amplitude of the numerical incident wave from the compressor face boundary. Both the first and higher order new boundary condition model calculations of the reflected pulse provided better agreement with the experimental data than the Paynter model

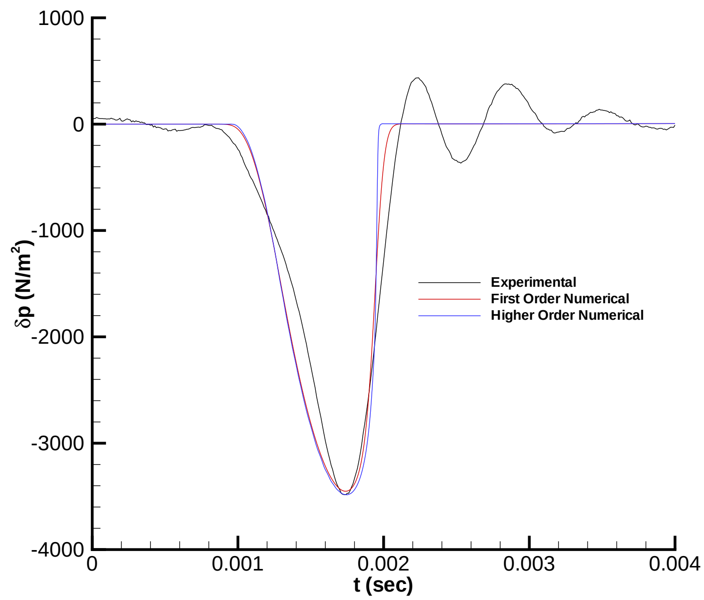

Figure 36: Incident Acoustic Expansion Pulse at Station 1 for Run 010A

results as shown in Figure 37. The higher order new small disturbance boundary condition reflected an expansion wave of amplitude -1355 Pa which corresponded to a 1.45% relative difference from the experimental amplitude. The first order reflected wave had an amplitude of -1311 Pa. The first and higher order models using the new small disturbance boundary condition reflected 37.9% and 38.9% of the amplitude of the numerical incident waves, respectively. Therefore, the new small disturbance boundary condition model again predicted the reflection characteristics of the axial compressor more closely than the Paynter small disturbance model.

Figure 38 shows the acoustic expansion waves created by the reflection of the incident expansion pulse off the simple area reduction boundary condition. The area reduction boundary condition for the higher order numerical model produced a reflected expansion wave with an amplitude of -1288 Pa which corresponded to a 6.33% relative difference from the experimental amplitude. The first order reflection pulse

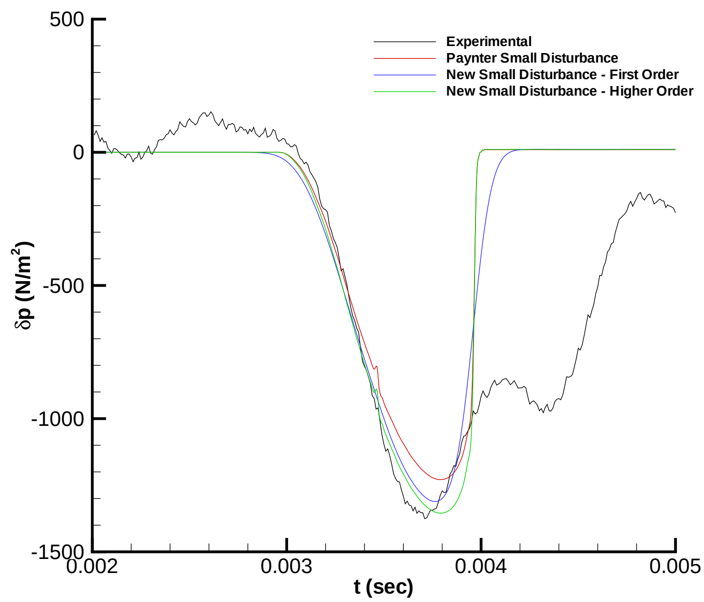

Figure 37: Paynter and New Small Disturbance Models' Acoustic Wave Reflections for Run 010A

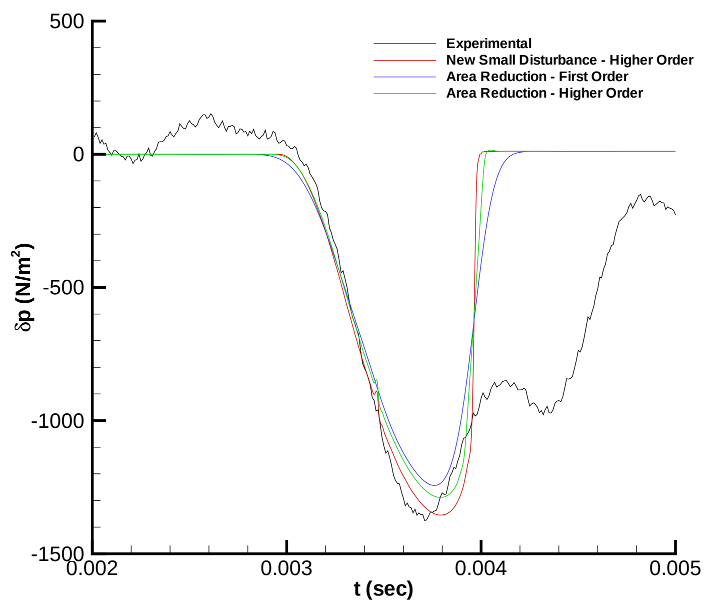

Figure 38: Area Reduction Model's Acoustic Wave Reflections for Run 010A

had an amplitude of -1243 Pa. Although the area reduction model did not perform better than the new small disturbance boundary condition, this simple boundary condition did predict the amplitude of the reflection pulse more accurately than the Paynter small disturbance boundary condition. The numerical reflection results of run 010A also showed that both the new small disturbance model and area reduction model compressor face boundary conditions provided improved wave amplitude accuracy over existing boundary conditions when compared with the experimental data.

6.1.4 Experimental Test Run 41A

Third, the numerical one-dimensional model was tested against the experimental data from the University of Cincinnati run 41A.[11] Table 4 lists the flow and compressor conditions for this experimental test. Again, a CFL of 0.7 was used for these numerical runs, and all numerical results given below were higher order calculations unless otherwise stated. Figure 39 shows the inlet steady state pressure and Mach number profiles for run 41A.

M_0	0.1724
M_{CF}	0.1968
p_{amb} (kPa)	98.93
T_{amb} (K)	295.6
$\dot{m}_{cor}$ (kg/m^3)	2.65
N_{cor} (RPM)	18749
Γ_{VIGV}	24.8°
Γ_{rotor}	52.0°
h_{bump} (m)	0.0126
T_{bump} (sec)	0.0008

Table 4: Flow and Compressor Conditions for Experimental Run 41A

Figure 40 shows the time history of the incident expansion pulse as recorded by transducer station 1 for run 41A. The amplitude of the experimental expansion pulse

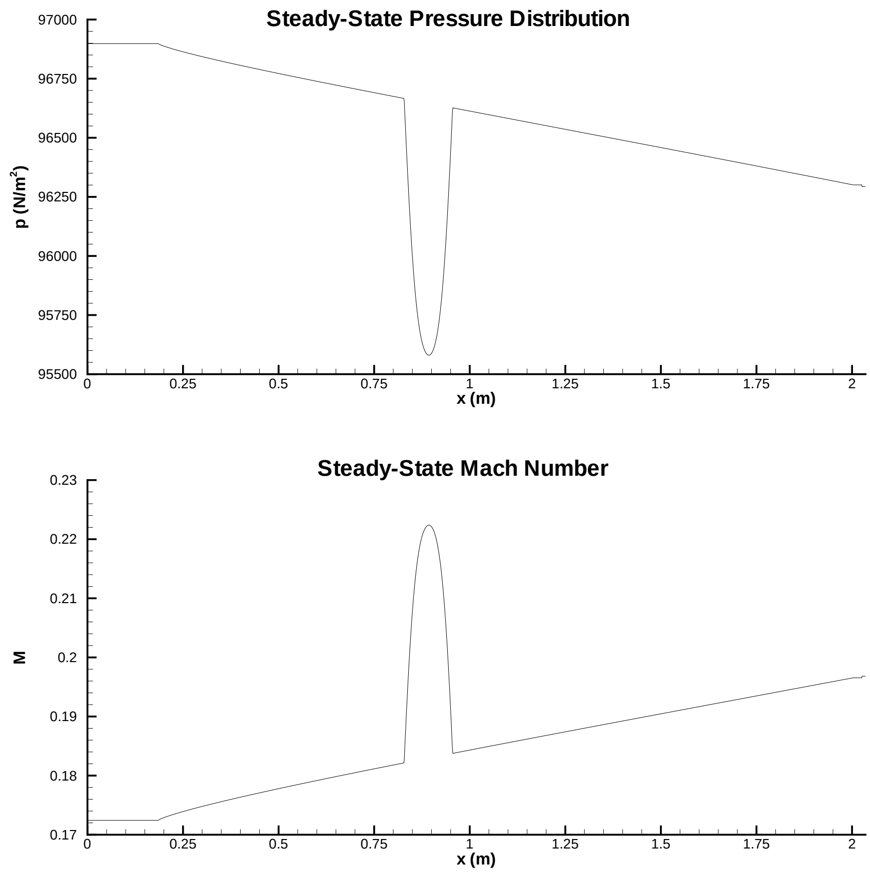

Figure 39: Steady State Pressure and Mach Number Distributions for Run 41A

was -3719 Pa. The collapsing bump simulated by the higher order numerical model created an expansion disturbance to the flow with an amplitude of -3654 Pa. This numerical expansion wave had a 1.75% difference in amplitude from the experimental pulse. Again, the one-dimensional numerical model accurately predicted the incident acoustic expansion disturbance. This is very important since this wave is reflected by the compressor face boundary conditions.

Figure 41 shows the time history of the reflected acoustic pulses calculated by the Paynter and new small disturbance boundary conditions at transducer station 4 for run 41A. The largest amplitude of the experimental reflection pulse was measured as

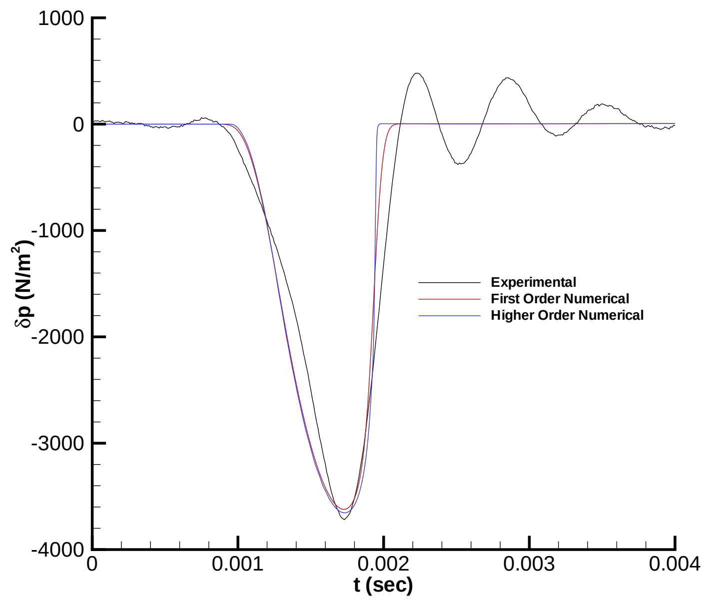

Figure 40: Incident Acoustic Expansion Pulse at Station 1 for Run 41A

-1342 Pa which corresponded to a 36.1% reflection of the incident pulse off the axial compressor for this test run. The Paynter small disturbance boundary condition produced a reflected expansion pulse with an amplitude of -1315 Pa which corresponded to a 2.01% relative difference from the experimental amplitude. In addition, the amplitude of this numerical reflected pulse was 35.9% of the amplitude of the numerical incident wave. The higher order new small disturbance boundary condition reflected an expansion wave of amplitude -1348 Pa which corresponded to a 0.45% relative difference from the experimental amplitude. The amplitude of this reflection by the new small disturbance model was 36.9% of the amplitude of the numerical incident wave. Again, the new small disturbance boundary condition provided an accurate reflection for the compressor face boundary.

Figure 42 shows the time history of the reflected expansion pulses created by the simple area reduction boundary condition at station 4 for run 41A. The area reduc-

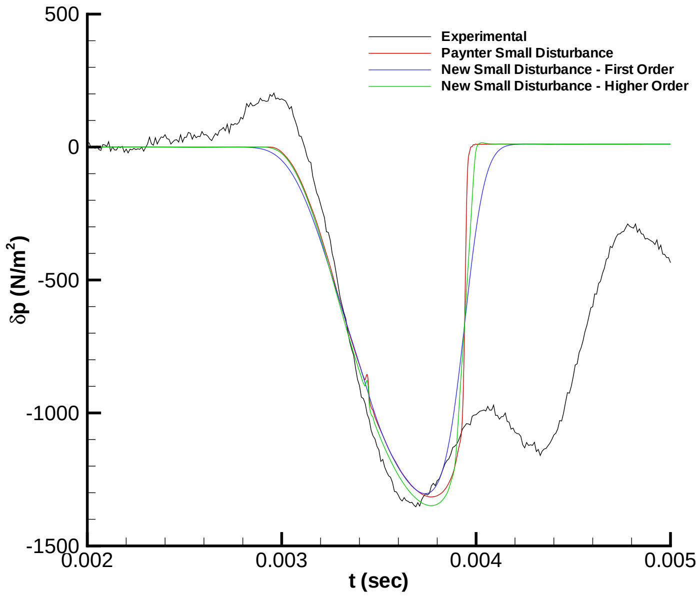

Figure 41: Paynter and New Small Disturbance Models' Acoustic Wave Reflections for Run 41A

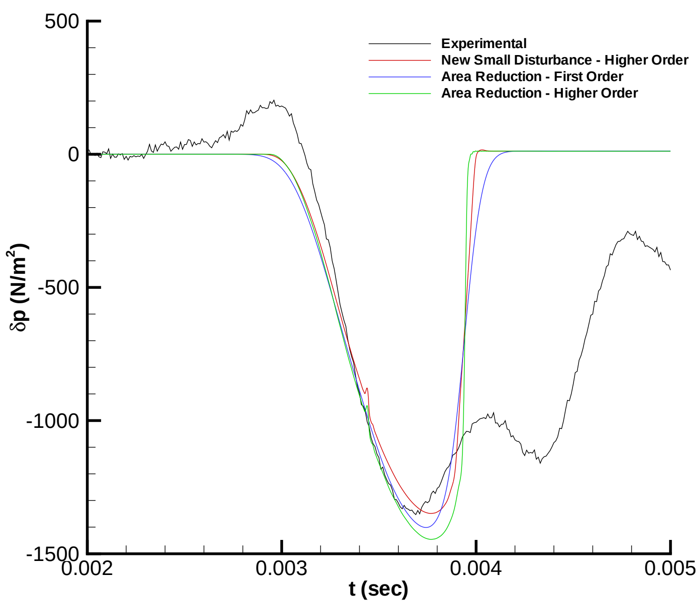

Figure 42: Area Reduction Model's Acoustic Wave Reflections for Run 41A

tion boundary condition for the higher order numerical model produced a reflected expansion wave with an amplitude of -1445 Pa while the first order reflection pulse had an amplitude of -1401 Pa. Although the area reduction model overpredicted the reflection amplitude, this boundary condition still calculated the reflection pulse amplitude within 8% of the experimental value. The numerical reflection results of run 41A showed the same trends as the previous two experimental runs.

6.1.5 Experimental Test Run 40A

Finally, the numerical one-dimensional model was tested against the experimental data from the University of Cincinnati run 40A.[11] Table 5 lists the flow and compressor conditions for this experimental test. Like the previous runs, a CFL number of 0.7 was used. All numerical results for this run were higher order calculations unless otherwise stated. Figure 43 shows the steady state pressure and Mach number distributions for the experimental run 40A.

M_0	0.1751
M_{CF}	0.1999
p_{amb} (kPa)	98.19
T_{amb} (K)	292.6
$\dot{m}_{cor}$ (kg/m^3)	2.69
N_{cor} (RPM)	18316
Γ_{VIGV}	19.8°
Γ_{rotor}	52.0°
h_{bump} (m)	0.0121
T_{bump} (sec)	0.0008

Table 5: Flow and Compressor Conditions for Experimental Run 40A

Figure 44 shows the time history of the incident expansion pulse as recorded by transducer station 1 for run 40A. The experimental expansion pulse had an amplitude of -3515 Pa. The incident disturbance created by the higher order numerical model had an amplitude of -3481 Pa which corresponded to a 0.97% difference in amplitude

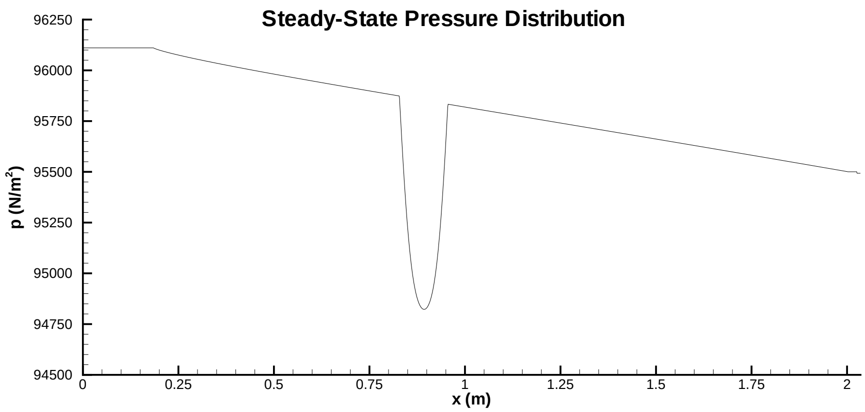

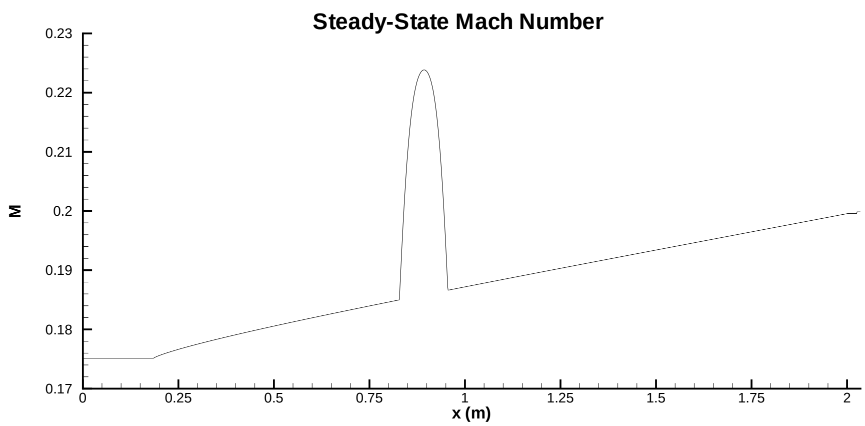

Figure 43: Steady State Pressure and Mach Number Distributions for Run 40A

from the experimental pulse. The first order incident expansion wave had an amplitude of -3448 Pa. Like the previous three cases, the higher order model for run 40A predicted the amplitude of the incident pulse more accurately than the first order model as expected. The one-dimensional modeling of the bump collapse produced incident waves that agreed well with the experimentally measured waves for all four cases.

Figures 45 and 46 show the time history of the reflected acoustic pulses calculated by the Paynter small disturbance, new small disturbance, and area reduction boundary conditions at transducer station 4 for run 40A. All of these numerical boundary

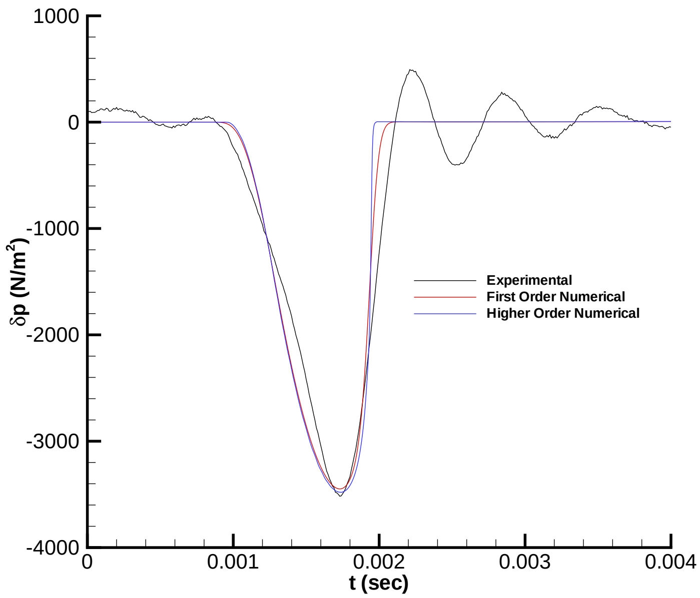

Figure 44: Incident Acoustic Expansion Pulse at Station 1 for Run 40A

condition models overpredicted the amplitude of the reflected expansion pulse. The amplitude of the experimental reflection pulse was measured as -1114 Pa which corresponded to a 31.7% reflection of the incident pulse by the axial compressor for run 40A. This 31.7% reflection for the experimental case was much lower than the typical experimental reflection values of approximately 36% observed by Freund and Sajben. A problem with the data reduction for this experimental run could have occurred. The reflected expansion pulses produced by the Paynter and new small disturbance boundary conditions had amplitudes that differed from the experimental amplitude by 13% and 18%, respectively. In addition, the area reduction boundary condition also produced an expansion pulse that differed from the experimental pulse by 18%. With the exception of this run, the new small disturbance and area reduction boundary conditions provided wave reflections that accurately modeled the amplitude of the reflected wave from the axial compressor within 3% and 8%, respectively.

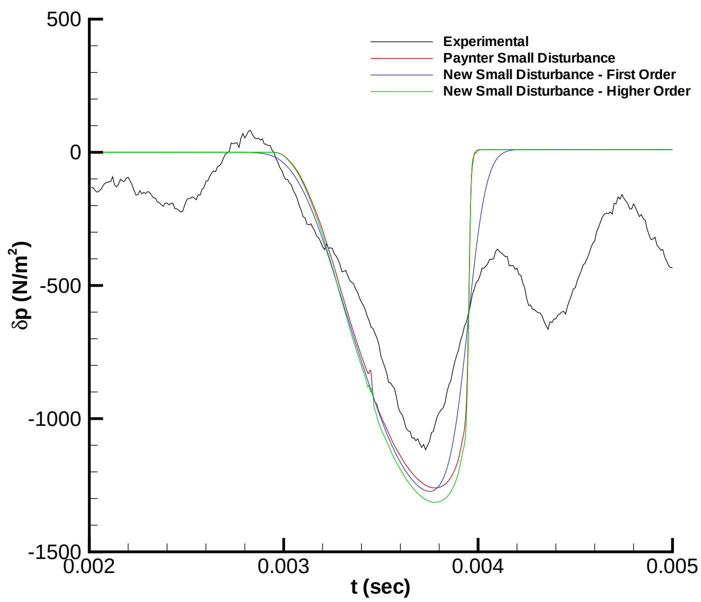

Figure 45: Paynter and New Small Disturbance Models' Acoustic Wave Reflections for Run 40A

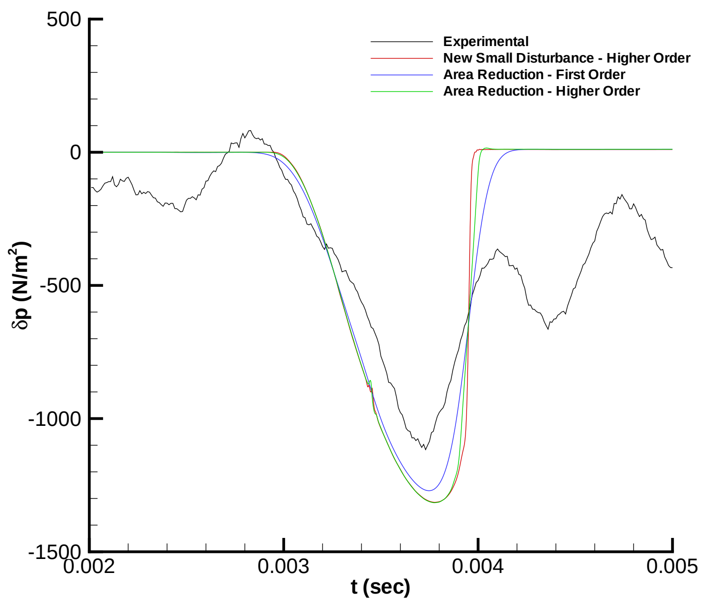

Figure 46: Area Reduction Model's Acoustic Wave Reflections for Run 40A

6.2 Axisymmetric Model

6.2.1 Model Validation

Freund and Sajben measured a steady state pressure distribution along the annular duct and velocity profiles both upstream and downstream of the flexible bump for the experimental conditions given in Table 1.[11] Figure 47 shows the comparison of the axisymmetric numerical pressure distributions across the inlet to the experimentally measured distribution. For all three sets of data, the pressure was measured along the case of the annular duct. The first order model used an Euler explicit time integration with a first order spatial discretization, and the higher order model used a two stage Runge-Kutta time integration scheme with a minmod limited MUSCL variable extrapolation for higher order spatial discretization. Again, the struts located at approximately -0.15, -1.25, and -1.7 meters were not modeled in the numerical code. The higher order model showed good agreement in the calculation of the pressure distribution along the bump when compared with the experimental data. However, both numerical models showed a larger pressure drop across the bump than measured experimentally. Freund and Sajben noticed that the measured pressure did not fully recover downstream of the bump, but they did not invesitgate the causes of this pressure drop.[11] From analyzing the experimental data, the pressure drop across the bump should be approximately 70 Pa if the pressure fully recovers. This pressure drop is due to the boundary layer growth along the bump portion of the inlet. The University of Cincinnati experimental data showed an additional approximately 45 Pa pressure drop across the bump for a total pressure drop of 115 Pa. The first order model calculated a very large pressure drop of approximately 310 Pa across the bump, and the higher order model calculated this pressure drop to be approximately 160 Pa. Therefore, the higher order pressure distribution had a pressure drop that was approximately 45 Pa larger than the experimental drop. The cause of this larger

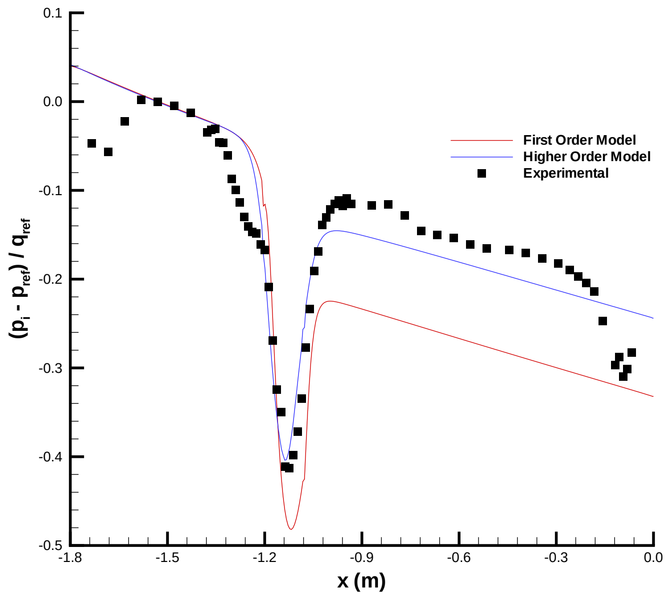

Figure 47: Axial Static Pressure Distribution Comparison Along Inlet Case

pressure drop maybe due to the high pressure regions calculated by the axisymmetric numerical model at the leading and trailing edges of the bump as shown in Figure 48. These non-physical regions are due to excess diffusion (dissipation and dispersion)[31] produced by the numerical method at low flow speeds. To reduce this excess numerical diffusion, a preconditioned numerical model would need to be employed. However, a preconditioned model would not allow for time accurate tracking of the acoustic pulses generated by the collapse of the flexible bump. Since the purpose of this research was to accurately model the reflection characteristics of the axial compressor in time, the higher order non-preconditioned model presented in Section 5 was used for the axisymmetric results. In addition, the pressure distribution along the hub/bump wall had an oscillatory effect at the leading and trailing edges of the bump. Possible causes for these oscillations are numerical dispersion from the higher order model and the thin layer approximation to the viscous flux terms. The effects of the larger numerical pressure drop across the bump and the oscillations in the flow on the unsteady results will be shown later in this results section.

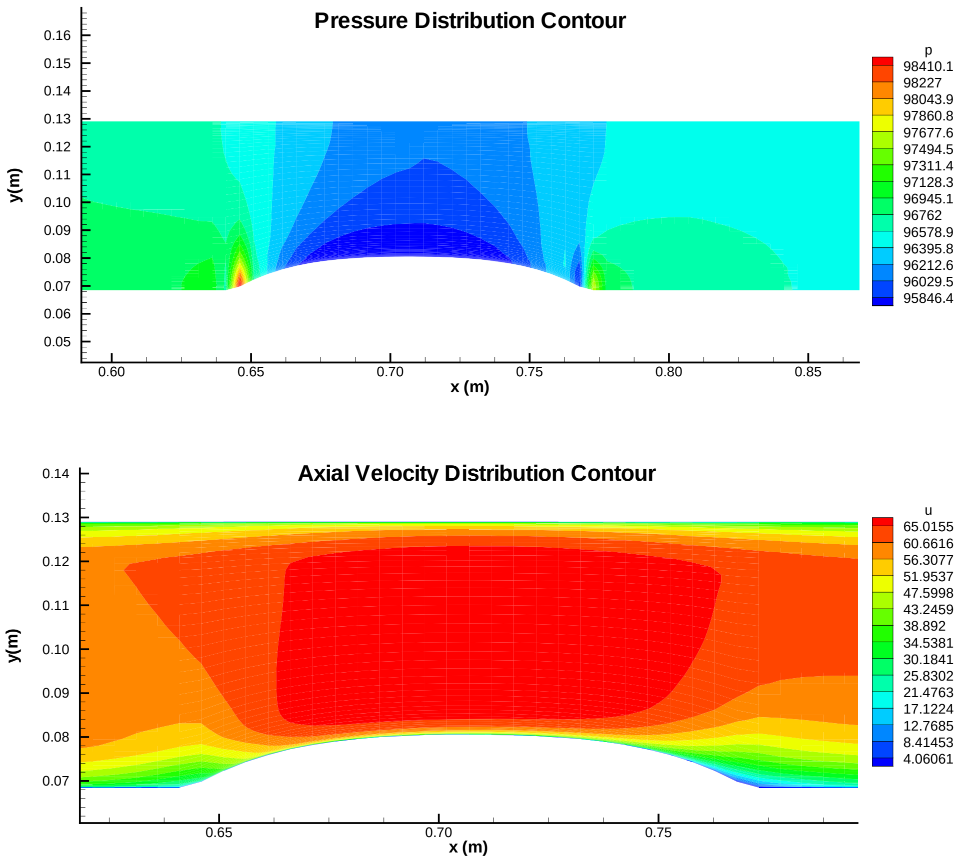

Figure 48: Numerical Pressure and Axial Velocity Contour Plots over the Flexible Bump for the Validation Case

The velocity profiles for this experimental steady state test case were measured at x = -0.2218 and -1.5585 meters.[11] Figure 49 shows the agreement of the numerical velocity profiles with the measured experimental profile upstream of the flexible bump. The first and higher order numerical profiles overlap at this location. The numerical model calculated the boundary layerto be slightly thicker on the hub and too thin on the case when compared to the experimental data. However, the velocity profiles do agree reasonably well with the experimental results. Figure 50 shows the experimentally measured and numerically calculated profiles downstream of the bump. Both numerical models calculated thicker boundary layer at the hub and a thinner boundary layer at the case than experiment for this location. The higher order velocity profile is approaching a fully developed profile for the annular duct. The experimental velocity profile shows very little growth in the hub boundary layer along the inlet. In addition, the experimental boundary layer on the case occupies approximately 60% of the total annulus height. The boundary condition at the compressor face for the steady state numerical calculations was constant static pressure. There may be some factor at the axial compressor that is not being taken into consideration by the model boundary conditions that contributes to this experimental velocity profile. However, no mention of any additional factors was given by Freund and Sajben other than possible blockage by the struts. Therefore, the axisymmetric model boundary conditions were not changed.

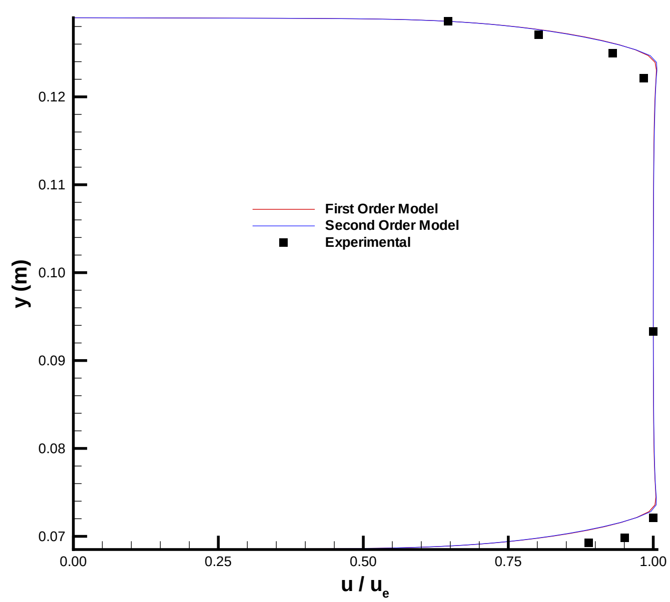

Figure 49: Velocity Profiles at x = -1.5585 m for the Validation Case

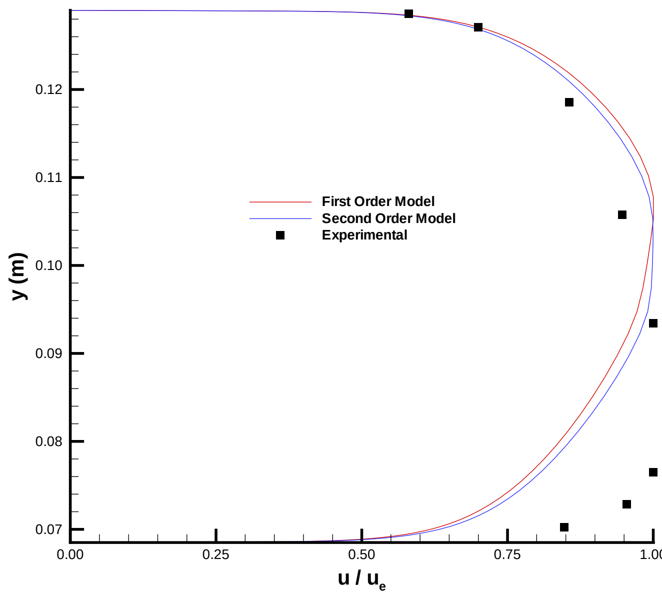

Figure 50: Velocity Profiles at x = -0.2218 m for the Validation Case

The effectiveness of the Spalart-Allmaras turbulence model was evaluated. Figure 51 shows a comparison of the turbulence model to the Law of the Wall at locations both upstream and downstream of the flexible bump. At the upstream location, the turbulent boundary was still developing. The numerical velocity profiles at both locations show good agreement with the Law of the Wall. In addition, the cell center of the first cell off the hub or case had a y^+ value of approximately 1.5. Therefore, the physical grid was partitioned correctly for turbulence calculations, and the turbulence model performed properly for the axisymmetric numerical code.

The compressor face boundary reflection results from axisymmetric turbulent flow model were compared to the experimental data gathered for four test cases. The results presented in the following sections were calculated using the higher order axisymmetric model.

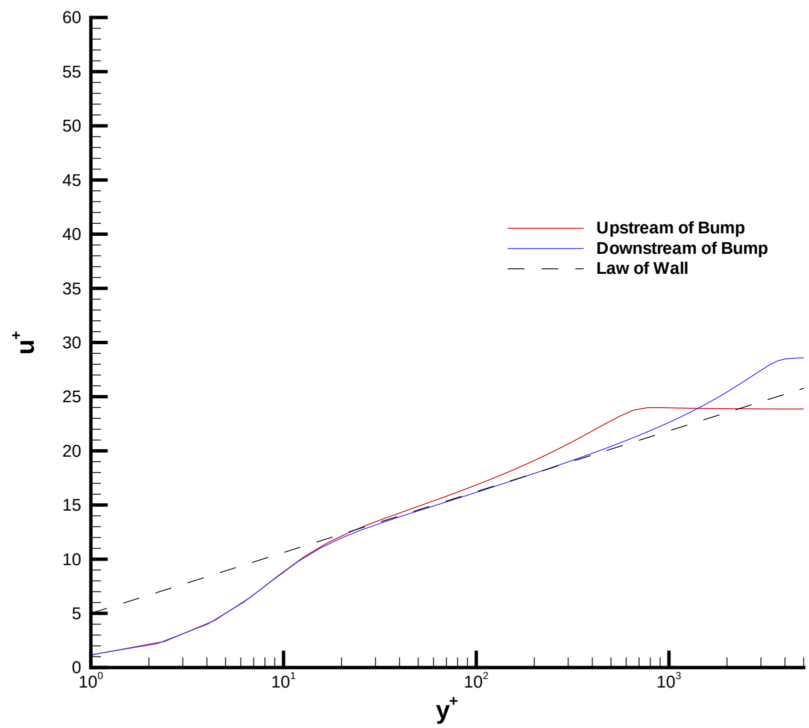

Figure 51: Profile of Turbulent Boundary Layer at $x =$ -0.2218 and -1.5585 m

6.2.2 Experimental Test Run 14A

First, the results from the axisymmetric model were compared to the experimental data from run 14A. Table 2 lists the flow and compressor conditions for this experimental test. The rotor stagger angle listed in the table is the angle at the mean radius. For all axisymmetric model numerical runs, the stagger angle for the first stage rotor varies linearly from 45° at the hub to 60° at the case. Like the one-dimensional model, assumptions had to be made with regard to the input values required by the new small disturbance boundary condition for the axisymmetric model. Again, the ratio of cross-sectional area in front of the rotor to the area behind was chosen to be 1.0, the known stagger angle for the variable inlet guide vanes was used for α_1, and the known variation of the stagger angle for the first stage rotor blades was used for β_4. These same assumptions were used for all numerical runs presented in the axisymmetric results section.

Figures 52 and 53 show contour plots and pressure profiles of the acoustic wave motion through the inlet, respectively. The collapse of the flexible bump creates two expansion pulses, one propagating upstream and the other downstream toward the compressor face. Then, both waves are reflected off the inflow and outflow boundaries. Both figures show the oscillatory nature of the flow field between the two expansion pulses at $t = 1.45$ and 2.38 milliseconds. The steady state pressure profile in Figure 53 has a 170 Pa pressure drop across the bump. The normal pressure drop due to the growth of the boundary layer along the bump should be approximately 80 Pa. The additional 90 Pa pressure drop could be responsible for some of the oscillatory behavior in the flow field since the flow needs to adjust itself so that its pressure profile is continuous across the domain. However, a detailed look at the flow field around the bump after it had collapsed showed that a compression wave was formed along the hub from the downward movement of the fluid as the bump collapsed. This compression wave merged with the high pressure region at the trailing edge of the bump and propagated across the annulus. When the compression wave reached the case, it reflected off the case and spread out. This compression wave then propagated back across the annulus, reflected off the hub, and spread out. As the compression wave spread out, it produced oscillations in the flow that propagated both upstream and downstream through the duct. The pressure profiles at $y = 0.099$ m in Figure 53 show that the oscillations were being damped out over time. These oscillations do interact with the reflected wave from the compressor face boundary condition. The reflected wave at $t = 3.99$ milliseconds in both figures was created by the new small disturbance boundary condition. In Figure 52, the incident expansion waves travelling in both

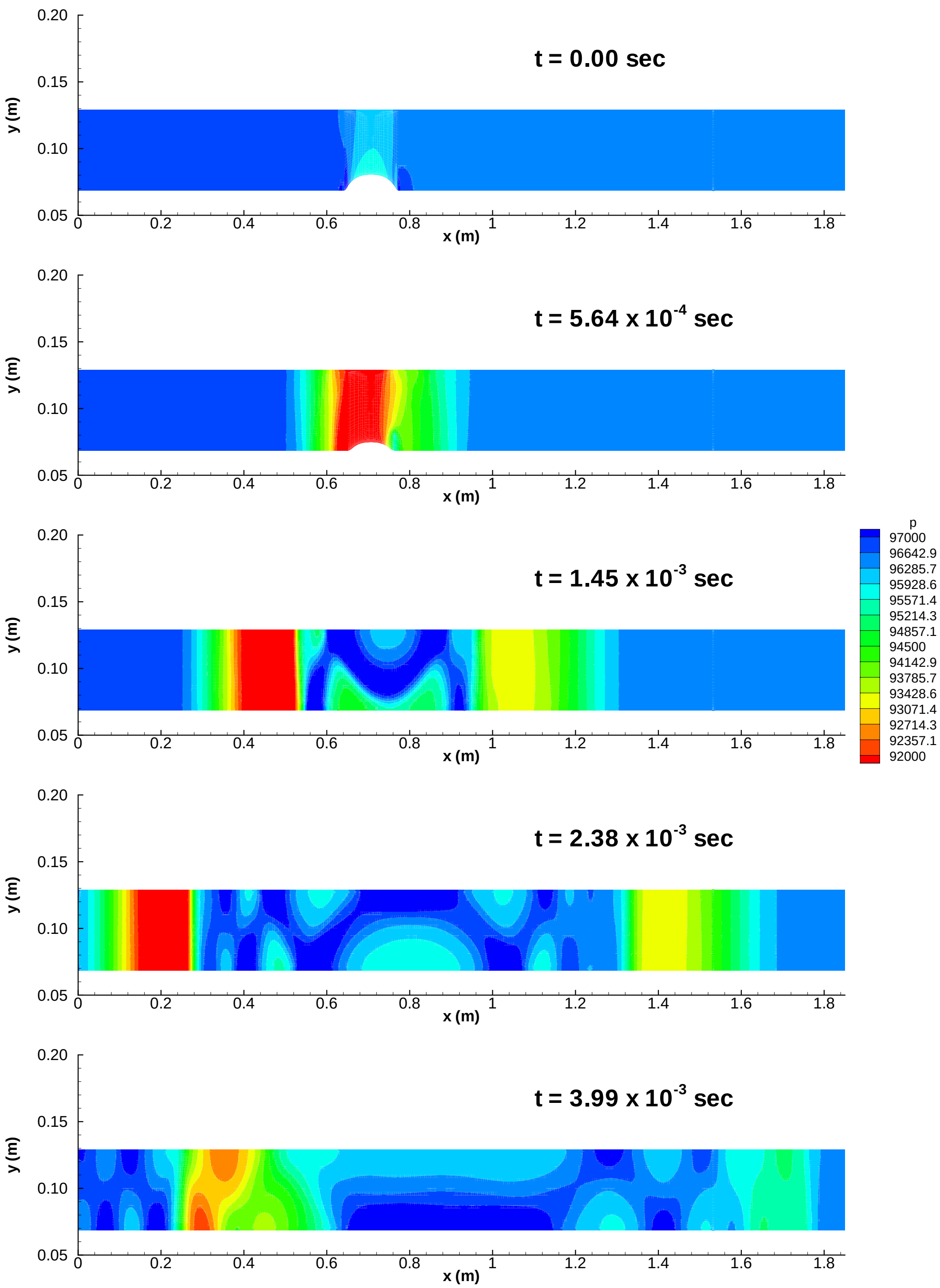

Figure 52: Contour Plots of Wave Propagation Through the Inlet

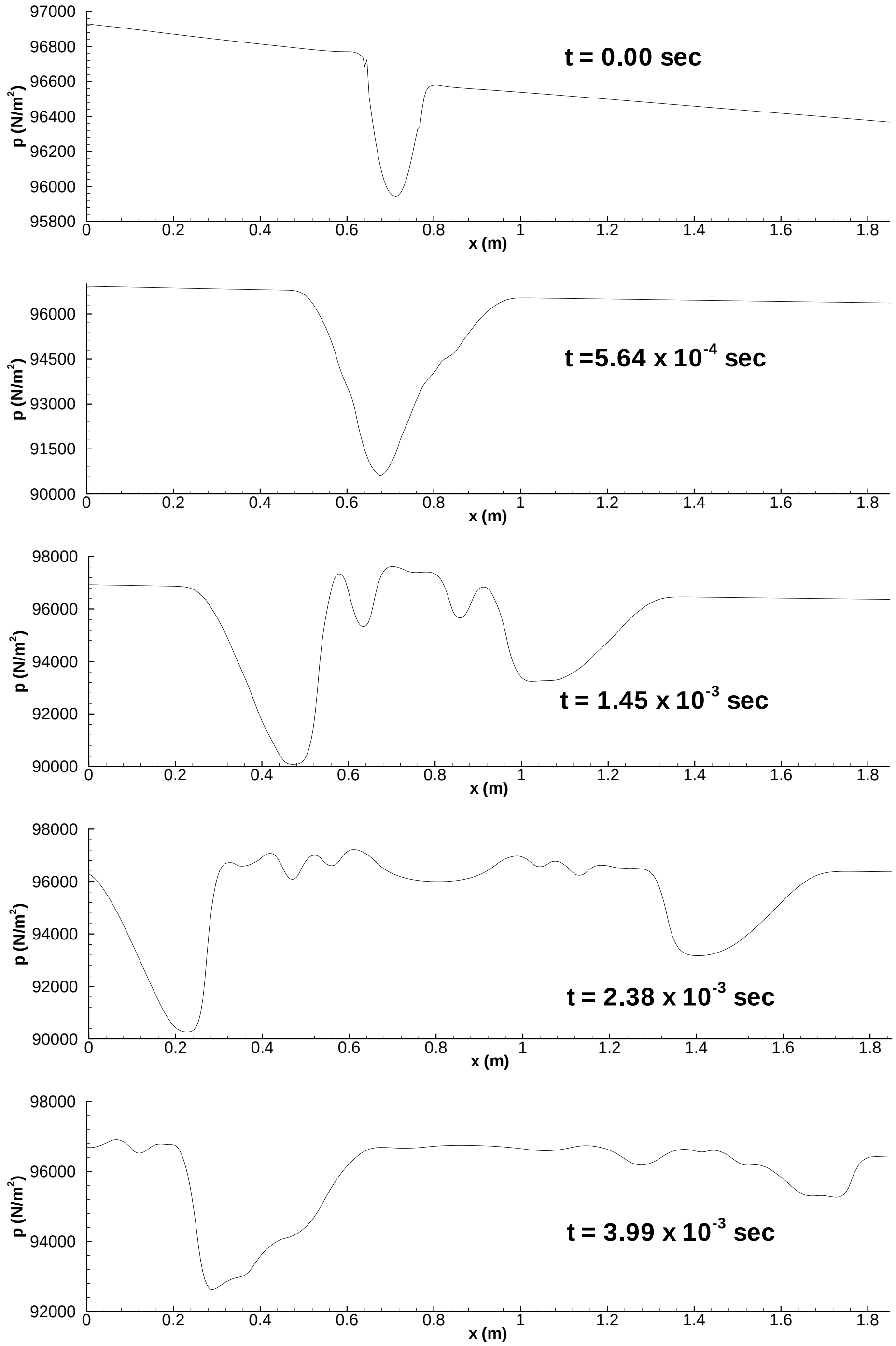

Figure 53: Pressure Profiles of Wave Propagation Through the Inlet at $y = 0.099$ m

directions are essentially planar. This planar nature of the flow validates the use of a one-dimensional model for this inlet.

Figure 54 shows the time history of the downstream travelling incident expansion pulse as recorded by transducer station 1. The amplitude of the experimental incident expansion pulse was -3576 Pa, and the amplitude of the incident pulse for the axisymmetric model was -3295 Pa. The relative percent difference of the numerical amplitude compared to the experimental amplitude was 7.85%. The oscillatory nature of the flow field between the two expansion pulses probably contributed to the reduced amplitude of the downstream propagating numerical pulse. Although the numerical incident expansion pulse had an amplitude less than experimental, this pulse was still used to test the compressor face boundary conditions. The percentage of reflected pulse amplitude to incident pulse amplitude for the numerical results was compared to the percentage measured from the experimental results. As stated in the one-dimensional results, the oscillations in the experimental results were thought to be caused by rebounding of the flexible bump from the hub cage. The oscillations observed in the numerical results were similiar to the waves in the experiment, but the numerical oscillations had a higher frequency and less damping than the ones measured in the experimental test run.

The numerical reflection results from the new small disturbance compressor face boundary condition model were compared with the experimental data for the University of Cincinnati run 14A. Figure 55 shows the comparison of the numerical results with the experimental data measured at transducer station 4. The essential overlap of the experimental results at both the hub and case illustrate the planar nature of the acoustic waves travelling through the inlet. The numerical results also show the same character. At station 4, the incident and reflected waves overlap. Previously, the incident pulse measured at transducer 1 was shifted in time and subtracted from

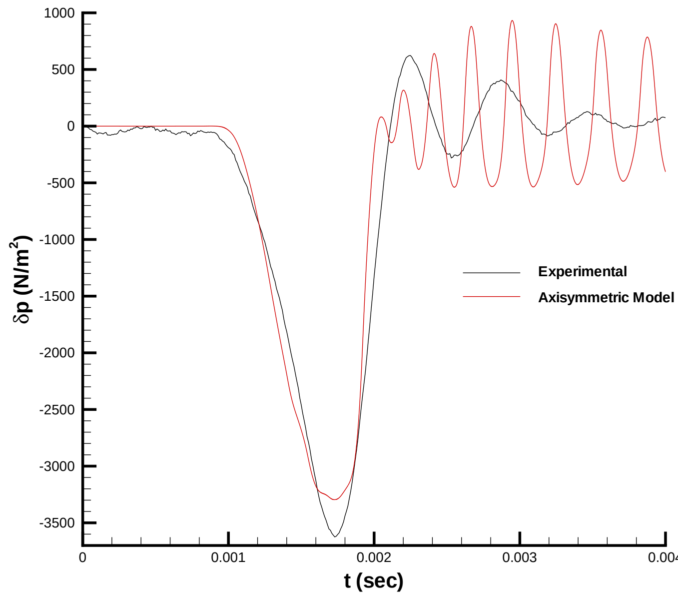

Figure 54: Comparison of Incident Acoustic Expansion Pulses at Station 1 for Run 14A

the pressure data collected at transducer 4 to investigate the amplitude and shape of the reflected wave. However, the high frequency oscillatory nature of the flow behind the incident wave made the calculation of the numerical reflected wave amplitude extremely difficult. Therefore, the pressure profile at $t = 3.99 \times 10^{-3}$ sec in Figure 53 was used to show the reflected wave amplitude and shape.

Figure 56 shows the reflected acoustic pulses created by Paynter small disturbance, new small disturbance, and area reduction boundary conditions for run 14A. The damped oscillations produced by the oscillatory nature of the flow field between the incident pulses interacts with the reflected pulses. The amplitude of the Paynter model reflection pulse was -1112 Pa which corresponded to a 33.7% reflection of the numerical incident pulse amplitude from the compressor face boundary condition. The new small disturbance boundary condition produced a reflected wave of amplitude -1161 Pa which corresponded to a 35.2% reflection of the numerical incident wave

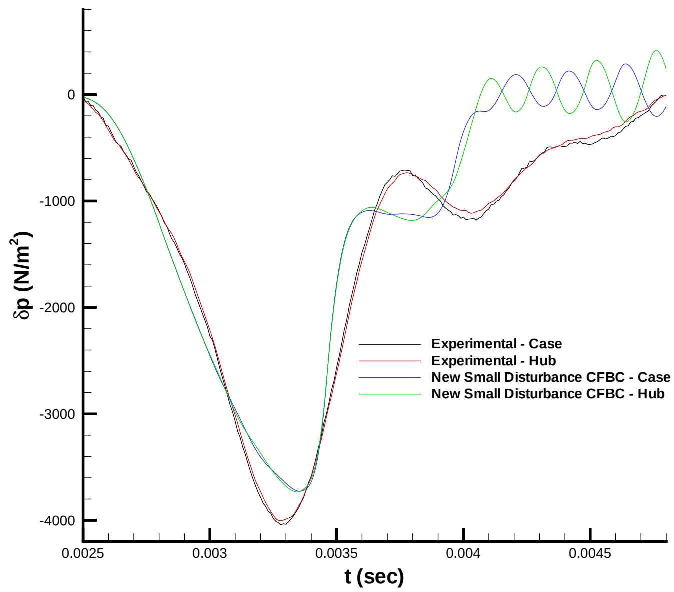

Figure 55: Comparison of Pressure Data at Transducer Station 4 for Run 14A

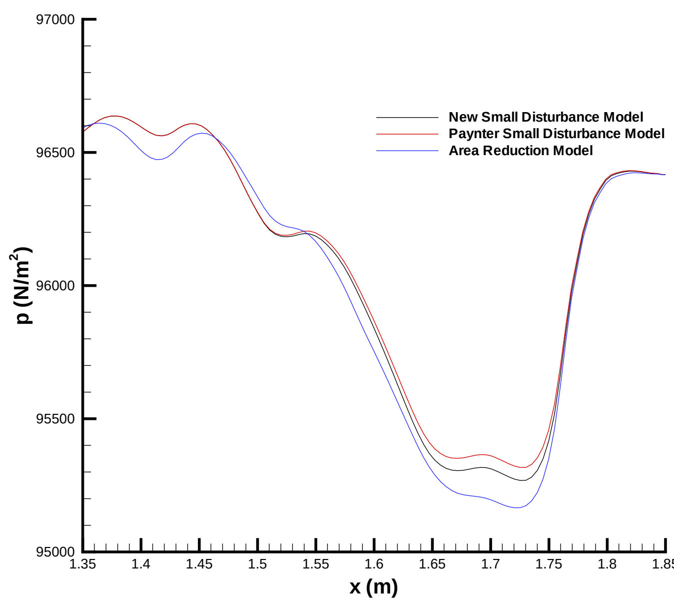

Figure 56: Reflected Acoustic Waves from Compressor Face Boundary Conditions for Run 14A

amplitude. Finally, the area reduction reflection pulse had an amplitude of -1264 Pa which was a 38.4% reflection. The experimental results showed a 36.8% reflection from the compressor face. All of the boundary conditions produced reflected pulse amplitudes that agree well qualitatively with the measured amplitude of compressor reflection. Like the one-dimensional results, the new small disturbance boundary condition performed better than the Paynter model when compared to the experimental amount of reflection.

6.2.3 Experimental Test Run 010A

Second, the results from the axisymmetric model were compared to the experimental data from run 010A. Table 3 lists the flow and compressor conditions for this experimental test. Again, the rotor stagger angle listed in the table is the angle at the mean radius. Figure 57 shows steady state pressure profile along the case for run 10A. The results show a pressure drop of 180 Pa across the bump. The normal pressure drop due to the growth of the boundary layer should be approximately 80 Pa.

Figure 58 shows the time history of the incident expansion pulse as recorded at station 1. The amplitude of the experimental incident expansion pulse was -3485 Pa. The amplitude of the incident pulse for the axisymmetric model was -3214 Pa which corresponded to a relative percent difference of 7.78%. Again, the oscillatory nature of the flow probably contributed to this reduction in the amplitude of the acoustic expansion pulse. The amplitude of the numerical incident pulse was used to determine the amount of reflection caused by the compressor face boundary conditions.

Figure 59 shows the reflected acoustic pulses created by Paynter small disturbance, new small disturbance, and area reduction boundary conditions for run 010A. Again, the high frequency oscillations in the flow field interacted with the reflected pulses. The amplitude of the Paynter model reflection pulse was -1080 Pa which corresponded to a 33.6% reflection of the numerical incident pulse, and the ampli-

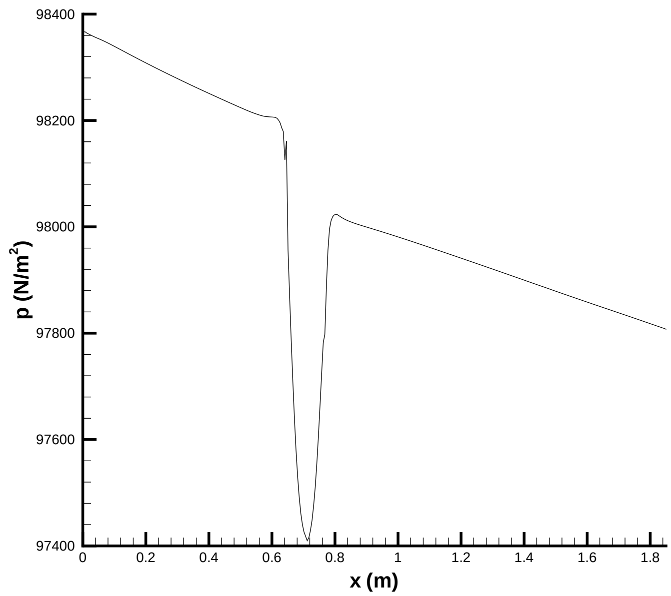

Figure 57: Steady State Pressure Profile for Run 010A

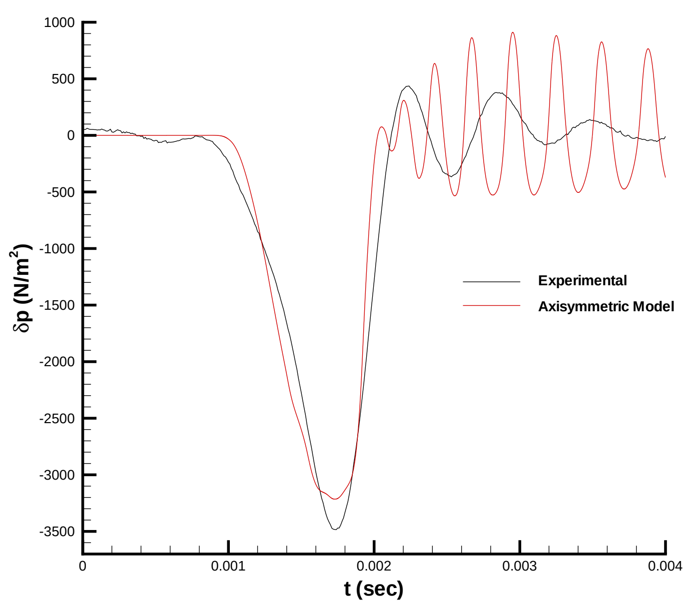

Figure 58: Comparison of Incident Acoustic Expansion Pulses at Station 1 for Run 010A

tude of the new small disturbance reflected wave was -1186 Pa which corresponded to a 36.9% reflection. The area reduction boundary condition produced a reflected wave with an amplitude of -1226 Pa which corresponded to a 38.1% reflection from the boundary condition. The experimental results showed a 39.5% reflection by the compressor. Again, the new small disturbance boundary condition produced a reflected pulse that agreed better with the experimental data than the Paynter small disturbance boundary condition. However, the area reduction boundary condition performed better than both of the small disturbance boundary conditions for this test run.

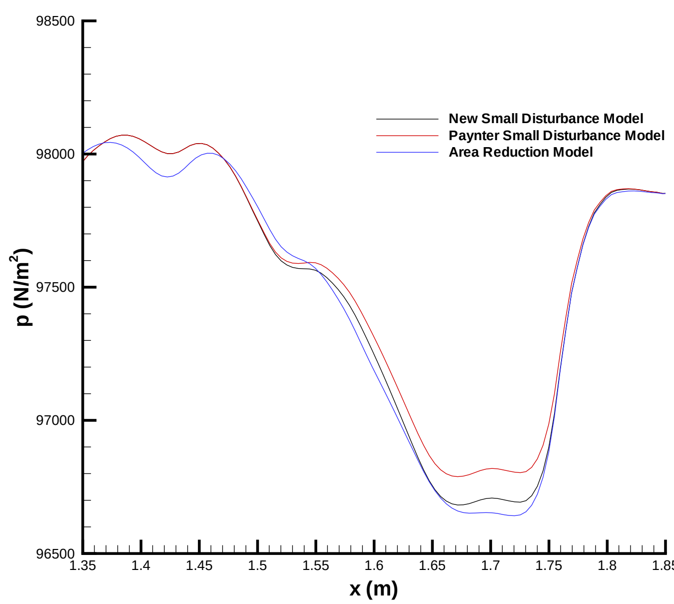

Figure 59: Reflected Acoustic Waves from Compressor Face Boundary Conditions for Run 010A

6.2.4 Experimental Test Run 41A

Third, the results from the axisymmetric model were compared to the experimental data from run 41A. Table 4 lists the flow and compressor conditions for this experimental test. Again, the rotor stagger angle listed in the table is the angle at the mean radius. Figure 60 shows steady state pressure profile along the case for run 41A. This pressure profile shows a 215 Pa pressure drop across the flexible bump. The normal pressure drop due to the growth of the boundary layer should be approximately 90 Pa.

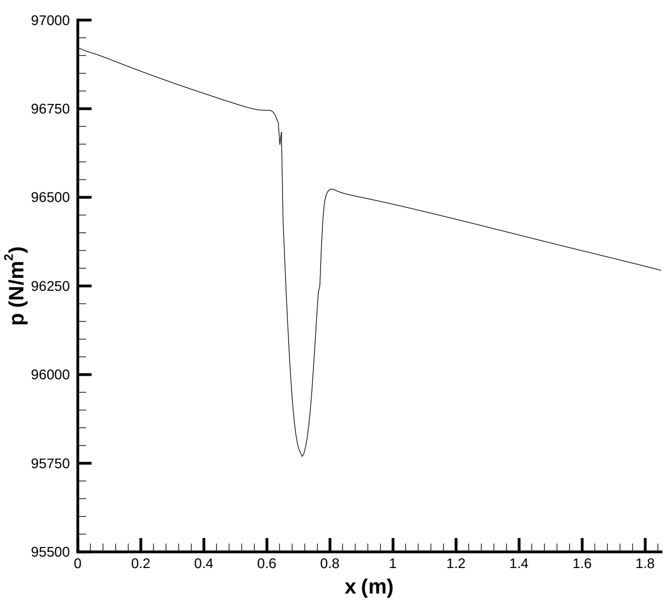

Figure 60: Steady State Pressure Profile for Run 41A

Figure 61 shows the time history of the acoustic expansion pulse as recorded at station 1. This incident pulse propagates downstream and interacts with the compressor face. The amplitude of the experimental pulse was −3719 Pa, and the amplitude of the numerical pulse was −3371 Pa. The relative percent difference between the numerical and experimental pulse amplitudes was 9.16%. This difference in pulse amplitudes is probably due to the oscillations in the flow field. Again, the amplitude of the numerical pulse was used to determine the percentage of reflection.

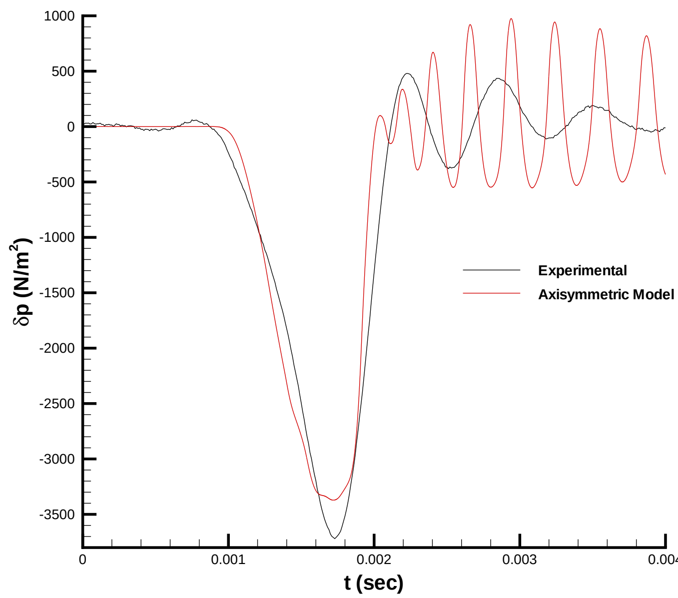

Figure 61: Comparison of Incident Acoustic Expansion Pulses at Station 1 for Run 41A

Figure 62 shows the reflected acoustic pulses created by Paynter small disturbance, new small disturbance, and area reduction boundary conditions for run 41A. The experimental data showed a 36.1% reflection from the axial compressor for this run. The new small disturbance compressor face boundary condition reflected an expansion pulse with an amplitude of -1258 Pa. This reflection was 37.3% of the incident numerical pulse amplitude. The amplitude of the area reduction reflection pulse was -1353 Pa which corresponded to a 40.1% reflection, and the amplitude of the Paynter model reflection pulse was -1144 Pa. This amplitude was a 33.9% reflection of the numerical incident pulse amplitude. The new small disturbance boundary condition provided a reflection that agreed quantitatively within 2% of the measured reflection characteristics of the compressor.

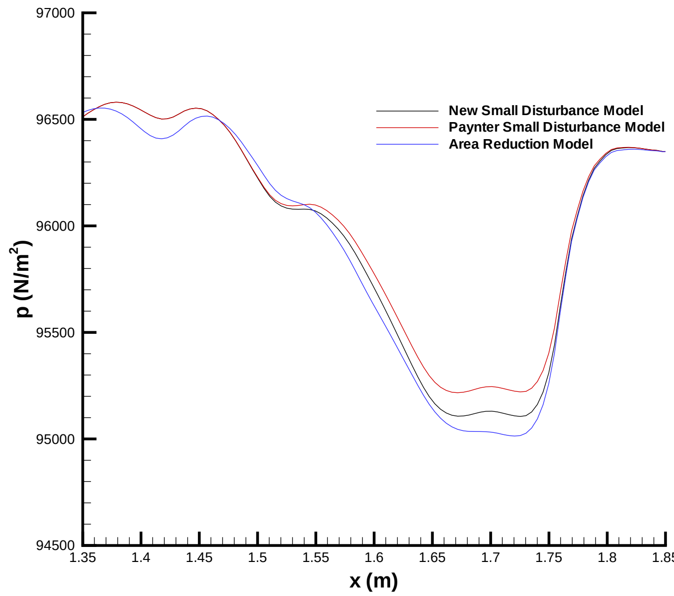

Figure 62: Reflected Acoustic Waves from Compressor Face Boundary Conditions for Run 41A

6.2.5 Experimental Test Run 40A

Finally, the results from the axisymmetric model were compared to the experimental data from run 40A. Table 5 lists the flow and compressor conditions for this experimental test. Again, the rotor stagger angle listed in the table is the angle at the mean radius. Figure 63 shows steady state pressure profile along the case for run 40A. A 205 Pa pressure drop across the bump was calculated for this numerical case. Again, the normal pressure drop due to the growth of the boundary layer should be approximately 90 Pa.

Figure 64 shows the time history of the acoustic expansion pulse as calculated by the transducer at station 1. The amplitude of the experimental pulse was −3515 Pa. The amplitude of the numerical incident pulse was −3214 Pa which corresponded to a relative percent difference of 8.56%. For all four experimental test runs, the

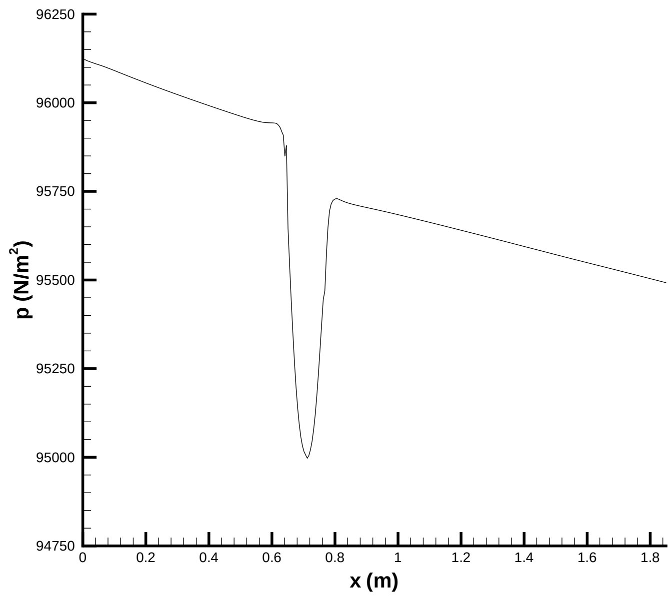

Figure 63: Steady State Pressure Profile for Run 40A

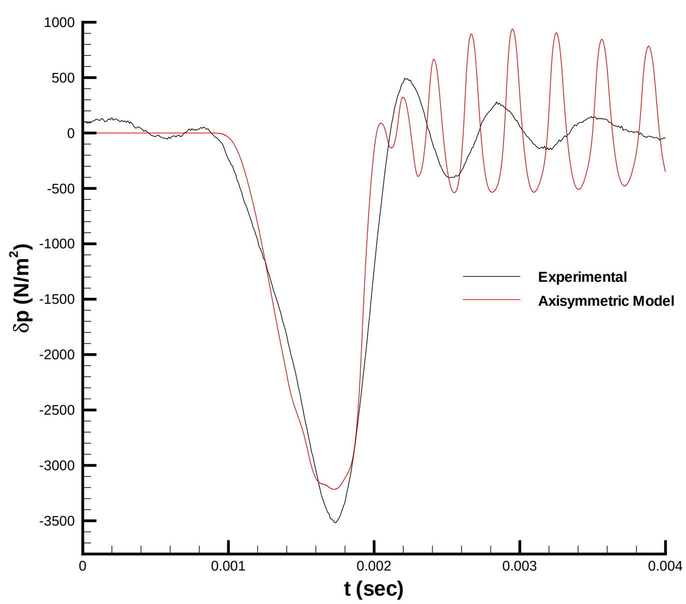

Figure 64: Comparison of Incident Acoustic Expansion Pulses at Station 1 for Run 40A

oscillatory behavior of the flow probably caused the amplitude of the numerical pulse to be approximately 8% less than the experimental pulse amplitude.

Figure 65 shows the reflected acoustic pulses created by the three compressor face boundary conditions for run 40A. The experimental data showed a 31.7% reflection from the axial compressor for this run. Again, this reflection percentage was much lower than that measured for all other experimental runs. The new small disturbance compressor face boundary condition reflected an expansion pulse with an amplitude of -1192 Pa which corresponded to a 37.1% reflection of the numerical incident wave. The amplitude of the Paynter model reflection pulse was -1145 Pa which corresponded to a 35.6%. The area reduction reflection pulse had an amplitude of -1209 Pa. Like the one-dimensional results, all boundary conditions overpredicted the amount of reflection for this experimental test run. However, the new small disturbance boundary condition calculated the amount of reflection from the compressor face within 5.4% of the experimental amount for all runs investigated. If run 40A is omitted, the reflection from the new small disturbance boundary condition agreed within 2.6% of the experimental reflection compared to 5.9% for the Paynter small disturbance model. The new small disturbance boundary condition provided more accurate reflection results for both one-dimensional and axisymmetric models of the University of Cincinnati experiment than the Paynter boundary condition did.

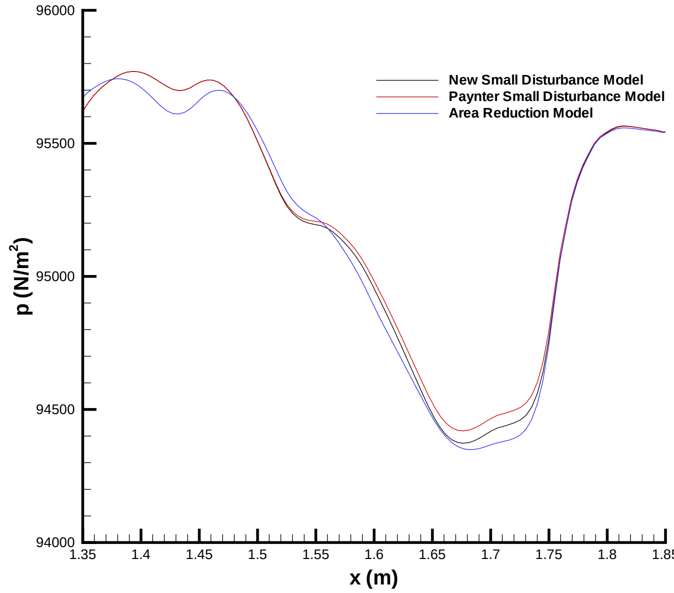

Figure 65: Reflected Acoustic Waves from Compressor Face Boundary Conditions for Run 40A

7 Conclusions

The new small disturbance and area reduction compressor face boundary conditions were developed to properly model the interaction of an acoustic pulse and an axial compressor. The new small disturbance boundary condition included parameters neglected in the Paynter small disturbance formulation. This new model accounted for the inlet guide vanes, cambered rotor blades, and the rotational speed of the compressor. Therefore, the new small disturbance boundary condition provided a more accurate representation of an axial compressor. The area reduction boundary condition used a simple approach. The cross-sectional area for the domain was reduced across the first stage rotor by an amount equal to the amount of frontal area in a blade passage seen as closed to the entering acoustic wave. Both of these boundary conditions were applied in one-dimensional and axisymmetric models of the experiment at the University of Cincinnati. Their acoustic wave reflection results were compared to the experimental data measured for four test cases and the Paynter small disturbance boundary condition results.

The one-dimensional results showed that the new small disturbance boundary condition accurately modeled the reflection characteristics of the axial compressor within 6% for all test cases. In addition, this new boundary condition provided improved reflection predictions compared to the Paynter model. The area reduction boundary condition did not perform as well as the new small disturbance boundary condition. However, this simple boundary condition did provide reflections that agreed well with the experimental reflection characteristics of the compressor.

The numerical effects present in the axisymmetric model caused some problems in the calculation of the initial steady flow conditions and the final evaluation of the compressor face boundary conditions. However, the reflection results showed that the new small disturbance boundary condition still provided the best agreement with experimental data from the University of Cincinnati. Therefore, the new small disturbance compressor face boundary condition was shown to be the best alternative for modeling the interaction between an acoustic disturbance and an axial compressor. For the axisymmetric model, the area reduction boundary condition produced reflections that agreed well with the experimental data. The easy of implementation and good agreement with the experimental data makes the area reduction model a viable compressor face boundary condition alternative for design studies.

The one-dimensional and axisymmetric models provided very similar results for the reflection characteristics of the University of Cincinnati axial compressor. In addition, the expansion pulses created by the collapsing bump for the axisymmetric model were essentially planar. Therefore, the one-dimensional model of the flow field through this inlet is a valid and computationally less expensive alternative for investigating the reflection characteristics of the compressor face boundary.

For future research, both the new small disturbance and area reduction boundary conditions need to be implemented in inlet CFD codes and tested to see how well they can predict inlet unstart. Based on their performance compared to the University of Cincinnati experimental data, both of these boundary conditions should provide more accurate predictions than the currently imposed compressor face boundary conditions. In addition, more investigation on how to eliminate the numerical diffusion in the axisymmetric flow model is needed. Possible solutions are development of a time accurate preconditioned numerical model and use of all viscous flux terms instead of the thin layer approximation terms.

References

[1] Mayer, D. W. and Paynter, G. C., “Boundary Conditions for Unsteady Supersonic Inlet Analyses,” *AIAA Journal*, vol. 32, no. 6, June 1994, pp. 1200–1206.

[2] Garrard, D., Davis, M. Jr., Wehofer, S., and Cole, G., “A One Dimensional Time Dependent Inlet/Engine Numerical Simulation for Aircraft Propulsion Systems,” ASME Paper 97-GT-333, June 1997.

[3] Numbers, K. and Hamed, A., “Development of a Coupled Inlet-Engine Dynamic Analysis Method,” AIAA Paper 97-2880, July 1997.

[4] Clark, L. T., “Dynamic Response Characteristics of a Mixed Compression Supersonic Inlet as a Part of a Larger System,” AIAA Paper 95-0036, January 1995.

[5] Suresh, A., Townsend, S. E., Cole, G. L., Slater, J. W., and Chima, R., “Analysis of Inlet-Compressor Acoustic Interactions Using Coupled CFD Codes,” AIAA Paper 99-0749, January 1999.

[6] Kovasznay, L. S. G., “Turbulence in Supersonic Flow,” *Journal of the Aeronautical Sciences*, vol. 20, no. 10, October 1953, pp. 657–675.

[7] Decher, R., Mayer, D. W., and Paynter, G. C., “On Supersonic Inlet-Engine Stability,” AIAA Paper 94-3371, June 1994.

[8] Chung, J. K., “Numerical Simulation of a Mixed Compression Supersonic Inlet Flow,” AIAA Paper 94-0583, January 1994.

[9] Freund, D. and Sajben, M., “Experimental Investigation of Outflow Boundary Conditions Used in Unsteady Inlet Flow Computations,” AIAA Paper 97-0610, January 1997.

[10] Freund, D. and Sajben, M., “Reflection of Large Amplitude Acoustic Pulses from an Axial Flow Compressor,” AIAA Paper 97-2879, July 1997.

[11] Freund, D. D., “Experimental Exploration of Compressor-Face Boundary Conditions for Unsteady Inlet Flow Computations,” Ph.D. Dissertation, Department of Aerospace Engineeing and Engineering Mechanics, University of Cincinnati, December 1997.

[12] Freund, D. and Sajben, M., “Experiment to Support the Formulation and Validation of Compressor-Face Boundary Conditions,” *Journal of Propulsion and Power*, vol. 16, no. 3, May June 2000, pp. 406–414.

[13] Mayer, D. W. and Paynter, G. C., “Prediction of Supersonic Inlet Unstart Caused by Freestream Disturbances,” *AIAA Journal*, vol. 33, no. 2, February 1995, pp. 266–275.

[14] Chung, J. K. and Cole, G. L., “Comparison of Compressor Face Boundary Conditions for Unsteady CFD Simulations of Supersonic Inlets,” AIAA Paper 95-2627, July 1995.

[15] Slater, J. W. and Paynter, G. C., "Implementation of a Compressor Face Boundary Condition Based on Small Disturbances," *Journal of Turbomachinery*, vol. 123, no. 2, April 2001, pp. 386–391.

[16] Freund, D. and Sajben, M., "Experimental Exploration of Compressor-Face Boundary Conditions for Unsteady Inlet Flow Computations," AIAA Paper 95-2886, July 1995.

[17] Freund, D., Sajben, M., and Slater, J. W., "Compressor-Face Boundary Condition Experiment: Generation of Acoustic Pulses in Annular Ducts," AIAA Paper 96-2657, July 1996.

[18] Paynter, G. C., "Response of a Two-Dimensional Cascade to an Upstream Disturbance," *AIAA Journal*, vol. 35, no. 3, March 1997, pp. 434–440.

[19] Paynter, G. C., "Modeling the Response from a Cascade to an Upstream Convective Velocity Disturbance," AIAA Paper 98-3570, July 1998.

[20] Paynter, G. C., Clark, L. T., and Cole, G. L., "Modeling the Response from a Cascade to an Upstream Acoustic Disturbance," *AIAA Journal*, vol. 38, no. 8, August 2000, pp. 1322–1330.

[21] Shapiro, A. H., *The Dynamics and Thermodynamics of Compressible Fluid Flow*, vol. 2, The Ronald Press Company, New York, 1954, p. 918.

[22] Sajben, M., "Prediction of Acoustic, Vorticity, and Entropy Waves Generated by Short-Duration Acoustic Pulses Incident on a Blade Row," ASME Paper 99-GT-148, June 1999.

[23] Schlichting, H., *Boundary-Layer Theory, Seventh Edition*, McGraw-Hill, Inc., New York, 1979, p. 638.

[24] Slater, J. W., Freund, D., and Sajben, M., "Study of CFD Methods Applied to Rapidly Deforming Boundaries," AIAA Paper 97-2041, July 1997.

[25] Wilcox, D. C., *Turbulence Modeling for CFD, Second Edition*, DCW Industries, 1998, pp. 29–39.

[26] Spalart, P. R. and Allmaras, S. R., "A One-Equation Turbulence Model for Aerodynamic Flows," *La Recherche Aérospatiale*, vol. 1, 1992, pp. 5–21.

[27] White, F. M., *Viscous Fluid Flow, Second Edition*, McGraw-Hill, Inc., New York, 1991, pp. 28–29.

[28] Roe, P. L., "Approximate Riemann Solvers, Parameter Vectors and Difference Schemes." *Journal of Computational Physics*, vol. 43, no. 2, October 1981, pp. 357–372.

[29] Vatsa, V. N., Thomas, J. L., and Wedan, B. W., "Navier-Stokes Computations of a Prolate Spheroid at Angle of Attack," *Journal of Aircraft*, vol. 26, November 1989, pp. 986–993.

[30] Harten, A. and Hyman, J. M., "Self Adjusting Grid Methods for One-Dimensional Hyperbolic Conservation Laws," *Journal of Computational Physics*, vol. 18, no. 2, May 1983, pp. 235-269.

[31] Tannehill, J. C., Anderson, D. A., and Pletcher, R. H., *Computational Fluid Mechanics and Heat Transfer, Second Edition*, Taylor and Francis, Washington DC, 1997, pp. 106, 209, 542–543.

[32] Coffey, T., McMullan, R. J., Kelley, C. T., and McRae, D. S., "Globally Convergent Algorithms for Nonsmooth Nonlinear Equations in Computational Fluid Dynamics," CRSC-TR01-28, November 2001.

[33] Edwards, J. R., "Numerical Implementation of a Modified Liou-Steffan Upwind Scheme," *AIAA Journal*, vol. 32, no. 10, October 1994, pp. 2120–2122.

[34] Edwards, J. R., "A Low -Diffusion Flux-Splitting Scheme for Navier-Stokes Calculations," *Computers and Fluids*, vol. 26, no. 6, July 1997, pp. 635–659.

[35] Kelley, C. T., *Iterative Methods for Linear and Nonlinear Equations*, SIAM, Philadelphia, 1995, pp. 33–59.

[36] Saad, Y. and Schultz, M., "GMRES a Generalized Minimal Residual Algorithm for Solving Nonsymmetric Linear Systems," *SIAM Journal on Scientific and Statistical Computing*, vol. 7, no. 3, July 1986, pp. 856–869.

[37] Hirsch, C., *Numerical Computation of Internal and External Flows, Volume 2*, John Wiley and Sons, Chichester, England, 1990, pp. 334–335.